Knots and planar Skyrmions

JENNINGS, PAUL,ROBERT

Knots and planar Skyrmions

Paul R. Jennings

A Thesis presented for the degree of
Doctor of Philosophy

Centre for Particle Theory
Department of Mathematical Sciences
University of Durham
England

March 2015

Dedicated to

My family

Knots and planar Skyrmions

Paul R. Jennings

Submitted for the degree of Doctor of Philosophy
March 2015

Abstract

In this thesis the research presented relates to topological solitons in $(2+1)$ and $(3+1)$-dimensional Skyrme theories. Solutions in these theories have topologically invariant quantities which results in stable solutions which are topologically distinct from a vacuum.

In Chapter 2 we discuss the broken baby Skyrme model, a theory which breaks symmetry to the dihedral group D_N. It has been shown that the unit soliton solution of the theory is formed of N distinct peaks, called partons. The multi-soliton solutions have already been numerically simulated for $N = 3$ and were found to be related to polyiamonds. We extend this for higher values of N and demonstrate that a polyform structure continues. We discuss our numerical simulations studying the dynamics of this model and show that the time dependent behaviour of solutions in the model can be understood by considering the interactions of individual pairs of partons. Results of these dynamics are then compared with those of the standard baby Skyrme model.

Recently it has been demonstrated that Skyrmions of a fixed size are able to exist in theories without a Skyrme term so long as the Skyrmion is located on a domain wall. In Chapter 3 we present a $(2+1)$-dimensional $O(3)$ sigma model, with a potential term of a particular form, in which such Skyrmions exist. We numerically compute domain wall Skyrmions of this type. We also investigate Skyrmion dynamics so that we can study Skyrmion stability and the scattering of multi-Skyrmions. We consider scattering events in which Skyrmions remain on the same domain wall and find they are effectively one-dimensional. At low speeds these scatterings are

well-approximated by kinks in the integrable sine-Gordon model. We also present more exotic fully two-dimensional scatterings in which Skyrmions initially on different domain walls emerge on the same domain wall.

The Skyrme-Faddeev model is a $(3+1)$-dimensional non-linear field theory that has topological soliton solutions, called hopfions. Solutions of this theory are unusual in that that they are string-like and take the form of knots and links. Solutions found to date take the form of torus knots and links of these. In Chapter 4 we show results which address the question of whether any non-torus knot hopfions exist. We present a construction of fields which are knotted in the form of cable knots to which an energy minimisation scheme can be applied. We find static hopfions of the theory which do not have the form of torus knots, but instead take the form of cable and hyperbolic knots.

In Chapter 5 we consider an approximation to the Skyrme-Faddeev model in which the soliton is modelled by elastic rods. We use this as a mechanism to study examples of particular knots to attempt to gain an understanding of why such knots have not been found in the Skyrme-Faddeev model. The aim of this study is to focus the search for appropriate rational maps which can then be applied in the Skyrme-Faddeev model.

The material presented in this thesis relates to two published papers [1] and [2] corresponding to Chapters 2 and 3 respectively, which were done as part of a collaboration. In this thesis my own results are presented. Chapter 4 concerns material which relates to the preprint [3] which is all my own work. Chapter 5 discusses my own ongoing work.

Declaration

The work in this thesis is based on research carried out at the Centre for Particle Theory, Department of Mathematical Sciences, England. No part of this thesis has been submitted elsewhere for any other degree or qualification and it is all my own work unless referenced to the contrary in the text.

Acknowledgements

I would like to thank Daniel Jones, Andrew Lobb and Thomas Winyard for helpful discussions and suggestions. I would particularly like to thank Paul Sutcliffe for his supervision and guidance. I am grateful to the Science and Technology Facilities Council for funding during the undertaking of this work. Finally, thank you to Alice, my family and all my friends for their support through my studies and for helping me maintain some semblance of sanity.

Contents

List of Figures

List of Tables

Chapter 1

Introduction

In this chapter we provide a general introduction to the main concepts involved in this thesis. We explain the ideas underpinning topological solitons which we shall assume and make use of in further chapters of this work such as homotopy theory, topological charges and Derrick's theorem. We also introduce a number of models which will be referred to within the main body of the thesis. We examine a simple $(1+1)$-dimensional kink model to demonstrate these concepts and then discuss the Skyrme-type models in $(2+1)$ and $(3+1)$ dimensions.

Topological solitons are particle-like solutions of full non-linear classical field equations which are topologically distinct from the vacuum. By this we mean that solutions can not be deformed smoothly to be the vacuum due to some underlying topology of the theory. This topology therefore causes solutions which are stable to relatively large perturbations. There are numerous examples of topological solitons in various dimensions including kinks, vortices, monopoles, instantons and Skyrmions. They can be found in many non-linear classical field theories. See [4] for a comprehensive review of the many types of topological solitons.

1.1 Homotopy theory and topological charge

Given two manifolds X and Y without a boundary, consider two based maps $\varphi_1, \varphi_2 : X \to Y$. We say that φ_1 is homotopic to φ_2 if it can be continuously deformed to give φ_2. We see then that homotopy is an equivalence relation, and so we can classify

maps into equivalence classes, called homotopy classes. These classes will classify the topology of the map. We denote the set of homotopy classes of based maps $\varphi : S^n \to Y$ as $\pi_n(Y)$ and this is in fact a group for $n \geq 1$. In particular, we find that $\pi_n(S^n) = \mathbb{Z}$ for $n \geq 1$ and $\pi_3(S^2) = \mathbb{Z}$, which will be the cases considered in this thesis so the topology of these maps is classed by the integers. We shall refer to the integer corresponding to a particular map as the topological charge of the map. In practice one can drop the requirement of the maps being based, so long as the domain X is connected and the codomain Y is simply connected since this is only important for the group structure.

In the case where the field is a map between closed manifolds of the same dimension we can express this topological charge as the topological degree of the map. Suppose that $\varphi : X \to Y$ is a differentiable map with $\dim X = \dim Y$ and X connected. Then given a unit form Ω on Y, that is $\Omega = \beta(\mathbf{y})d^D\mathbf{y}$, normalised such that $\int_Y \Omega = 1$, the topological degree is given by the integral of the pull-back of this volume form over X,

$$\deg \varphi = \int_X \varphi^*(\Omega) = \int \beta(\mathbf{y}(\mathbf{x}))J(\mathbf{x})d^D\mathbf{x}, \tag{1.1.1}$$

where $J(\mathbf{x}) = \det\left(\frac{\partial y^i}{\partial x^j}\right)$ is the Jacobian. For a map $\varphi : S^n \to S^n$ in the k'th homotopy class of $\pi_n(S^n)$, we have $\deg \varphi = k$.

For example, consider the case of a map $\boldsymbol{\phi} : S^2 \to S^2$. Then a normalised volume form is $\frac{1}{4\pi}\sin\chi\, d\theta\, d\chi$, and one may express $\boldsymbol{\phi} = (\cos\theta\sin\chi, \sin\theta\sin\chi, \cos\chi)$. It then follows that

$$\deg \boldsymbol{\phi} = \frac{1}{4\pi}\int \sin\chi(\partial_x\theta\partial_y\chi - \partial_x\chi\partial_y\theta)\, dxdy = -\frac{1}{4\pi}\int \boldsymbol{\phi}\cdot(\partial_x\boldsymbol{\phi}\times\partial_y\boldsymbol{\phi})\, dxdy \tag{1.1.2}$$

where the final step follows from the form of the map $\boldsymbol{\phi}$ given above.

Alternatively, we can think of the degree of the map as counting the number of preimages of a point in Y with multiplicity. Consider a point $\mathbf{y} \in Y$ with a (possibly empty) set of preimages $\{\mathbf{x}^{(1)}, \ldots, \mathbf{x}^{(M)}\}$ at each of which the Jacobian of the map φ is non-zero. Then

$$\widetilde{\deg}\,\varphi = \sum_{m=1}^{M} \operatorname{sgn}(J(\mathbf{x}^{(m)})), \tag{1.1.3}$$

where $J(\mathbf{x}^{(m)})$ is the Jacobian evaluated at $\mathbf{x}^{(m)}$. This obviously gives an integer and counts the preimages with multiplicity $+1$ or -1 depending on whether the map φ is locally orientation preserving or orientation reversing. It is then a theorem that $\deg \varphi = \widetilde{\deg}\, \varphi$ and the above definition is independent of the choice of the point $\mathbf{y} \in Y$ [4]. This preimage counting argument for the degree of a map will be a very useful concept in later chapters.

Given a scalar field theory of a type which is governed by a suitable Lagrangian at a fixed time it can be thought of a as map $\phi : X \to Y$. Then if this satisfies a dynamic field equation it must be continuous in space and time and so has a well defined homotopy class which is independent of time, i.e. the homotopy class is a topological conserved quantity.

1.2 Derrick's Theorem

Consider a time independent field configuration in a non-trivial homotopy class. We want stable solutions (i.e. energy minima) to exist in these homotopy classes. Derrick's theorem [5] is a non-existence theorem that applies to field theories in flat space. It states that any field configuration which is a stationary point of the energy must be stationary to all variations and in particular should be stationary under spatial rescaling. If this is not the case then no stable non-trivial solutions can exist in the theory.

More precisely, suppose we have a finite energy field configuration, then let $e(\mu)$ be the energy of the field configuration after applying a spatial rescaling $\mathbf{x} \mapsto \mu\mathbf{x}$. Then if $e(\mu)$ has no stationary point, there can be no static solutions of the field equations with finite energy that have a non-trivial homotopy class, i.e. no static solutions other than the vacuum fields.

Consider a theory in d spatial dimensions with an energy functional of the form

$$E = E_4 + E_2 + E_0, \tag{1.2.4}$$

where E_i is a term of the energy which is of i'th order in spatial derivatives. Under a spatial rescaling $x \mapsto \mu x$, for non-zero $\mu \in \mathbb{R}$ we see that the energy scales as

$$E \mapsto e(\mu) = \mu^{d-4} E_4 + \mu^{d-2} E_2 + \mu^d E_0. \tag{1.2.5}$$

We shall use this to show that in particular dimensions such an energy functional has a stationary point under a spatial rescaling and so passes Derrick's theorem. This argument can also be used to find the scale of the soliton as a function of the parameters in the theory by considering the form of μ for the stationary point. We will see this in practice in the following sections in which we introduce specific models.

1.3 The sine-Gordon kink

The most basic topological soliton involves a single real scalar field $\phi(x,t)$ in one spatial dimension. The solitons which results from these are called kinks, due to the shape of the field. In this case we shall restrict ourselves to a particular potential, which gives rise to the sine-Gordon kink. This is a well known model and has applications in the modelling of elementary particles [6], and other applications where non-linear waves play an important role. The theory is governed by Lagrangian density

$$\mathcal{L} = \frac{1}{2}\partial_\mu\phi\,\partial^\mu\phi - (1-\cos\phi), \tag{1.3.6}$$

which leads to energy

$$E = \int_{-\infty}^{\infty} \frac{1}{2}(\partial_t\phi)^2 + \frac{1}{2}(\partial_x\phi)^2 + (1-\cos\phi)\,dx, \tag{1.3.7}$$

By variation of the Lagrangian we find the field equation

$$\partial_\mu\partial^\mu\phi + \sin\phi = 0. \tag{1.3.8}$$

This has vacuum field solutions $\phi(x,t) = 2\pi n$ for $n \in \mathbb{Z}$ which are isolated, and so the set of vacuum fields, $\mathcal{V}$, has the homotopy group $\pi_0(\mathcal{V}) = \mathbb{Z}$. We see that for an arbitrary field to have finite energy, the field must approach a vacuum value at spatial infinity, say

$$\lim_{x\to\pm\infty} \phi(x,t) = \phi_\pm = 2\pi n_\pm, \tag{1.3.9}$$

for some $n_\pm \in \mathbb{Z}$. These vacua are isolated and so the field cannot be deformed from one vacuum to another whilst keeping the energy finite. We further note that the system is symmetric under shifts of the field of the form $\phi \mapsto \phi + 2\pi k$ for $k \in \mathbb{Z}$, so

one can always arrange for $\phi_- = 0$. Thus the topology is captured by the difference of these and more generically one can write

$$N = \frac{\phi_+ - \phi_-}{2\pi} = \frac{1}{2\pi}\int_{-\infty}^{\infty} \partial_x \phi \, dx, \tag{1.3.10}$$

which gives the number of solitons in the field $\phi(x,t)$. We are able to write this topological number as the integral of a topological charge density. Although this seems an unusual way to write the topological charge it will make more sense in future examples to consider a topological charge density.

We see that the form of the static energy, that is energy function (1.3.7) with $\partial_t \phi = 0$, is of the correct form to avoid Derrick's theorem in one spatial dimension. As we saw in the previous section, under a spatial rescaling $x \mapsto \mu x$ the energy scales as $E = E_2 + E_0 \mapsto \frac{1}{\mu}E_2 + \mu E_0$. Thus there is a balancing of terms and so there could be stable solutions with non-trivial topological structure in the theory.

Manipulating the static energy by completing the square of the integrand, one finds that

$$\begin{aligned}
E &= \int_{-\infty}^{\infty} \left\{ \left(\frac{1}{\sqrt{2}} \partial_x \phi \mp \sqrt{1-\cos\phi} \right)^2 \pm \partial_x \phi \sqrt{2(1-\cos\phi)} \right\} dx \\
&\geq \pm \int_{-\infty}^{\infty} \sqrt{2(1-\cos\phi)} \partial_x \phi \, dx \\
&= \pm \int_{\phi_-}^{\phi_+} \sqrt{2(1-\cos\phi)} \, d\phi \\
&= \pm \int_0^{2\pi N} \sqrt{4\sin^2 \frac{\phi}{2}} \, d\phi \\
&= \pm 2N \int_0^{2\pi} \sin\frac{\phi}{2} \, d\phi \\
&= \pm 4N \Big[-\cos\frac{\phi}{2} \Big]_0^{2\pi} \\
&= \pm 8N,
\end{aligned} \tag{1.3.11}$$

where the sign is chosen such that $\pm N$ is positive, so $E \geq 8|N|$. This bound is saturated when $\partial_x \phi = \pm\sqrt{2(1-\cos\phi)}$, which can be integrated, and gives (for positive sign) that a static solution to the system is

$$\phi(x) = 4\arctan(\exp(x-a)). \tag{1.3.12}$$

It is natural to interpret the constant of integration a as the location of the kink. We see that taking $\phi_- = 0$ this has $\phi_+ = 2\pi$ and so has $N = 1$, describing a kink.

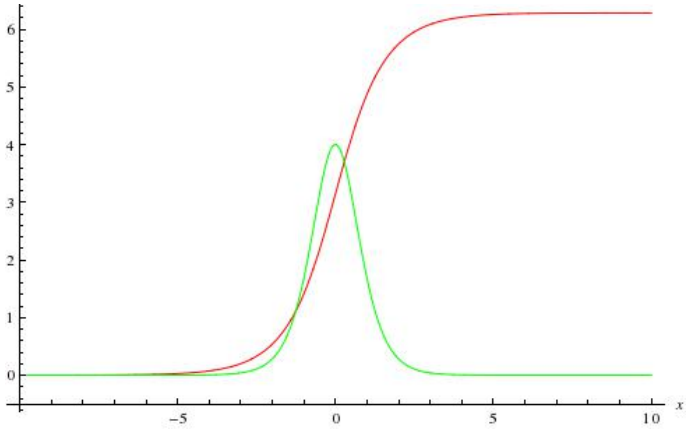

Figure 1.1: Plot showing the field $\phi(x)$ (red curve) of the sine-Gordon kink and its energy density (green curve) with $a = 0$.

The choice of sign only represents a change in sign $\phi \mapsto -\phi$ which describes an anti-kink with charge $N = -1$. It also follows from (1.3.12) and the form of the static energy that this static kink solution has energy density $\mathcal{E} = 4\,\mathrm{sech}^2(x-a)$. These have been plotted in Figure 1.1 from which the shape of a kink can be seen, as well as the localised nature of the energy density, localised about $x = a$, which in this case has been taken to be zero. Since it is only those kinks with $N = 1$ which saturate the Bogomolny bound two kinks must be repulsive.

It follows that since two kinks in this theory are repulsive, there are no static multi-soliton states. This system is in fact integrable and dynamic multi-soliton states can be found analytically. For this it will be convenient to work with the light-cone coordinates $x_\pm = \frac{1}{2}(x \pm t)$, and we define $\partial_\pm = \frac{\partial}{\partial x_\pm}$. In these coordinates field equation (1.3.8) then becomes $\partial_+\partial_-\phi = \sin\phi$. Given a particular field ϕ_0, we can define field ψ via the Bäcklund transformation

$$\partial_+\psi = \partial_+\phi_0 - 2\beta \sin\left(\frac{\phi_0+\psi}{2}\right), \qquad \partial_-\psi = -\partial_-\phi_0 + \frac{2}{\beta}\sin\left(\frac{\phi_0-\psi}{2}\right) \tag{1.3.13}$$

for non-zero $\beta \in \mathbb{R}$, called the Bäcklund parameter. This is subject to compatibility condition $\partial_+\partial_-\psi = \partial_-\partial_+\psi$ due to mixed partial derivatives commuting. It is then straightforward to check that this condition gives that $\partial_+\partial_-\phi_0 = \sin\phi_0$. Similarly we find from $\partial_+\partial_-\phi_0 = \partial_-\partial_+\phi_0$ that $\partial_+\partial_-\psi = \sin\psi$. Thus if ϕ_0 is a solution to the sine-Gordon field equations, then so is ψ.

For example, if we take ϕ_0 to be the vacuum field, $\phi_0 = 0$, then we see that

equations (1.3.13) become

$$\partial_+\psi = -2\beta \sin\frac{\psi}{2}, \qquad \partial_-\psi = -\frac{2}{\beta}\sin\frac{\psi}{2} \tag{1.3.14}$$

which we can easily integrate to give

$$\psi(x_+, x_-) = 4\arctan\left(\exp\left(-\beta x_+ - \frac{x_-}{\beta} + \alpha\right)\right) \tag{1.3.15}$$

for constant of integration α. Changing back to our original coordinates we find

$$\psi(x,t) = 4\arctan\left(\exp\left(\gamma(x - vt - a)\right)\right), \tag{1.3.16}$$

where we make the identifications

$$v = \frac{1-\beta^2}{1+\beta^2}, \qquad \gamma = -\frac{1+\beta^2}{2\beta} = \frac{1}{\sqrt{1-v^2}}, \qquad a = \frac{2\beta\alpha}{1+\beta^2}. \tag{1.3.17}$$

We note that the above field is just the Lorentz boosted solution we found for the static single kink solution (1.3.12).

We can then use these Lorentz boosted fields as the initial fields in a further Bäcklund transformation. Let ψ_1 and ψ_2 be fields of the form shown in (1.3.15) with Bäcklund parameters β_1 and β_2 respectively, and both with $\alpha = 0$. Consider the Bäcklund transformation to field ψ_{ij} which is the transformation of $\phi_0 = \psi_i$ with Bäcklund parameter β_j. We require these to satisfy consistency condition $\psi_{12} = \psi_{21}$ since Bäcklund transformations should commute. More accurately, Bäcklund transformations can be made to commute by making a choice of integration constant. This condition then gives that

$$\psi_{12} = \psi_{21} = 4\arctan\left(\frac{\beta_1+\beta_2}{\beta_2-\beta_1}\tan\left(\frac{\psi_1-\psi_2}{4}\right)\right) = 4\arctan\left(\frac{\beta_1+\beta_2}{\beta_2-\beta_1}\frac{\sinh\left(\frac{\theta_1-\theta_2}{2}\right)}{\cosh\left(\frac{\theta_1+\theta_2}{2}\right)}\right) \tag{1.3.18}$$

where $\theta_i = -\beta_i x_+ - \frac{x_-}{\beta_i}$. When we choose for $\beta_1 = \beta$ and $\beta_2 = -1/\beta$ we find the solution to the sine-Gordon equation is

$$\phi_{kk}(x,t) = 4\arctan\left(\frac{v\sinh(\gamma x)}{\cosh(\gamma v t)}\right). \tag{1.3.19}$$

We see that this describes a field in which two sine-Gordon kinks scatter. We will make use of this explicit form in Chapter 3. We plot the field and energy density

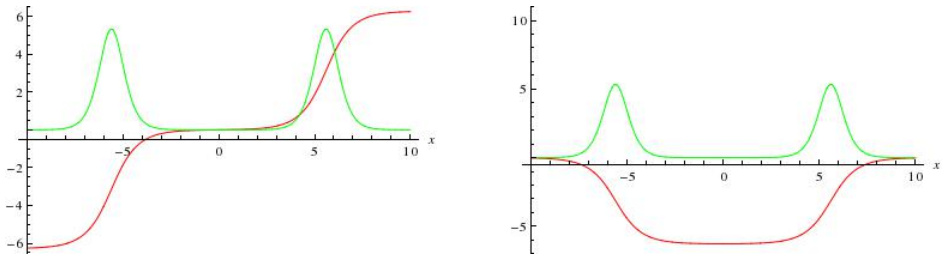

(a) $t = -10$

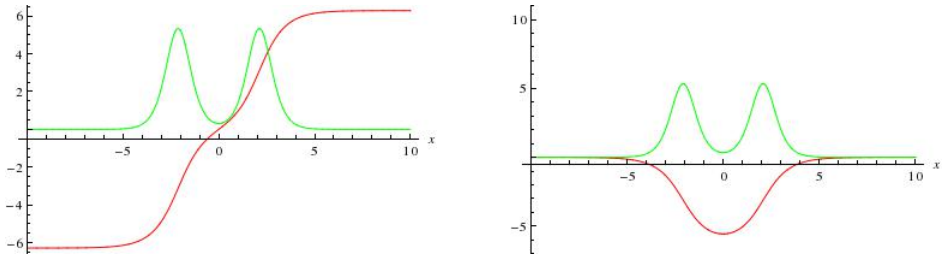

(b) $t = -3$

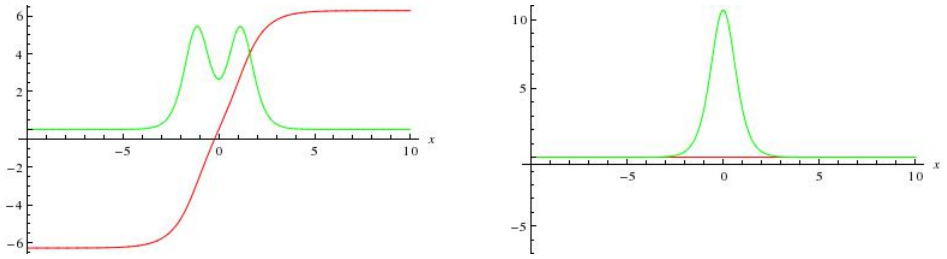

(c) $t = 0$

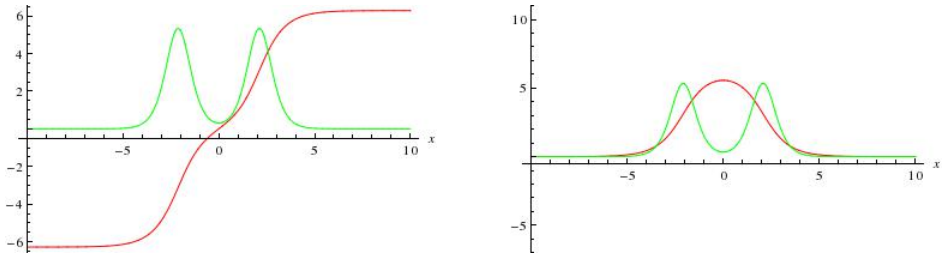

(d) $t = 3$

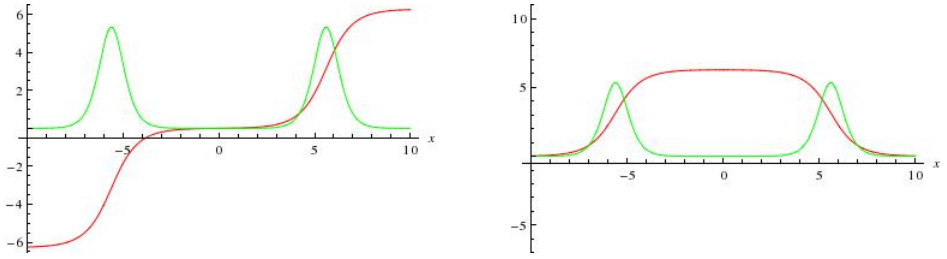

(e) $t = 10$

Figure 1.2: Plot showing the field (red curve) of the sine-Gordon kink and its energy density (green curve) of $\phi_{kk}(x,t)$ (left) and $\phi_{k\bar{k}}(x,t)$ (right) with $v = 0.5$.

in the left hand column of Figure 1.2, where we can see that the solitons approach each other, before repelling away again.

We can also obtain analytic solutions which describes the scattering of a kink with an antikink by choosing different β_1 and β_2 in the above construction. Choosing instead for $\beta_1 = -1/\beta$ and $\beta_2 = -\beta$ we get

$$\phi_{k\bar{k}}(x,t) = 4\arctan\left(\frac{\sinh(\gamma v t)}{v\cosh(\gamma v x)}\right) \tag{1.3.20}$$

We plot the field in the right hand column of Figure 1.2. We see that in this model the kink and anti-kink do not annihilate, but instead pass through each other, seemingly not interacting with each other.

A final example of kink scattering follows from that above for v imaginary. We take the combined transformation $v \mapsto iv\gamma$ and $\gamma \mapsto 1/\gamma$ to get solutions of the form

$$\phi_b(x,t) = 4\arctan\left(\frac{\sin(vt)}{v\gamma\cosh(x/\gamma)}\right). \tag{1.3.21}$$

We see that a kink and anti-kink form a bound state which is periodic in time. Such a solution is called a breather and is shown in Figure 1.3. This particular solution results in a stationary breather, since the breather is located at the origin, however it is trivial to construct a moving breather by a Lorentz boost of the solution.

Applying further Bäcklund transformations leads to more complicated systems such as sine-Gordon wobbles [7, 8] which are interactions of a kink and a breather. We shall see in a later chapter that the sine-Gordon model will play the role of an effective theory in a higher dimensional model we will study.

1.4 Skyrme model

The sine-Gordon model we have seen above is a suitable toy model for the more physically motivated Skyrme model and many of the basic features of the sine-Gordon model will appear in the Skyrme-type theories. The Skyrme model [9, 10] is a relativistic (3+1)-dimensional non-linear theory of pions that can be regarded as a low energy effective theory of Quantum Chromodynamics (QCD) in the limit of a large number of colours [11, 12]. This theory has topological soliton solutions called

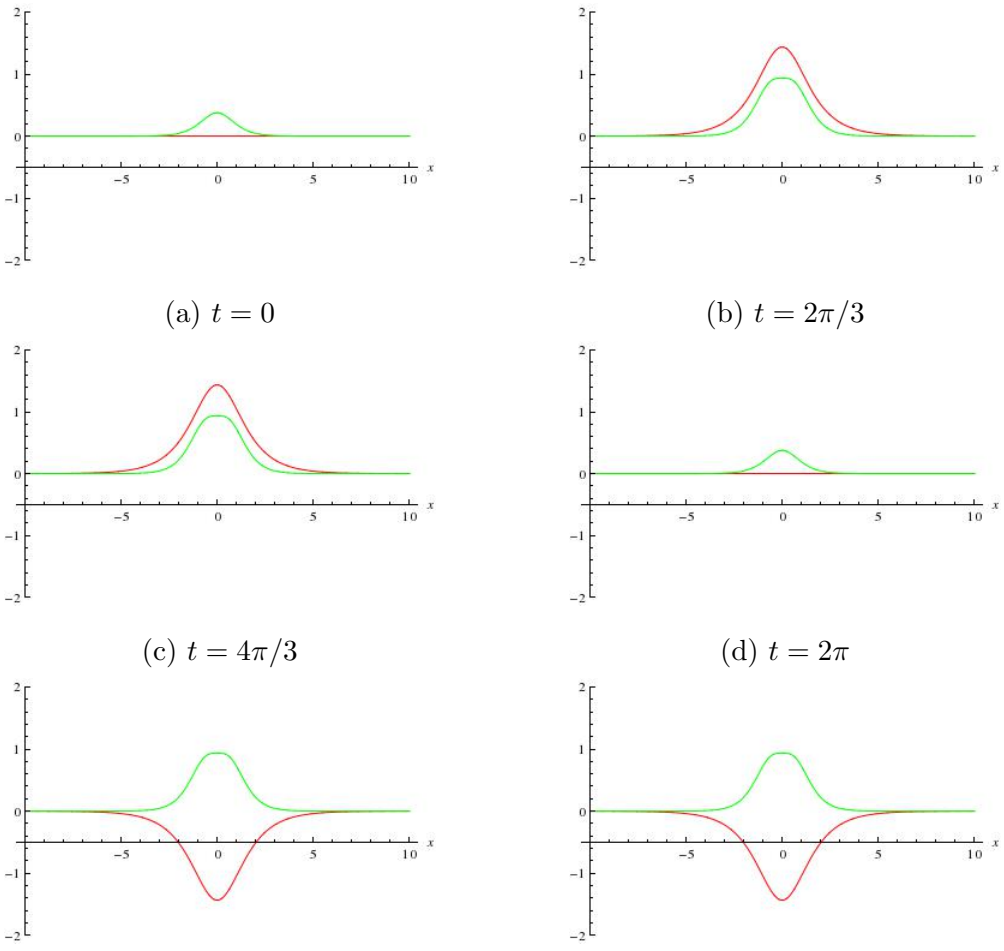

(a) $t = 0$ (b) $t = 2\pi/3$

(c) $t = 4\pi/3$ (d) $t = 2\pi$

(e) $t = 8\pi/3$ (f) $t = 10\pi/3$

Figure 1.3: Plot showing the field (red curve) of the sine-Gordon kink and its energy density (green curve) of $\phi_b(x,t)$ with $v = 0.5$. Note that the images show one period of the breather.

Skyrmions which represent baryons. The theory is defined in terms of a scalar field $U(\mathbf{x}, t) \in SU(2)$ called the Skyrme field, and is defined via the Lagrangian density

$$\mathcal{L}_{\text{Skyrme}} = \frac{F_\pi^2}{16} \operatorname{Tr}(\partial_\mu U \partial^\mu U^\dagger) + \frac{1}{32e^2} \operatorname{Tr}([\partial_\mu U U^\dagger, \partial_\nu U U^\dagger][\partial^\mu U U^\dagger, \partial^\nu U U^\dagger]), \quad (1.4.22)$$

where F_π is the pion decay constant and e is a dimensionless parameter, both of which are fixed by comparison with experiment. These parameters can be scaled away to give

$$\mathcal{L}_{\text{Skyrme}} = \frac{1}{2} \operatorname{Tr}(\partial_\mu U \partial^\mu U^\dagger) + \frac{1}{16} \operatorname{Tr}([\partial_\mu U U^\dagger, \partial_\nu U U^\dagger][\partial^\mu U U^\dagger, \partial^\nu U U^\dagger]), \quad (1.4.23)$$

where energy and length scales are $F_\pi/4e$ and $2/eF_\pi$ respectively. Introducing an $su(2)$-valued current $R_\mu = \partial_\mu U U^\dagger$ we see that we can write the Lagrangian as

$$\mathcal{L}_{\text{Skyrme}} = -\frac{1}{2} \operatorname{Tr}(R_\mu R^\mu) + \frac{1}{16} \operatorname{Tr}([R_\mu, R_\nu][R^\mu, R^\nu]). \quad (1.4.24)$$

This Lagrangian leads to the Skyrme field equation

$$\partial_\mu (R^\mu + \frac{1}{4}[R^\nu, [R_\nu, R^\mu]]) = 0. \quad (1.4.25)$$

For finite energy in the model one requires the field to go to a constant value at spatial infinity. For this we impose the boundary condition $U(x) \to \mathbf{1}_2$ as $|\mathbf{x}| \to \infty$ This one-point compactification of space leads to $U(\mathbf{x})$ being a map from the three-sphere to $SU(2)$. Since the group manifold of $SU(2)$ is the three-sphere we see that $U(\mathbf{x})$ is classified by the homotopy group $\pi_3(S^3) = \mathbb{Z}$ and are categorised by integer values given by the degree of the map. Explicitly we find the topological charge is given by

$$B = -\frac{1}{24\pi^2} \int \epsilon_{ijk} \operatorname{Tr}(R_i R_j R_k) \, d^3\mathbf{x}, \quad (1.4.26)$$

where B is a topological invariant which is identified with the baryon number.

We see that the form of the static energy following from (1.4.23) is of the correct form to avoid Derrick's theorem in three-dimensions. Even though we do not have a potential term in the theory, the energy scales under a spatial rescaling $\mathbf{x} \mapsto \mu\mathbf{x}$ as $\frac{1}{\mu}E_4 + \mu E_2$. Thus since each term scales in an opposite way there is a minimal energy at some finite μ. The term quartic in spatial derivatives, which we shall refer to as the Skyrme term, was introduced by Skyrme to support stable static solitons in the

theory. We note that although any term which is degree four or higher would have a similar effect on stablility this choice is unique in being of degree four, Lorentz invariant and which result in terms in the field equations that do not exceed second order in time derivatives.

We now write the Skyrme field in terms of the triplet of pion fields $\boldsymbol{\pi}$ as

$$U(\mathbf{x}) = \sigma + i\boldsymbol{\pi} \cdot \boldsymbol{\tau}, \tag{1.4.27}$$

where $\boldsymbol{\tau}$ are the Pauli matrices and σ is a scalar field to ensure that $U \in SU(2)$ via the constraint that

$$\sigma^2 + \boldsymbol{\pi} \cdot \boldsymbol{\pi} = 0. \tag{1.4.28}$$

We note that this defines σ up to a choice of sign that is determined by requiring that the field is continuous. Substituting (1.4.27) into the Skyrme Lagrangian and introducing the four-component unit vector $\boldsymbol{\phi} = (\pi_1, \pi_2, \pi_3, \sigma)$ we find that

$$\mathcal{L} = \partial_\mu \boldsymbol{\phi} \cdot \partial^\mu \boldsymbol{\phi} - \frac{1}{2}(\partial_\mu \boldsymbol{\phi} \cdot \partial^\mu \boldsymbol{\phi})^2 + \frac{1}{2}(\partial_\mu \boldsymbol{\phi} \cdot \partial_\nu \boldsymbol{\phi})(\partial^\mu \boldsymbol{\phi} \cdot \partial^\nu \boldsymbol{\phi}) + \lambda(1 - \boldsymbol{\phi} \cdot \boldsymbol{\phi}), \tag{1.4.29}$$

where λ is a Lagrange multiplier term to enforce the condition that $\boldsymbol{\phi}$ is a unit vector. We note that this is a modified $O(4)$ sigma model. This is useful since we will be concerned in this thesis with a lower dimensional model, the baby Skyrme model.

As in the sine-Gordon kink model, one can manipulate the static energy to find a bound in terms of the topological charge. It follows from equation (1.4.29) that the static energy is given by

$$E = \frac{1}{12\pi^2} \int \partial_i \boldsymbol{\phi} \cdot \partial_i \boldsymbol{\phi} + \frac{1}{2}(\partial_i \boldsymbol{\phi} \cdot \partial_i \boldsymbol{\phi})^2 - \frac{1}{2}(\partial_i \boldsymbol{\phi} \cdot \partial_j \boldsymbol{\phi})(\partial_i \boldsymbol{\phi} \cdot \partial_j \boldsymbol{\phi})\, d^3\mathbf{x}. \tag{1.4.30}$$

It is easiest to see the bound by writing the energy in terms of the strain tensor $D_{ij} = \partial_i \boldsymbol{\phi} \cdot \partial_j \boldsymbol{\phi}$, which has non-negative eigenvalues λ_1^2, λ_2^2 and λ_3^2 with the sign of the roots chosen such that $\lambda_1\lambda_2\lambda_3$ is positive (negative) if U is locally orientation preserving (reversing). It can then be shown that the energy density $\mathcal{E}$ and topological charge

density $\mathcal{B}$ can be expressed as

$$\begin{aligned}\mathcal{E} &= \frac{1}{12\pi^2}\left(\mathrm{Tr}(D) + \frac{1}{2}(\mathrm{Tr}(D)^2 - \mathrm{Tr}(D^2))\right) \\ &= \frac{1}{12\pi^2}(\lambda_1^2 + \lambda_2^2 + \lambda_3^2 + \lambda_1^2\lambda_2^2 + \lambda_2^2\lambda_3^2 + \lambda_1^2\lambda_3^2) \qquad (1.4.31)\\ \mathcal{B} &= \frac{1}{2\pi^2}\sqrt{\det(D)} = \frac{1}{2\pi^2}\lambda_1\lambda_2\lambda_3 \qquad (1.4.32)\end{aligned}$$

It then follows from the inequality

$$(\lambda_1 \pm \lambda_2\lambda_3)^2 + (\lambda_2 \pm \lambda_1\lambda_3)^2 + (\lambda_3 \pm \lambda_1\lambda_2)^2 \geq 0 \qquad (1.4.33)$$

that $E \geq |B|$ with equality only occurring when $|\lambda_1| = |\lambda_2| = |\lambda_3| = 1$ which only happens in the case where the map is an isometry, which is not possible since $\mathbb{R}^3$ is not isometric to S^3. Thus this bound cannot be saturated.

Since we cannot saturate the bound, there is no Bogomolny argument for analytic solutions to this theory. For the Skyrme model analytic solutions are not known, but much work has been undertaken computing these numerically [13, 14]. The forms which solutions take appear to be related to the platonic solids. For more details on the forms of these solutions we refer the reader to [4, 15].

The Skyrme Lagrangian (1.4.23) has an $SU(2) \times SU(2)$ symmetry relating to transformations $U \mapsto \mathcal{O}_1 U \mathcal{O}_2$ for $\mathcal{O}_i \in SU(2)$. The boundary condition imposed on the field breaks this symmetry to an $SO(3)$ given by $U \mapsto \mathcal{O}_1 U \mathcal{O}_1^\dagger$. In terms of the pion fields this corresponds to a symmetry $\boldsymbol{\pi} \mapsto M\boldsymbol{\pi}$ for $M \in SO(3)$. This symmetry of the field relates physically to the isospin.

As we can see from the form of the Lagrangian density (1.4.29), the pion fields of this theory are massless. An additional term can be added to the Lagrangian density (1.4.23) to give them a mass

$$\mathcal{L}_m = m_\pi^2 \,\mathrm{Tr}(U - \mathbf{1}_2). \qquad (1.4.34)$$

The effect of this mass term has also been studied [16] and it was found that the forms of the solutions were similar to those found in the massless case, however some qualitative differences were noted. Solutions appear flattened and for higher charges were seen to display a clustering into lower charge components, especially into those of charge three and four.

One issue with the Skyrme model is that the binding energy of baryons is overestimated in the model. Recently a number of different methods for trying to address this have been considered. These methods include adding terms which are higher order in derivatives [17, 18], the addition of vector mesons coupled to the Skyrme field [19] as well as particular forms of potential term [18, 20].

1.5 Baby Skyrme model

The baby Skyrme model is a modified $O(3)$ sigma model in (2+1)-dimensional space and is a lower dimensional analogue of the full Skyrme model. As well as being a toy model of the Skyrme model, so having links with QCD and being a useful testing ground for aspects of Skyrmions, the baby Skyrme model has been considered in its own right as a model of condensed matter systems such as ferromagnetic quantum Hall systems [21] and chiral ferromagnets [22]. We discuss these condensed matter systems in more detail in Chapter 3. The theory is described by a Lagrangian analogous to that for the full Skyrme model as we have seen above,

$$\mathcal{L}_{BS} = \frac{1}{2}\partial_\mu \boldsymbol{\phi} \cdot \partial^\mu \boldsymbol{\phi} - \frac{\kappa^2}{4}(\partial_\mu \boldsymbol{\phi} \times \partial_\nu \boldsymbol{\phi}) \cdot (\partial^\mu \boldsymbol{\phi} \times \partial^\nu \boldsymbol{\phi}) - V, \tag{1.5.35}$$

where κ^2 and m^2 are parameters of the theory, $\boldsymbol{\phi}(\mathbf{x}, t)$ is a unit three-component vector and V is a non-zero potential term dependent on $\boldsymbol{\phi}(\mathbf{x}, t)$. We see that for finite energy we again require the field to approach a vacuum of this potential. Requiring the field to approach a particular vacuum value at infinity results in a one-point compactification of space, so topologically we find that $\boldsymbol{\phi} : S^2 \to S^2$. Thus it has an associated integer since the homotopy group is given by $\pi_2(S^2) = \mathbb{Z}$. As we know, we also need to avoid Derrick's theorem to allow for stable static solutions. Under a spatial rescaling $\mathbf{x} \mapsto \mu\mathbf{x}$ we find that $E \mapsto \frac{1}{\mu^2}E_4 + E_2 + \mu^2 E_0$. We see that in this case we require a non-zero potential term which scales inversely to the Skyrme term to be able to avoid Derrick's theorem and allow stable solutions for a given topological charge. It can also be found via Derrick's theorem that the scale of the solitons of the theory is proportional to $\sqrt{\kappa/m}$, where m^2 is an overall multiplicative constant of the potential V.

There is no obvious choice of potential for this theory. The standard term to include is derived from the mass term in the Skyrme model to give a mass to the pions. Explicitly this is given by

$$V = m^2(1 - \phi_3) \tag{1.5.36}$$

in the baby Skyrme model. We see that this gives mass to the ϕ_1 and ϕ_2 components if we consider them as a perturbation from the vacuum field. However this choice of potential is not unique, and a range of other potentials has been examined. The choice of potential changes the appearance of the solitons which result from the theory immensely, as we shall see in more detail in a later chapter.

As with the full model the homotopy class of the map is given by the topological charge. Since the map is between spaces of equal dimension this is given by a topological degree,

$$B = -\frac{1}{4\pi}\int \boldsymbol{\phi}\cdot(\partial_1\boldsymbol{\phi}\times\partial_2\boldsymbol{\phi})\,\mathrm{d}^2\mathbf{x}. \tag{1.5.37}$$

A Bogomolny bound for the theory can be found from the static energy which follows from (1.5.35) by noting that

$$\begin{aligned}
E &= \int\left(\frac{1}{2}\partial_i\boldsymbol{\phi}\cdot\partial_i\boldsymbol{\phi} + \frac{\kappa^2}{4}(\partial_i\boldsymbol{\phi}\times\partial_j\boldsymbol{\phi})\cdot(\partial_i\boldsymbol{\phi}\times\partial_j\boldsymbol{\phi}) + V\right)\mathrm{d}^2\mathbf{x}\\
&\geq \int\frac{1}{2}(\partial_i\boldsymbol{\phi}\cdot\partial_i\boldsymbol{\phi})\,d^2\mathbf{x}\\
&= \int\frac{1}{4}(\partial_i\boldsymbol{\phi}\pm\epsilon_{ij}\boldsymbol{\phi}\times\partial_j\boldsymbol{\phi})\cdot(\partial_i\boldsymbol{\phi}\pm\epsilon_{ik}\boldsymbol{\phi}\times\partial_k\boldsymbol{\phi}) \pm \frac{1}{2}\epsilon_{ij}\boldsymbol{\phi}\cdot(\partial_i\boldsymbol{\phi}\times\partial_j\boldsymbol{\phi})\,d^2\mathbf{x}\\
&\geq \pm\int\boldsymbol{\phi}\cdot(\partial_1\boldsymbol{\phi}\times\partial_2\boldsymbol{\phi})\,d\mathbf{x}\\
&= 4\pi|B|
\end{aligned} \tag{1.5.38}$$

where ϵ_{ij} is the totally antisymmetric tensor and the sign is chosen such that one gets the modulus of the topological charge. We have also used the fact that since $\boldsymbol{\phi}\cdot\boldsymbol{\phi} = 1$ we have that $\partial_i\boldsymbol{\phi}\cdot\boldsymbol{\phi} = 0$. We see that since this bound relies solely on the first term of the energy it can not be saturated by any non-trivial fields and so the energy must exceed this bound.

We now concern ourselves with the asymptotic interactions of two unit charge baby Skyrmions with the standard potential as was first considered in [23, 24]. For

convenience for this study we shall set $\kappa = 1$, which can always be made to be such by a rescaling of energy and length. Consider a static field of the form

$$\boldsymbol{\phi}(\mathbf{x}) = (\sin f \cos(\theta - \chi), \sin f \sin(\theta - \chi), \cos f), \tag{1.5.39}$$

for polar coordinates (r, θ), arbitrary angle χ and $f(r)$ is a function satisfying $f(0) = \pi$ and $\lim_{r\to\infty} f = 0$. This field is of the right form to have unit charge and has the same symmetry as the energy density of the theory. The energy of such a static field is then

$$E = 2\pi \int \left(\frac{1}{2} f'^2 + \frac{\sin^2 f}{2r^2}(1 + f'^2) + m^2(1 - \cos f) \right) r \, dr \tag{1.5.40}$$

Considering a variation of this energy leads one to the Euler-Lagrange equations for f given by

$$\left(r + \frac{\sin^2 f}{r} \right) f'' + \left(1 - \frac{\sin^2 f}{r^2} + \frac{f' \sin f \cos f}{r} \right) f' - \frac{\sin f \cos f}{r} - r m^2 \sin f = 0 \tag{1.5.41}$$

The behaviour of the function $f(r)$ can be considered for large r, so $\cos f \sim 1$ and $\sin f \sim f$ and by linearising in f it is found that it obeys

$$f'' + \frac{1}{r} f' - \left(\frac{1}{r^2} + m^2 \right) f = 0 \tag{1.5.42}$$

which has solutions which are of the form of modified Bessel functions, so we can write

$$f(r) \sim \frac{pm}{2\pi} K_1(mr) \tag{1.5.43}$$

where K_1 is the modified Bessel function and p is a constant. Thus it follows that the asymptotic form of the field is given by

$$\boldsymbol{\phi}^{(1)} = \frac{pmK_1(mr)}{2\pi} (\cos(\theta - \chi), \sin(\theta - \chi), 1). \tag{1.5.44}$$

If we write $\boldsymbol{\phi}^{(1)} = \boldsymbol{\phi}_\infty + \boldsymbol{\varphi}^{(1)}$, where $\boldsymbol{\phi_\infty} = (0, 0, 1)$ is the vacuum field. Then introducing $\hat{\mathbf{x}} = \mathbf{x}/r$ and the orthogonal vectors $\mathbf{p}_1 = p(\cos\chi_1, \sin\chi_1)$ and $\mathbf{p}_2 = p(-\sin\chi_1, \cos\chi_1)$ we find that

$$\varphi_a^{(1)} = \frac{m}{2\pi} \mathbf{p}_a \cdot \hat{\mathbf{x}} K_1(mr) = -\frac{1}{2\pi} \mathbf{p}_a \cdot \nabla K_0(mr) \tag{1.5.45}$$

for $a = 1, 2$, and where we have used the property of modified Bessel functions that $\frac{d}{dz}K_0(z) = -K_1(z)$ for the second equality.

We now consider the situation where a further unit charge soliton is placed at $\mathbf{R}$ with phase χ_2. These are assumed to be at large separation, with $R = |\mathbf{R}| \gg 1/m$. There then exists a field $\varphi^{(2)}$ analogous to $\varphi^{(1)}$ which satisfies

$$\varphi_a^{(2)} = -\frac{1}{2\pi}\mathbf{q}_a \cdot \nabla K_0(m|\mathbf{x} - \mathbf{R}|) \tag{1.5.46}$$

for $\mathbf{q}_1 = p(\cos\chi_2, \sin\chi_2)$ and $\mathbf{q}_2 = p(-\sin\chi_2, \cos\chi_2)$. If we assume these dipoles $\mathbf{p}_1$ and $\mathbf{q}_1$, and dipoles $\mathbf{p}_2$ and $\mathbf{q}_2$ interact via a scalar field theory obeying the Klein-Gordon equation with mass m it is known that the interaction between the doublets $\mathbf{p}_a$ and $\mathbf{q}_a$ is

$$\begin{aligned} W &= \sum_{a=1,2} \frac{1}{2\pi}(\mathbf{p}_a \cdot \nabla)(\mathbf{q}_a \cdot \nabla)K_0(mR) \\ &= \frac{p^2}{2\pi}\cos(\chi_1 - \chi_2)\partial_\mu\partial^\mu K_0(mR) \\ &= \frac{p^2m^2}{2\pi}\cos(\chi_1 - \chi_2)K_0(mR) \end{aligned} \tag{1.5.47}$$

where $|\mathbf{R}| = R$. The first equality follows from the definitions of $\mathbf{p}_a$ and $\mathbf{q}_a$, while the second follows from $K_0(mr)$ being the Green's function of the Klein-Gordon equation

$$(\partial_\mu\partial^\mu - m^2)K_0(mr) = -2\pi\delta^{(2)}(\mathbf{x}) \tag{1.5.48}$$

and since we are are interested in large separation we can exclude the delta-function term. Thus we see that for solitons with relative internal phase of π that the solitons will be maximally attractive.

As we saw above, two solitons can be attractive and therefore it follows that we can have multi-soliton states within the theory. These have been studied in detail for the standard potential [23, 25, 26]. An interesting feature which was found to occur is that for high charges chains of solitons are preferred, with each component rotated by π relative to neighbouring solitons [27].

1.6 Skyrme-Faddeev model

We now turn our attention to the Skyrme-Faddeev model [28, 29]. This is a (3+1)-dimensional modified $O(3)$ sigma model with a Skyrme term included. It has topo-

logical soliton solutions which take the form of knots and links. The model can be thought of as arising as a restriction of the target space of the (3+1)-dimensional Skyrme model when the field $U(\mathbf{x}, t)$ is restricted to taking values on an equatorial two-sphere of $SU(2)$. This can be thought of as restricting to considering fields with $\sigma = 0$ when the pions fields are made explicit, so $U = i\boldsymbol{\pi} \cdot \boldsymbol{\tau}$ with $\boldsymbol{\pi} \cdot \boldsymbol{\pi} = 1$. Alternatively, one can think of these topological solitons as strings formed from baby Skyrmions located in the plane transverse to the string, and so can be thought of as being baby Skyrmions which are knotted in three dimensions.

The Skyrme-Faddeev model has potential links to low-energy QCD, with it having been suggested that this model may describe glueballs [30], and applications have also been suggested in condensed matter systems [31]. However, these links are somewhat controversial and it has been shown recently [32] that in two-component superconductors outside specific parameter choices the topological stability of the Skyrme-Faddeev model approximation is destroyed. Nonetheless the Skyrme-Faddeev model is a good testing ground for other theories where knotted fields have been found experimentally.

The model is described by Lagrangian density

$$\mathcal{L}_{SF} = \partial_\mu \boldsymbol{\phi} \cdot \partial^\mu \boldsymbol{\phi} - \frac{1}{2}(\partial_\mu \boldsymbol{\phi} \times \partial_\nu \boldsymbol{\phi}) \cdot (\partial^\mu \boldsymbol{\phi} \times \partial^\nu \boldsymbol{\phi}) \tag{1.6.49}$$

where $\boldsymbol{\phi}$ is a three-component unit vector. We see that this is of the same form as for the baby Skyrme model, although now we are in an extra spatial dimension and so we no longer require a potential term to evade Derrick's theorem. The Lagrangian density leads to the static energy

$$E = \frac{1}{32\pi^2\sqrt{2}} \int \partial_i \boldsymbol{\phi} \cdot \partial_i \boldsymbol{\phi} + \frac{1}{2}(\partial_i \boldsymbol{\phi} \times \partial_j \boldsymbol{\phi}) \cdot (\partial_i \boldsymbol{\phi} \times \partial_j \boldsymbol{\phi})\, d^3x. \tag{1.6.50}$$

for a particular choice of scaling which will become evident later. Under a spatial rescaling $\mathbf{x} \mapsto \mu\mathbf{x}$ we see that the static energy relating to Lagrangian density (1.6.49) scales as $E \mapsto \frac{1}{\mu}E_4 + \mu E_2$, and so each term scales in the opposite way, which allows for stationary points of the energy for a finite scale μ.

For the field to have a finite energy it must tend towards a constant vector at spatial infinity, which we choose to be $\lim_{|\mathbf{x}|\to\infty} \boldsymbol{\phi}(\mathbf{x}) = \boldsymbol{\phi}_\infty = (0, 0, 1)$ without loss of

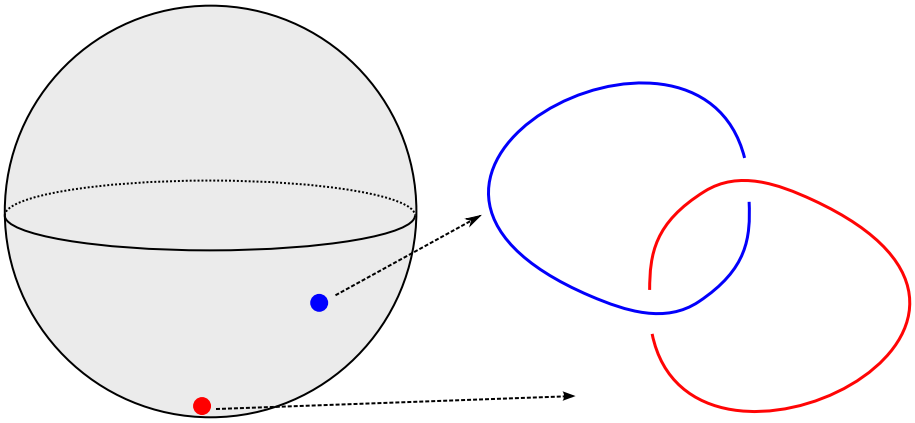

Figure 1.4: A schematic representation of the preimages of two distinct points on the target two-sphere relating to two curves. In this case we see that they have Hopf charge $Q = 1$ since they are linked once.

generality. This identification leads to a one-point compactification of physical space so the field is a map $\boldsymbol{\phi} : S^3 \to S^2$ and so has related homotopy group $\pi_3(S^2) = \mathbb{Z}$.

Since the map is between spaces of different dimensions, the topological charge can not simply be the degree of the map, as is the case for other Skyrme theories we have seen. Instead we find that the topological charge is given by the Hopf invariant. Let f be the pullback under $\boldsymbol{\phi}$ of the area two-form on the target S^2. Then the triviality of the second cohomology group of S^3 means that f must be exact, say $f = da$, and the Hopf charge is given by

$$Q = \frac{1}{4\pi^2} \int_{S^3} f \wedge a. \tag{1.6.51}$$

The Hopf charge can not be written as a density which is local in terms of $\boldsymbol{\phi}$, and so it is useful to think of it in a more intuitive geometric way. The preimages of points of S^2 are generically (a collection of) closed curves. The Hopf charge is then given by the (signed) linking number of the preimage of two distinct points of the target S^2 [33]. A sketch of this is shown in Figure 1.4 for the preimages of two points for a configuration with $Q = 1$. The sign of the linking number of these curves depends on the relative orientation of the curves. It is defined for two curves A and B as

$$\text{link}(A, B) = \sum_{D \cap B} \pm 1, \tag{1.6.52}$$

where D is a smooth surface with boundary A and the sign is determined from the

(a) $\ell = +1$ (b) $\ell = -1$

Figure 1.5: Linking number corresponding to a given crossing.

relative orientations of D and B. In practice we take the points on the two-sphere to be close together such that the relative orientation follows from continuity of the field. Considering a projection of the curve on to a plane, the linking number is then given by $\frac{1}{2}\sum_{c\in C}\ell(c)$, where C is the set of all crossings of the two curves, and $\ell(c)$ is ± 1 according to the rules given in Figure 1.5. We note that here we follow the sign convention of [34] for consistency, however this is the opposite to the usual sign convention. In the Skyrme-Faddeev model solutions with positive and negative Hopf charge are related by a spatial reflection and so this convention makes no real impact upon the form of solutions.

As in the other models seen already, the static energy function relating to Lagrangian density can be bounded below by a term dependent on the topological charge Q. It is known that the energy functional (1.6.50) obeys the Vakulenko-Kapitanskii bound [35]

$$E \geq c\,|Q|^{3/4}, \tag{1.6.53}$$

where the sublinear growth of the energy is due to the use of complicated Sobolev inequalities rather than a Bogomolny bound as we have seen previously. This sublinear growth of the energy can be understood physically as a consequence of the creation of additional charge through the knotting and linking of solitons. The inequality has been proven for $c = (3/16)^{3/8} \approx 0.534$ [36], although it is believed this value is not optimal.

To derive (1.6.53) we follow the derivation of [37]. Firstly write $\mathcal{E}_2 = \partial_i\boldsymbol{\phi}\cdot\partial_i\boldsymbol{\phi}$ and $\mathcal{E}_4 = \frac{1}{2}(\partial_i\boldsymbol{\phi}\times\partial_j\boldsymbol{\phi})\cdot(\partial_i\boldsymbol{\phi}\times\partial_j\boldsymbol{\phi})$. From Sobolev type equalities (see [38] for a derivation) we see that

$$|Q|^{3/2} \leq K\left(\int_{\mathbb{R}^3}\mathcal{E}_4\,d^3\mathbf{x}\right)\left(\int_{\mathbb{R}^3}\sqrt{\mathcal{E}_4}\,d^3\mathbf{x}\right), \tag{1.6.54}$$

for $K = (32\pi^4 3^{3/4})^{-1}$. We further find that

$$\mathcal{E}_4 \leq \frac{1}{4}\mathcal{E}_2^2. \tag{1.6.55}$$

To see this, define the 3×3 matrix $D_{ab} = \partial_i \phi_a \partial_i \phi_b$ which has one zero eigenvalue corresponding to eigenvector ϕ_a. Let the remaining two eigenvalues be λ_1 and λ_2, then $\mathcal{E}_2 = \lambda_1 + \lambda_2$ and $\mathcal{E}_4 = \lambda_1 \lambda_2$ where this follows from

$$\begin{aligned}
\mathcal{E}_4 &= \frac{1}{2}\Big[(\partial_i \boldsymbol{\phi} \cdot \partial_i \boldsymbol{\phi})(\partial_j \boldsymbol{\phi} \cdot \partial_j \boldsymbol{\phi}) - (\partial_i \boldsymbol{\phi} \cdot \partial_j \boldsymbol{\phi})(\partial_i \boldsymbol{\phi} \cdot \partial_j \boldsymbol{\phi})\Big] \\
&= \frac{1}{2}\Big[(\partial_i \phi_a \partial_i \phi_a)(\partial_j \phi_b \partial_j \phi_b) - \partial_i \phi_a \partial_i \phi_b \partial_j \phi_b \partial_j \phi_a\Big] \\
&= \frac{1}{2}\Big[\operatorname{Tr}(D)^2 - \operatorname{Tr}(D^2)\Big].
\end{aligned} \tag{1.6.56}$$

The inequality above then follows trivially. Finally, by a simple completion of the square one finds that

$$E \geq \frac{1}{16\pi^2\sqrt{2}} \left(\int_{\mathbb{R}^3} \mathcal{E}_2 \, d^3\mathbf{x}\right)^{1/2} \left(\int_{\mathbb{R}^3} \mathcal{E}_4 \, d^3\mathbf{x}\right)^{1/2}. \tag{1.6.57}$$

These three inequalities then lead straightforwardly to the Vakulenko-Kapitanskii bound (1.6.53).

It has been conjectured by Ward [37] that the value of K can be improved upon to find a tighter bound on the energy, such that $c = 1$ should be the optimal value. This is done by considering related maps from the three-sphere of some finite radius to the unit two-sphere.

In the following chapters we present research undertaken for this doctoral study. In Chapter 2 we look at a baby Skyrme model in which the choice of potential breaks the $O(2)$ of the model to a discrete symmetry given by the dihedral group. We study numerically the form of static multi-solitonic solutions for a variety of dihedral groups. We then consider the impact that such a breaking of the symmetry will have on the dynamics of such broken baby Skyrmions. This chapter is based upon publication [1].

In Chapter 3 we discuss in more detail the link between the baby Skyrmion and condensed matter systems. We propose and investigate a model in which there is no Skyrme term. Instead, stability of solutions comes from the fact that they are located on domain walls. We consider this stability and then investigate the

scattering behaviour of solitons in this theory. Here we make links with an effective theory given by a sine-Gordon theory. This chapter is based upon publication [2].

Chapter 4 is concerned with the Skyrme-Faddeev model. Certain forms of knotted field solutions, called hopfions, are known within the model. In this chapter we construct fields with the form of a new class of knots and show that they are present as stable solutions within the model. We present the first known hopfions which are not of the form of torus knots or links thereof, but instead take the form of cable knots and hyperbolic knots. Chapter 4 is based upon the preprint [3]

Finally, in Chapter 5 we present current research focussing on an approximation to the Skyrme-Faddeev model in which solutions are considered as elastic rods. We shall apply the techniques of this model to try to understand the form of knots found in the full model and understand why fields are knotted in certain ways in the Skyrme-Faddeev model.

Chapter 2

Broken baby Skyrmions

Although the Skyrme model is seen as an effective theory of QCD, and so the baby Skyrme model as a toy model of this, these models exhibit no classical colour dependent behaviour. The number of colours, $N \in \mathbb{Z}$, appears in the Skyrme model only on quantisation where it appears in the coefficient of an additional term which must be added to the classical Lagrangian, the Wess-Zumino term. For a classical theory the Wess-Zumino term does not contribute to the energy however it is important in the quantum theory. In this chapter we wish to consider a particular form of the potential term with the aim of introducing a classical colour dependence to the baby Skyrme model.

As we have seen in the previous chapter, the baby Skyrme model has no obvious choice for the potential term, and this choice can have a large impact upon the symmetry of solutions in the theory. We see that the first two terms of the Lagrangian density for the baby Skyrme model (1.5.35) have an O(3) symmetry, since for $M \in O(3)$ these terms of the Lagrangian are symmetric under $\boldsymbol{\phi} \mapsto M\boldsymbol{\phi}$. The identification of the field at spatial infinity to a vacuum value for a given potential will break this symmetry to $O(2)$, while the symmetries of the potential may break this symmetry further. The standard potential [23, 24] for the model, $V = m^2(1 - \phi_3)$, as we have introduced previously, retains this $O(2)$ symmetry. Solutions to the static field equations for charges one and two are axially symmetric, as can be seen from the plots of their energy density in Figure 2.1. In this Chapter, unless otherwise stated, for numerical simulations we have taken $\kappa^2 = m^2 = 1$.

Figure 2.1: Energy density plots of the charge one and two baby Skyrmions with the standard potential $V = m^2(1 - \phi_3)$.

Figure 2.2: Energy density plots of the charge one and two baby Skyrmions with the new baby Skyrme potential $V = \frac{m^2}{2}(1 - \phi_3^2)$.

Other potentials have been also considered, such as the new baby Skyrmion potential [25] $V = \frac{m^2}{2}(1-\phi_3^2)$, a potential that is known to be relevant in ferromagnet systems of the Ising type. This does not break the symmetry any further, so this theory also has $O(2)$ symmetry. Numerical simulations show that the solitons with topological charge one and two are again axially symmetric, as can be seen in Figure 2.2. More recently models which further break the symmetry have also been considered. The easy plane potential [39], $V = \frac{m^2}{2}\phi_1^2$, which is known to be applicable to antiferromagnets and breaks the symmetry to the discrete dihedral group D_2. This follows from the fact that a point on the orbit of the obvious $O(2)$ symmetry of the potential must be identified as the value the field takes at spatial infinity so further breaking the symmetry to D_2. Ward [40] has also considered the potential

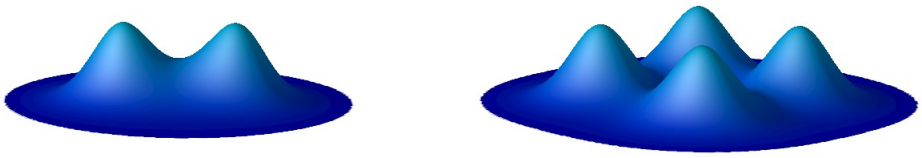

Figure 2.3: Energy density plots of the charge one and two baby Skyrmions with the easy plane potential $V = \frac{m^2}{2}\phi_1^2$.

Figure 2.4: Energy density plots of the charge one and two baby Skyrmions with the Ward potential $V = \frac{m^2}{2}(1-\phi_3^2)(1-\phi_1^2)$.

$V = \frac{m^2}{2}(1-\phi_3^2)(1-\phi_1^2)$ which also breaks the symmetry group to D_2. We can see the energy density of the charge one and charge two solitons in Figures 2.3 and 2.4 for the easy plane and Ward potentials respectively. We can see that in both these models the unit charge solitons have two distinct peaks to the energy density and for the charge two solution we find four distinct peaks.

In this chapter we are interested in a model that has a classical colour dependence, which uses a potential that has been proposed by Jäykkä *et al.* [41], the explicit form of which we shall give in the following section. In the theory with this potential the symmetry is broken to the dihedral group D_N and similarly to the easy plane and Ward potentials the resulting unit charge solutions have energy density formed of N distinct lumps, which we shall refer to as partons. We will follow the

notation of paper [41] and hence refer, somewhat suggestively, to the system for a particular choice of N as the N-colour system. For the three-colour theory it was found that the energy density of solutions was arranged with three partons for each unit of topological charge the field had. It was found that partons were located on the vertices of equilateral triangles and that for multi-soliton solutions these equilateral triangles were joined along edges. Links were thus identified between the structure of the higher charge solitons and polyiamonds - the mathematical structures formed from joining equilateral triangles along edges. This structure was seen for a number of topological charges. The paper left interesting open questions as to how this would generalise for systems with a greater number of colours.

In this chapter we consider this baby Skyrme model with discrete symmetry, and examine static soliton field configurations for a range of N-colour systems. By examining the structure of the static solutions, we consider how the connection to polyiamonds generalises for higher-colour systems to polyforms. Finally we go on to consider the dynamics of these solitons and ascertain how their structure impacts upon the known scattering behaviour observed in the baby Skyrme model with unbroken symmetry.

2.1 The Model

The baby Skyrme model is a modified non-linear sigma model, described by the Lagrangian density of the baby Skyrme model (1.5.35) for three-component unit vector $\boldsymbol{\phi}(\mathbf{x}, t)$. We fix the potential term for the remainder of this chapter as

$$V[\boldsymbol{\phi}] = m^2 \left|1 - (\phi_1 + i\phi_2)^N\right|^2 (1 - \phi_3), \tag{2.1.1}$$

for some integer $N \geq 2$, which was first considered for the $N = 3$ case by Jäkkä *et al.* [41]. Note that up to quadratic order in ϕ_1 and ϕ_2 this reduces to the standard pion mass potential. Hence physically the fields ϕ_1 and ϕ_2 are massive fields with mass given by the constant m, as with the standard potential. This choice of potential breaks the $O(3)$ symmetry of the system to the dihedral group D_N, generated by rotation $(\phi_1 + i\phi_2) \to (\phi_1 + i\phi_2)e^{2\pi i/N}$ and reflection $\phi_2 \to -\phi_2$. This choice of

potential has vacua at $\boldsymbol{\phi} = (0, 0, 1)$ and at the Nth roots of unity on the $\phi_3 = 0$ equatorial circle. The vacuum at spatial infinity is chosen to be the vacuum value

$$\boldsymbol{\phi}_\infty = \lim_{|\mathbf{x}|\to\infty} \boldsymbol{\phi}(\mathbf{x}, t) = (0, 0, 1). \tag{2.1.2}$$

This choice does not further restrict the symmetry of the model since the generators of the dihedral group are independent of ϕ_3. The energy of this baby Skyrme model then can be seen to have the form,

$$E = \int \left(\frac{1}{2}\dot{\boldsymbol{\phi}} \cdot \dot{\boldsymbol{\phi}} + \frac{\kappa^2}{2}(\dot{\boldsymbol{\phi}} \times \partial_i \boldsymbol{\phi}) \cdot (\dot{\boldsymbol{\phi}} \times \partial_i \boldsymbol{\phi}) \right) \mathrm{d}^2\mathbf{x} + \int \left(\frac{1}{2}\partial_i \boldsymbol{\phi} \cdot \partial_i \boldsymbol{\phi} + \frac{\kappa^2}{4} (\partial_i \boldsymbol{\phi} \times \partial_j \boldsymbol{\phi}) \cdot (\partial_i \boldsymbol{\phi} \times \partial_j \boldsymbol{\phi}) + V[\boldsymbol{\phi}] \right) \mathrm{d}^2\mathbf{x}, \tag{2.1.3}$$

where Latin indices run over spatial dimensions ($i = 1, 2$). The field equation that follows from the Lagrangian is,

$$-\frac{\delta V}{\delta \boldsymbol{\phi}} - \partial_\mu \partial^\mu \boldsymbol{\phi} + \kappa^2 \left[\partial_\mu \partial^\mu \boldsymbol{\phi} (\partial_\nu \boldsymbol{\phi} \cdot \partial^\nu \boldsymbol{\phi}) + \partial_\mu \boldsymbol{\phi} (\partial_\nu \boldsymbol{\phi} \cdot \partial^\mu \partial^\nu \boldsymbol{\phi}) - \partial_\mu \partial_\nu \boldsymbol{\phi} (\partial^\mu \boldsymbol{\phi} \cdot \partial^\nu \boldsymbol{\phi}) - \partial_\mu \boldsymbol{\phi} (\partial^\mu \boldsymbol{\phi} \cdot \partial_\nu \partial^\nu \boldsymbol{\phi}) \right] + \lambda \boldsymbol{\phi} = 0, \tag{2.1.4}$$

where λ is a Lagrange multiplier to enforce the condition that $\boldsymbol{\phi} \cdot \boldsymbol{\phi} = 1$. The field equation is highly non-linear, and to study the behaviour of the system we must resort to numerical techniques.

2.2 Static broken baby Skyrmions

In this section we specialise to the static case and examine the structure of (local) minimal energy solutions. The only work to date is for the three-colour system [41]. We shall recreate and then extend these findings, as well as examining the static solutions for higher-colour systems.

To find these soliton solutions we use an energy-minimising gradient flow algorithm on a square grid with $(501)^2$ grid points and lattice spacing $\Delta x = 0.04$, choosing to set $\kappa = m = 1$. Spatial derivatives are approximated using fourth-order finite difference methods while at the boundary of our grid the field is fixed to be the vacuum at spatial infinity $\boldsymbol{\phi}_\infty = (0, 0, 1)$. For all our simulations the topological

charge, when computed numerically, gives an integer value to five significant figures, indicating the accuracy of the results.

The gradient-flow algorithm requires an initial approximation to the static soliton. Consider the field configuration

$$\boldsymbol{\phi} = (\sin(f)\cos(B\theta), \sin(f)\sin(B\theta), \cos(f)), \tag{2.2.5}$$

for polar coordinates r and θ, and where f is a monotonically decreasing function of r. The boundary conditions of the field imply that we require f to satisfy that $f(0) = \pi$ and $f(R) = 0$, where the circle of radius $r = R$ lies inside the numerical grid. Outside this radius the rest of the grid is set to the vacuum $\boldsymbol{\phi}_\infty$. We can see that this describes a field on the grid with topological charge B, and so for a suitable choice of f this gives us our initial approximation. Although it is possible to solve the axially symmetric ansatz numerically for the specific form of f which minimises the energy, we use a linearly decreasing function since the additional energy related to this aids the numerical gradient flow procedure. We note that this initial approximation has the maximal symmetry D_{NB}, in the sense that the spatial rotation $\theta \to \theta + 2\pi/NB$ can be compensated for by global rotation symmetry, while the reflection $\theta \to -\theta$ can be balanced by a global reflection.

To find solutions with reduced symmetry we introduced a symmetry breaking perturbation to the above initial conditions. Once a pattern was discernible for these lower symmetry forms, we also used a product ansatz for our initial conditions with which we placed single unit charge solitons about our grid and then performed our gradient flow procedure.

Applying the energy minimisation algorithm to the initial condition given by equation (2.2.5) with $B = 1$ we obtain the unit charge soliton for a range of N. Plots of the energy density for $N = 3$, 4 and 5 are shown in Figure 2.5 with two different views. In the first row we present the energy density as a surface while in the second row we present this in the two-dimensional physical space and colour the value of the energy density. From these we see that the energy density is arranged in N lumps or partons, as we expect in analogy with the models with the easy plane and Ward potentials. We note that for all theories considered here that all unit charge solitons have the maximal symmetry of the ansatz, D_N. The unit charge

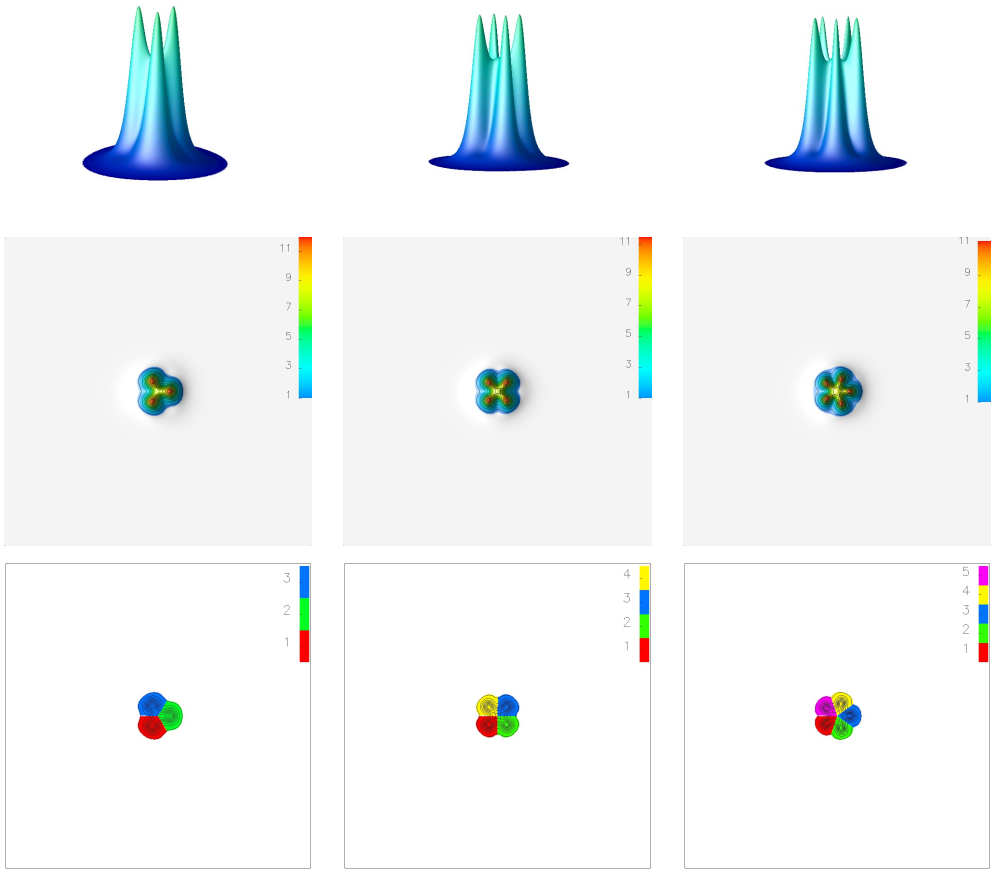

(a) $N = 3$, $B = 1$ (b) $N = 4$, $B = 1$ (c) $N = 5$, $B = 1$

Figure 2.5: Energy density plots of the single soliton solutions for (a) $N = 3$, (b) $N = 4$ and (c) $N = 5$. A surface of the energy density is shown in the top image, while the middle image is coloured based on the energy density and the bottom image is coloured based on the segment in which the point lies in the target space.

broken baby Skyrmions have energy 24.79, 34.58 and 34.41 for three, four and five colours respectively. If we were to plot the topological charge density rather than the energy density then the images would be qualitatively similar, again having distinct peaks in the same locations. Thus we can think of each parton contributing $1/N$ of the topological charge to the solution. Since fields must have an integer topological charge these partons must be topologically confined.

In the following we use the identification of each parton as a component of the unit charge by colouring each parton of the energy density a different colour depending on which segment of the two-sphere it lies in, dependent on its angle in

the ϕ_1, ϕ_2 plane. We use the vacua of the potential lying on the $\phi_3 = 0$ equator to define the boundary of the N segments of the target two sphere. We then colour the field using this to make the underlying colour structure more evident. This can be seen for the unit charge solitons in the final row of Figure 2.5. We will use this colouring in all further plots of our solutions. In these plots we show the entire numerical grid so all solutions are shown to scale. This also makes it clear that solutions are suitably far away from the numerical boundary so solutions should not be affected by the numerical procedures used.

For fields with topological charge greater than one we know that we should expect multi-soliton solutions, since two baby Skyrmions are attractive, and maximally attractive when there is a relative rotation of π between them. This fact follows analogously to the case where the symmetry is unbroken [24] since the form of the potential (2.1.1) reduces to the standard potential up to quadratic order in ϕ_1 and ϕ_2, and so the asymptotic fields are the same as those for the standard potential. Since two unit Skyrmions with suitable relative phase are attractive, bound states of solitons exist and in fact we find a number of (local) energy minima which are bound states. We tabulate the different symmetry groups and energy values of these local energy minima for each value of the topological charge in Table 2.1, 2.2, 2.3 and 2.4 for $N = 3$, 4 ,5 and 6 respectively. The energy density of the fields for these multi-solitons are also plotted in Figures 2.6, 2.7, 2.8, 2.9, 2.10, 2.11 and 2.12.

For charges above one we find that solutions are generally of two forms. We find solutions which have the maximal D_{NB} symmetry of the axial ansatz, which are comprised of the partons located on the vertices of a regular NB-gon. For the range of N considered in this study we find that for $B > 2$ these maximally symmetric forms do not form a global energy minimum but instead are a local energy minimum. For charge $B \geq 5$ these maximally symmetric solutions could not be found using our gradient flow algorithm and so appear to no longer be stable local energy minima. In the case when we have $B = 2$ and $N = 3$ we find that as well as this maximally symmetric D_6 form there is also a solution with D_2 symmetry formed from two charge one solutions with a relative π rotation and joined along their edges in the polyiamond picture. We can see from Table 2.1 that these two

B	Form	E	E/B	G	Figure
1		34.79	34.79	D_3	2.5(a)
2		66.07	33.04	D_6	2.6(a)
2		66.12	33.06	D_2	2.6(b)
3		101.04	33.68	D_9	2.6(c)
3		98.47	32.82	D_1	2.6(d)
3		100.94	33.65	D_3	2.12(a)
4		138.98	34.75	D_{12}	2.6(e)
4		130.65	32.66	C_2	2.6(f)
4		130.66	32.67	D_1	2.6(g)
4		131.80	32.95	D_3	2.6(h)
4		132.07	33.02	D_4	2.12(b)

Table 2.1: The energy for soliton solutions and their symmetry group G for $B \leq 4$ and $N = 3$.

configurations have comparable energy and so to within numerical accuracy we can not tell which configuration is expected to have lower energy.

For $N > 3$ we found no lower symmetry solutions via our gradient flow algorithm, such as two unit baby Skyrmions in a bound state. Instead initial conditions formed of two unit charges relaxed to the maximally symmetric solution. So this shows that if such a solution were to exist it is most likely an unstable saddle point of the energy. Since the charge two D_{2N} solution found at charge two for $N > 3$ is the only solution found, it is the global energy minimum at this charge.

For topological charge greater than two we find that the favourable configuration appears to be of the form of polyforms. We see that each unit charge solution is a regular N-gon with the N partons located at the vertices. Knowing that these unit charge solutions are maximally attractive with a relative spatial rotation of π, we can construct higher charge multi-soliton initial fields from these unit blocks, rotating them to be in the attractive channel. We can see for each value of N considered here that multi-soliton solutions are connected along edges and so can be seen as configurations of polyforms. This gives us a good ansatz for the possible forms of

B	Form	E	E/B	G	Figure
1		34.58	34.58	D_4	2.5(b)
2		65.58	32.79	D_8	2.7(a)
3		100.28	33.43	D_{12}	2.7(b)
3		97.97	32.66	D_2	2.7(c)
3		98.32	32.77	D_1	2.7(d)
3		98.71	32.90	D_3	2.12(c)
4		137.97	34.49	D_{16}	2.7(e)
4		129.94	32.49	D_2	2.7(f)
4		130.28	32.57	C_1	2.7(g)
4		131.61	32.90	D_1	2.7(h)
4		131.13	32.78	D_4	2.7(i)
4		130.61	32.65	C_2	2.7(j)
4		131.81	32.95	D_4	2.12(d)
4		135.94	33.98	D_4	2.12(e)

Table 2.2: The energy for soliton solutions and their symmetry group G for $B \leq 4$ and $N = 4$.

B	Form	E	E/B	G	Figure
1		34.41	34.41	D_5	2.8(a)
2		65.19	32.59	D_{10}	2.8(b)
3		99.23	33.23	D_{15}	2.8(c)
3		97.68	32.56	C_1	2.8(d)
3		98.14	32.71	C_1	2.8(e)
4		137.20	34.30	D_{20}	2.9(a)
4		129.62	32.40	D_2	2.9(b)
4		129.61	32.40	C_1	2.9(c)
4		130.69	32.67	C_1	2.9(d)
4		130.06	32.52	C_1	2.9(e)
4		131.11	32.78	C_1	2.9(f)
4		131.50	32.87	C_1	2.9(g)
4		129.65	32.41	D_2	2.9(h)

Table 2.3: The energy for soliton solutions and their symmetry group G for $B \leq 4$ and $N = 5$.

B	Form	E	E/B	G	Figure
1		34.26	34.26	D_6	2.10(a)
2		64.88	32.44	D_{12}	2.10(b)
3		99.23	33.08	D_{18}	2.10(c)
3		97.32	32.44	D_2	2.10(d)
3		97.47	32.49	D_1	2.10(e)
3		97.98	32.66	D_3	2.10(f)
4		136.60	34.15	D_{24}	2.11(a)
4		129.11	32.28	D_2	2.11(b)
4		129.26	32.32	C_1	2.11(c)
4		129.41	32.35	D_1	2.11(d)
4		129.41	32.35	D_2	2.11(e)
4		130.58	32.64	D_3	2.11(f)
4		130.79	32.70	D_2	2.11(g)
4		130.85	32.71	D_1	2.11(h)
4		129.09	32.27	D_2	2.11(i)

Table 2.4: The energy for soliton solutions and their symmetry group G for $B \leq 4$ and $N = 6$.

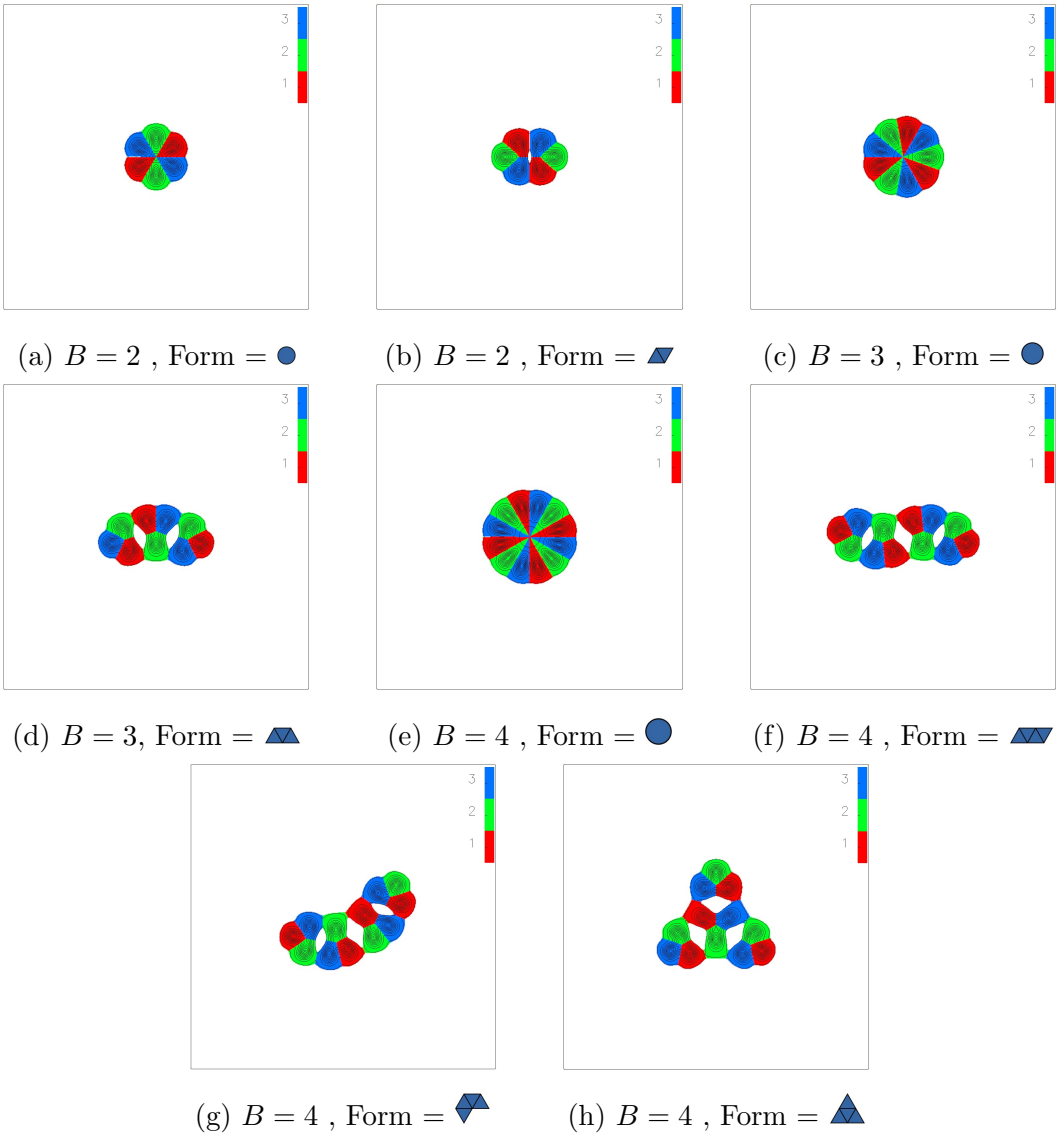

(a) $B = 2$, Form = (b) $B = 2$, Form = (c) $B = 3$, Form =

(d) $B = 3$, Form = (e) $B = 4$, Form = (f) $B = 4$, Form =

(g) $B = 4$, Form = (h) $B = 4$, Form =

Figure 2.6: Energy density plots of the multi-soliton solutions for $N = 3$ and $B \leq 4$ (colour is based on the segment in which the point lies in the target space).

solutions and indeed, as can be seen, this is the form of solutions.

As an example consider the case where $B = 3$ and $N = 4$. We have a solution with the maximal symmetry D_{12}, which has energy per charge $E/B = 33.43$ which is of higher energy than other local energy minimum found. We also have found solutions which take the form of polyominoes. In this case we have two possible polyominoes with the unit charges either in a line with the form or in the form of an 'L' as  . We see that both of these occur in Figures 2.7(c) and 2.7(d) with energies $E/B = 32.66$ and 32.77 respectively. The line solution has a lower energy, and is the global energy minima found for this charge. In fact this is found to be the case for all N with $B \geq 3$, which is expected since it is a known phenomenon also seen in the the unbroken model [27]. This meant that some polyform solutions close to the linear structure were difficult to find, with the initial conditions of these forms relaxing to the lower energy linear solution instead. Due to this we were unable to find solutions of the forms  and  for $N = 5$, nor the form  for $N = 6$. We would however expect local energy minima of this form, but with a very small basin of attraction.

Further to this general structure of solutions there are also some caveats. The first is a form of solutions not captured by the polyform picture, which we shall refer to as hole solutions. These can be seen in Figure 2.12. For $B \geq 3$ we find solutions formed of B unit solitons located so that an edge of each forms the edge of a B-gon with each unit soliton rotated so the colour structure alternates around this B-gon hole. Examples of this can be seen in Figures 2.12(a), 2.12(b), 2.12(c), 2.12(d), 2.12(f), 2.12(h) and 2.12(j). In the special case where $2B \bmod N = 0$ we can also have a solution to the static field equations where the colours are arranged sequentially around the B-gon. Solutions of this form can be seen in Figures 2.12(e), 2.12(g), 2.12(i), 2.12(k) and 2.12(l). For higher N there is also the possibility that more than two partons per unit component can deform to sit on the edge of the B-gon, as we can see occurs in the solution shown in Figure 2.12(l). We note however that these solutions have much higher energy than those presented earlier with polyform structure.

Another caveat which becomes evident from our solutions is that with increasing

N solutions become more deformed from the polyform picture. For example comparing the $N = 4$, $B = 3$ solution of the form  with the plot of the energy density in Figure 2.7(d) we see that the angle it forms is not a right-angle but instead is obtuse. We can understand this behaviour from the form of the energy functional. Due to the derivative terms the energy is obviously lower for fields with smoothly changing values on the two-sphere. Thus there will be an energy cost for points which take values in different segments that are located near each other in physical space. However in the examples where this deformation from the polyform structure exists we see that we would require partons representing non-neighbouring segments of the target sphere to be next to one another. In the solution of the form  we see we require green and yellow partons to be close together in physical space, however these relate to antipodal segments of the target sphere. Thus they are repulsive and cause the solution to deform from the simplified polyform picture. An identical interpretation can be seen to follow for the $N = 3$ $B = 4$ solution of the form  , seen in Figure 2.7(g). This repulsive force is most evident in the cases where we take $N \geq 5$, such as the charge three solutions in $N = 5$ and $N = 6$ with form  and  respectively. These can be seen plotted in Figures 2.8(e) and 2.10(f). Again the deformation from the polyform structure is due to the polyform requiring non-sequential partons to be located near each other. This reasoning also aids to explain why we find that linear solutions form the global energy minima as we increase B rather than a tessellation since fewer non-sequential partons are required to be located close together. Thus solutions appear to deform from the exact polyform structure one might expect, however solutions do appear to be constructed of polyforms which have been deformed. This polyform structure is of great use when deciding on the possible configurations at each charge.

The final caveat which we shall discuss occurs for $N = 5$ and $N = 6$ at charge four. We find a solution which is of a similar form to two warped maximally symmetric charge two solutions joined together in a line. We shall denote such solutions to be of the form  . These solutions for the five and six colour theories can be seen in Figures 2.9(h) and 2.11(i) respectively. These solutions seem to be of a similar energy to the linear polyform made from unit solutions. So we again see that

linear solutions are energetically preferred, even when the linear structures are not necessarily composed of unit charge baby Skyrmions.

2.3 Dynamics in the broken baby Skyrme model

We now turn our attention to the dynamics of broken baby Skyrmions and compare how the introduction of the symmetry breaking potential influences the dynamics of the system when compared to a theory with the standard potential, maintaining the $O(2)$ symmetry of the model. Numerical simulations were undertaken using a fourth-order accurate Runge-Kutta method on a square grid of 751×751 grid points with $\Delta x = 0.04$ and $\Delta t = 0.01$. At the boundary we keep the the field fixed as the vacuum value $\boldsymbol{\phi}_\infty$. We also include a damping term around the boundary to remove kinetic energy which hits the boundary to limit any kinetic energy reflecting back off the boundary and impacting on the numerical simulations. Especially when introducing such damping terms it is important to ascertain where on the grid boundary effects start to impact upon the reliability of the numerical simulations. To do this we can send a soliton towards the boundary with slow velocity and determine at what stage the boundary damping term affects this velocity. In our numerical set-up the boundary damping term was seen to have an effect when the soliton was located at a distance approximately 5 from the boundary. We therefore claim that solutions have escaped to infinity in our numerical solutions when they reach this proximity to the boundary.

As we have mentioned previously, two baby Skyrmions are aligned in the attractive channel if there is a relative rotation of π between them. However, since we have broken the axial symmetry by our choice of potential term it follows that there may be further parameters controlling the rotation of one of the solutions which need to be considered at short-range. For example, whether the solitons are collided point-to-point or edge-to-edge. From our work in the previous section we have seen by the form of solutions to the static equations of motion that the broken baby Skyrmions are maximally attractive when rotated relatively by π and sharing a common edge. We shall see how this additional short-range behaviour of preferring

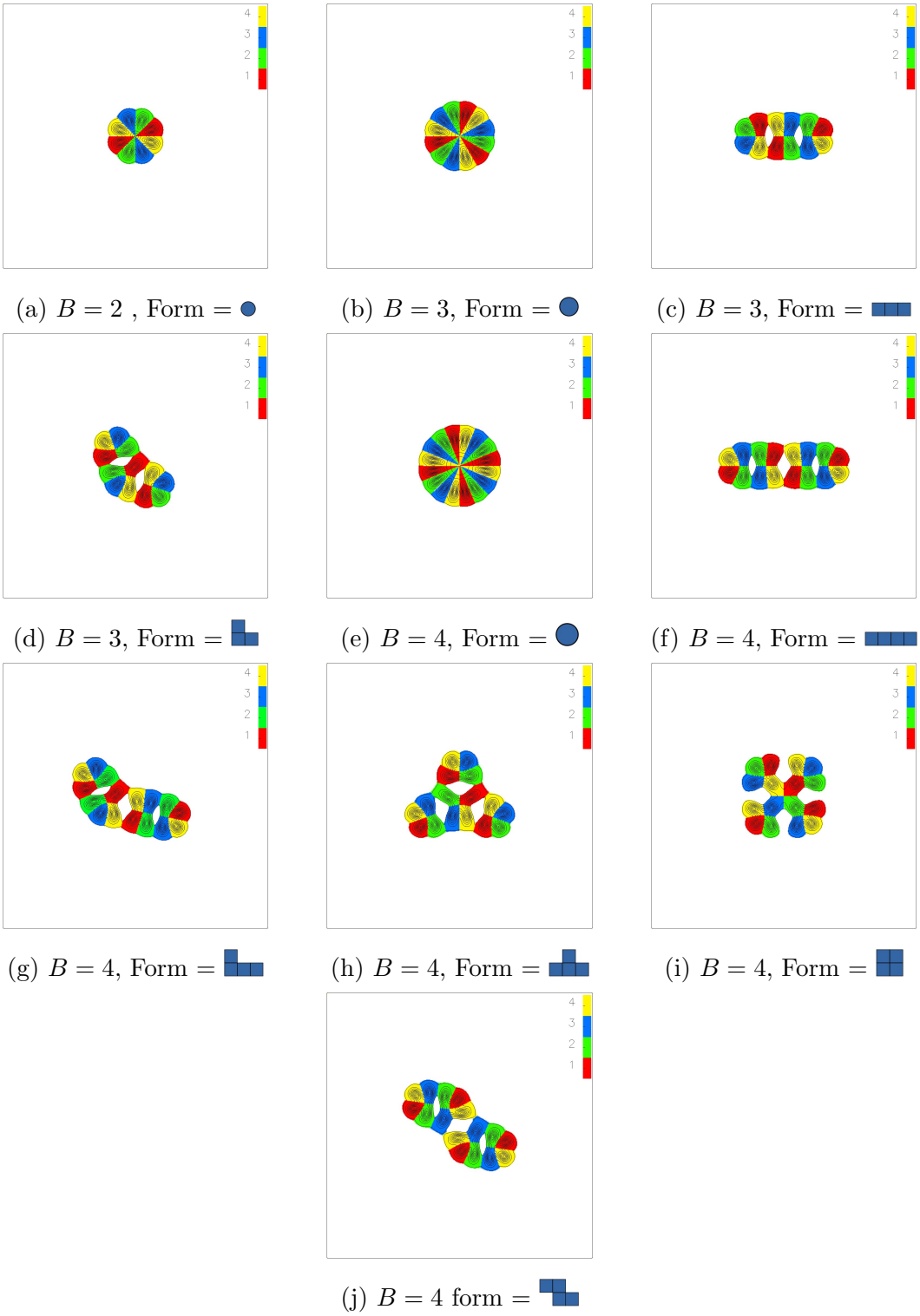

(a) $B = 2$, Form = (b) $B = 3$, Form = (c) $B = 3$, Form =

(d) $B = 3$, Form = (e) $B = 4$, Form = (f) $B = 4$, Form =

(g) $B = 4$, Form = (h) $B = 4$, Form = (i) $B = 4$, Form =

(j) $B = 4$ form =

Figure 2.7: Energy density plots of the multi-soliton solutions for $N = 4$ and $B \leq 4$ (colour is based on the segment in which the point lies in the target space).

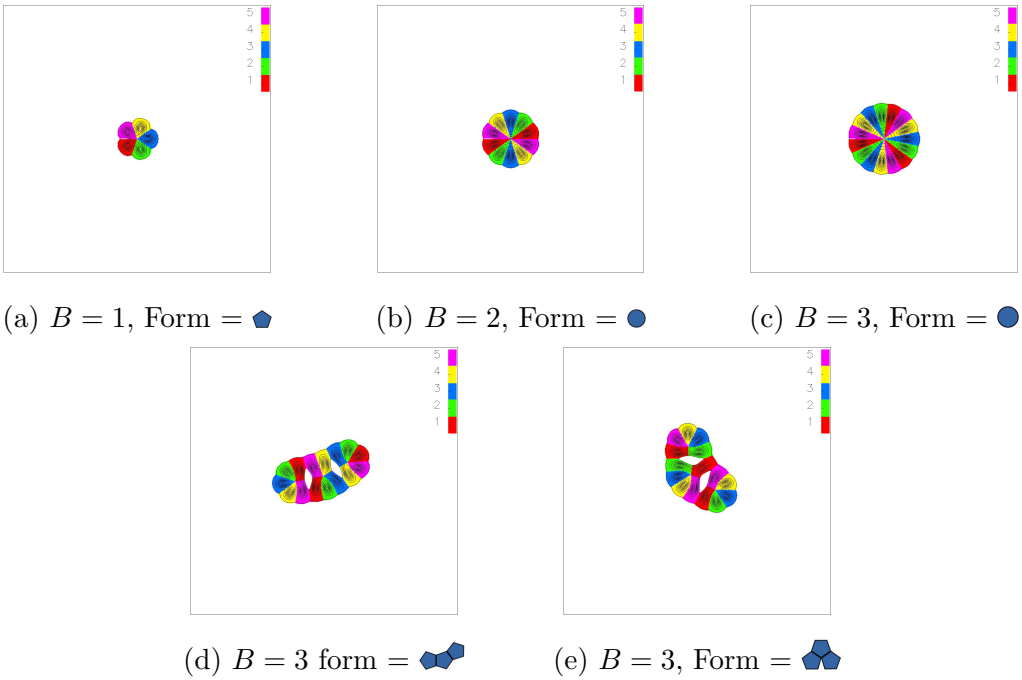

(a) $B = 1$, Form =
(b) $B = 2$, Form =
(c) $B = 3$, Form =
(d) $B = 3$ form =
(e) $B = 3$, Form =

Figure 2.8: Energy density plots of the multi-soliton solutions for $N = 5$ and $B \leq 3$ (colouring is based on the segment in which the point lies in the target space).

to align edge-to-edge effects the scattering of the broken baby Skyrmions.

We first consider the case where two unit charge broken baby Skyrmions collide. We position baby Skyrmions at $(-6.0, 0.0)$ and $(6.0, 0.0)$, each with a velocity directed towards the origin of magnitude v. In this study we considered a range of speeds $0.1 \leq v \leq 0.6$. We start by discussing the results of aligning the solitons so they collide edge-to-edge for the $N = 3$ case. The results can be seen in Figure 2.13 where we have plotted the coloured energy density at time-points of a scattering process. We also plot in Figure 2.13(h) the path that each parton takes during a scattering process. This path is calculated by finding the location of the maximum of the energy density which each parton relates to at each time point. This can then be plotted to give the path which the parton has followed. We find that the solitons undergo right-angled scattering as is common in topological soliton systems and as is seen in the baby Skyrme model with an unbroken potential. With the broken symmetry of solutions and our colouring of the partons it is also evident that on collision the broken baby Skyrmions undergo a rotation after collision. This can also be seen to be the case for $N = 4$ unit broken baby Skyrmions, as seen in

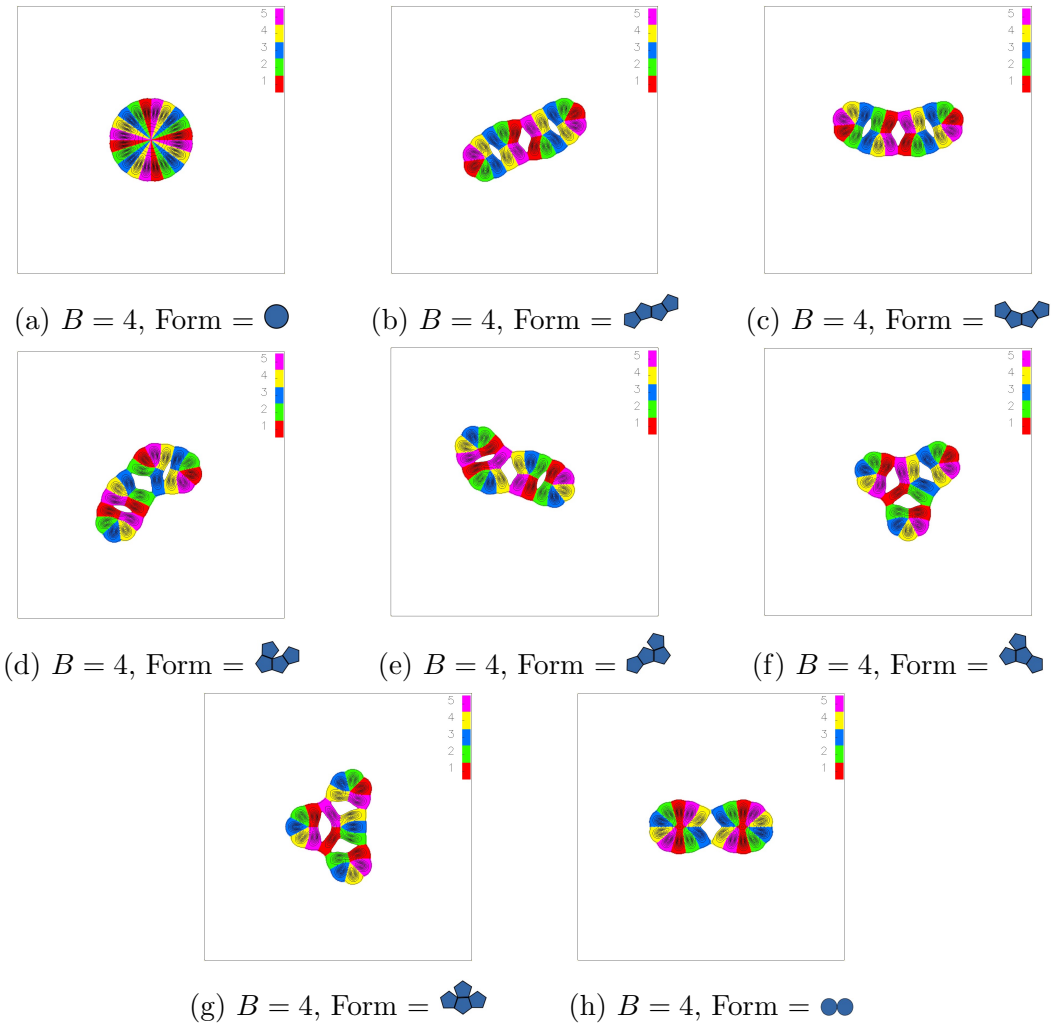

(a) $B = 4$, Form = (b) $B = 4$, Form = (c) $B = 4$, Form =

(d) $B = 4$, Form = (e) $B = 4$, Form = (f) $B = 4$, Form =

(g) $B = 4$, Form = (h) $B = 4$, Form =

Figure 2.9: Energy density plots of the multi-soliton solutions for $N = 5$ and $B = 4$ (colouring is based on the segment in which the point lies in the target space). Note that the solution was not obtained, although we still expect this solution to exist. It was very similar to the caveat in 2.9(h) meaning it was difficult to pick out initial conditions that would relax to the desired solution rather than this lower energy caveat form.

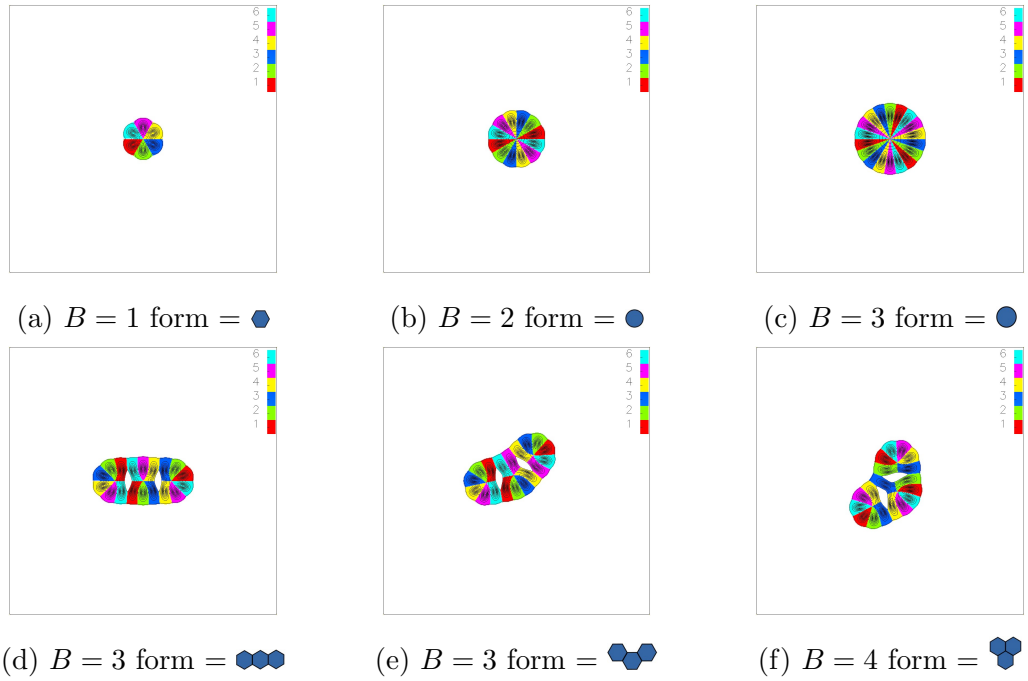

(a) $B = 1$ form = (b) $B = 2$ form = (c) $B = 3$ form =

(d) $B = 3$ form = (e) $B = 3$ form = (f) $B = 4$ form =

Figure 2.10: Energy density plots of the multi-soliton solutions for $N = 6$ and $B \leq 3$ (colouring is based on the segment in which the point lies in the target space).

Figure 2.14. We find that for scatterings in which the unit broken baby Skyrmions are aligned point-to-point that a similar scattering process occurs. We see that for the three-colour system this is just a time reversal of the edge-to-edge scattering due to the rotation of solutions after scattering. We also have undertaken scatterings where the alignment is somewhere between edge-to-edge and point-to-point, but still with relative rotation π between them. An example of such a scattering is shown in Figure 2.15 where we see that as the solitons approach they align themselves so that they are in what we have already suggested would be the maximally attractive channel, that is that as they approach they undergo a rotation so they are aligned edge-to-edge while their relative phase remains unchanged. This induced rotation continues after scattering, although the symmetry of the system is preserved. An important feature of all these scatterings is that they exhibit parton exchange. We see that the partons which make up each ingoing unit charge soliton are swapped between them on scattering so that the outgoing unit solitons are comprised of partons from multiple ingoing solitons. This is a novel phenomenon not before seen in Skyrme-type models.

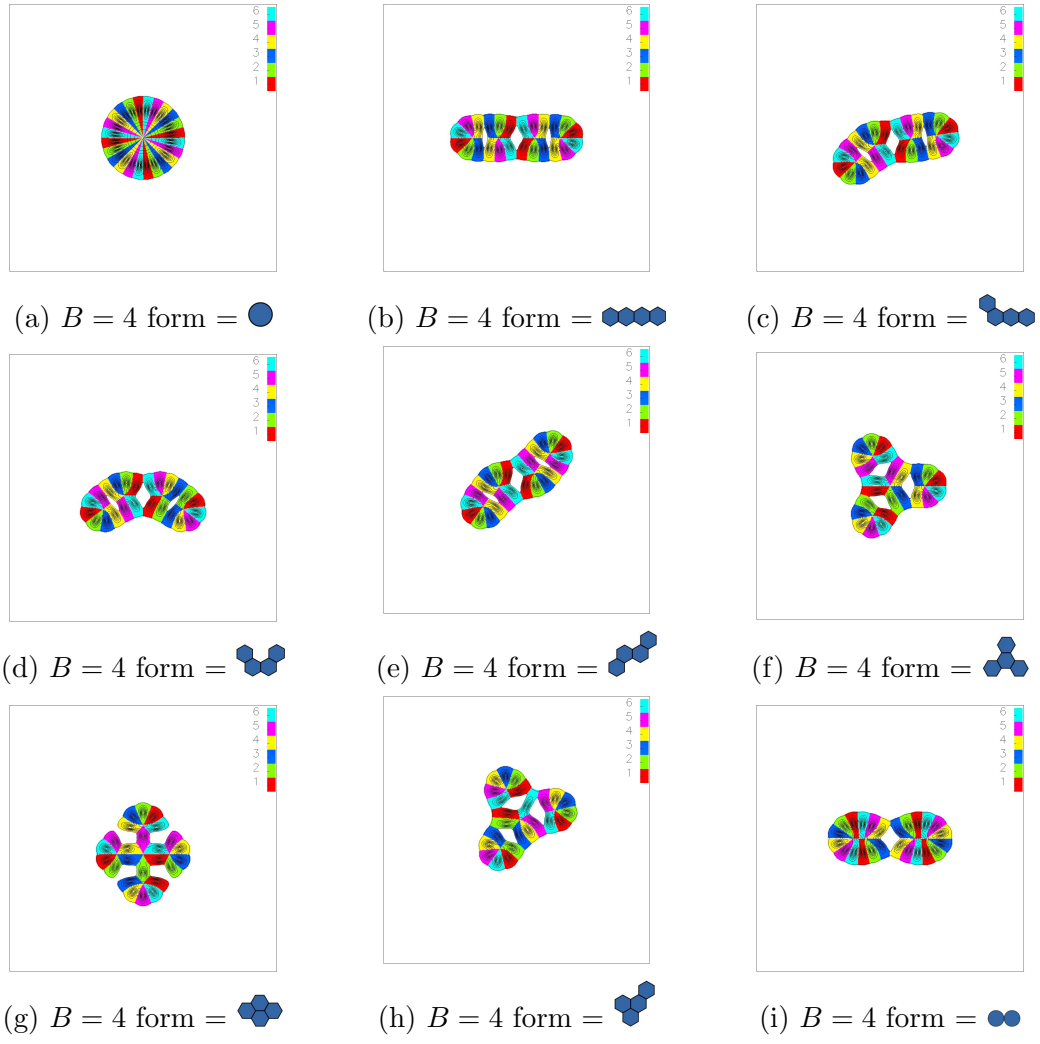

(a) $B = 4$ form = (b) $B = 4$ form = (c) $B = 4$ form =

(d) $B = 4$ form = (e) $B = 4$ form = (f) $B = 4$ form =

(g) $B = 4$ form = (h) $B = 4$ form = (i) $B = 4$ form =

Figure 2.11: Energy density plots of the multi-soliton solutions for $N = 6$ and $B = 4$ (colouring is based on the segment in which the point lies in the target space).

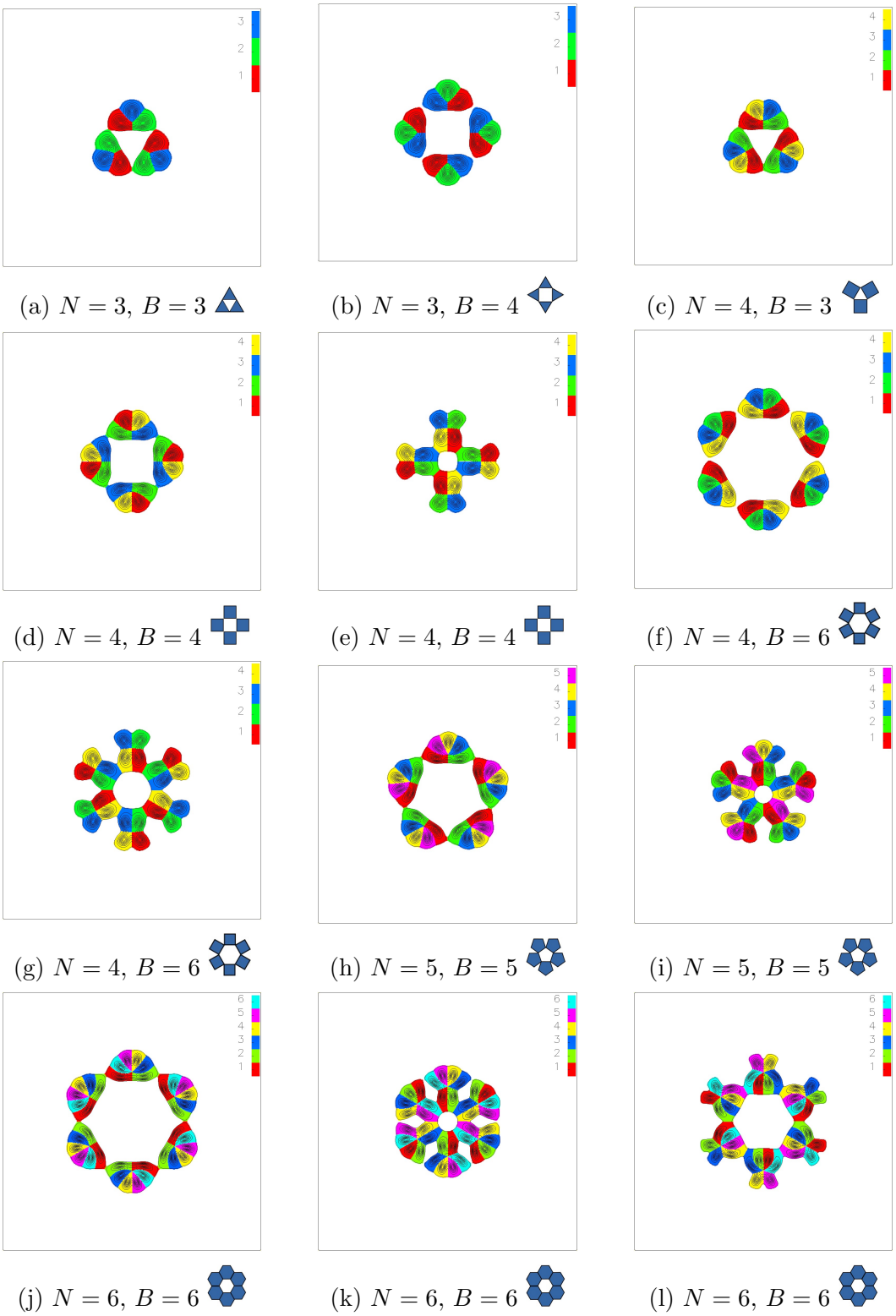

(a) $N = 3$, $B = 3$ (b) $N = 3$, $B = 4$ (c) $N = 4$, $B = 3$

(d) $N = 4$, $B = 4$ (e) $N = 4$, $B = 4$ (f) $N = 4$, $B = 6$

(g) $N = 4$, $B = 6$ (h) $N = 5$, $B = 5$ (i) $N = 5$, $B = 5$

(j) $N = 6$, $B = 6$ (k) $N = 6$, $B = 6$ (l) $N = 6$, $B = 6$

Figure 2.12: Energy density plots detailing the various hole caveats to the predicted polyform structure.

We are also able to view the collision in terms of the individual partons of the theory, with the individual partons scattering in particular ways depending on the colours involved. They follow a certain set of relations which enables us to understand and predict the scattering processes of many scatterings. As we have mentioned in the previous section, the derivative terms in the energy functional penalises any rapid change in the value of the field. Thus partons relating to the same segments of the target two-sphere can get close to one another, while those relating to different colours have a natural separation dependent on the phase difference between them. This leads to an understanding of the scattering behaviour for general N and for a wide range of scatterings at reasonable speeds.

Firstly, if two partons of the same colour scatter off one another these coalesce before scattering at an angle which bisects the incident angles. So in the above cases where we have two partons of the same colour with equal and opposite velocities this is right-angle scattering. The picture for the scattering of partons relating to different colours depends upon the phase difference between them. Parton scattering in which colours that are sequential around the target two-sphere have a relatively small preferred separation and although do not scatter off from each other, instead bond together which can then move apart with other partons that have emerged from scattering. Finally for partons scattering which relate to different non-sequential colours these do not want to be close in physical space, and so feel a repulsive force, and at the current speeds investigated motion stops before they scatter from each other. Instead they are deflected as a result of following the partons to which they are bonded to. Thus the scattering behaviour of broken baby Skyrmions is determined by the scattering behaviour between constituent partons.

We can apply this description to the scattering of two unit charge solitons in the $N = 3$ system scattered edge-to-edge as can be seen in Figure 2.13. We see that initially two sets of sequential colours come together and bond with one another. Each pair then moves apart orthogonally to the direction of motion following from the momentum of the system and the energy penalty for the field changing too rapidly if partons become too close. The green partons continue to move towards each other, scatter at right-angles and then each bond to one of the two-parton

pairs. These two resulting unit broken baby Skyrmions then move apart. A similar analysis can be made relating the scattering of two unit charge $N = 4$ broken baby Skyrmions scattered edge-to-edge. The first pair of parton scatterings from the leading edges are between sequential colours, and so we find a similar case to that above, with them bonding together and them moving apart orthogonally to the direction of motion. A similar process is then repeated with the second pair of scatterings from the trailing edge.

We see in our simulations that in both these cases that the scattering induces oscillatory modes on the outgoing unit solitons, as can be seen in the plots where the position of the partons has been tracked. We can understand this as a balancing of the motion from the scattering collision and a preferred separation between partons of different colours preventing partons of different colours from getting close together. This causes the partons to undergo a damped oscillation after collision. We are able to check that these simple rules for scattering seem to hold for more complicated scatterings, such as can be seen in Figure 2.16. Three unit charge $N = 3$ solitons located at the vertices of an equilateral triangle scatter at the origin each leading with a point. We see that the blue partons scatter first and the emergent partons bisect the angle between incident trajectories. The second set of partons in this case slow as they bond with the now scattered blue partons which pull the remaining partons apart from their original partons to form the outgoing unit broken baby Skyrmions.

For each scattering event there is a critical escape velocity, v_e, for which if $v \geq v_e$ then the resulting solitons escape to infinity after the collision, while for $v < v_e$ we see that the attractive force between the two scattered solitons results in them being accelerated towards each other again and further scattering occurs. We note that this second scattering appears like a time reversal of the first, albeit with a lower velocity due to the kinetic radiation on collision. This also means that due to the rotation on scattering that this second scattering is possibly different to the first, for example in the three-colour theory if it is initially an edge-to-edge scattering then this second will be a point-to-point. Since a large amount of kinetic radiation is released on collision we see that these oscillations are damped and coalesce into a

single soliton – eventually forming solutions to the static equations of motion.

Due to the radiation during scattering we find that the escape velocities are rather high. For the scattering processes looked at for this study a range of $0.3 \leq v_e \leq 0.5$ was found. This escape velocity is also found to be dependent on the number of colours we are considering in the theory and also on the alignment of the baby Skyrmions we are considering. For example, in the three colour system, when two Skyrmions are scattered in the attractive channel point-to-point we find an escape velocity of approximately 0.20, whilst when they are scattered edge-to-edge we find an escape velocity of approximately 0.38. This increase in the velocity needed for the solitons to escape can be understood by the fact that in the edge-to-edge scattering process partons come together and bond, where as for the point-to-point scattering process these do not form bonds so tightly, since the partons of identical colour meet first and strip the neighbouring partons before additional bonds are formed.

2.4 Conclusion

We have seen that introducing a potential given by equation (2.1.1) breaks the global symmetry of the baby Skyrme model to the dihedral group D_N, and have explored the impact this has upon the form of solutions for a range of N. We have also found that the link with polyiamonds for $N = 3$ extends to polyforms for general N, albeit with some additional considerations. An interesting extension to this work on static solutions would be to look at the soliton lattice that corresponds to different choices of N. For $N = 3$ it was found that the soliton lattice with the lowest energy was formed from a cell containing a unit charge broken baby Skyrmion, tessellating the space as one would expect for an equilateral triangle. For $N = 4$ and $N = 6$ one would expect the obvious tessellations relating to the square and the hexagon, however the deformation of the polyform structure found in this study may impact upon the formation of a lattice. Some clues to how this lattice might appear can be gained from solutions of the form  and  in Figures 2.7(i) and 2.11(g) respectively. For the cases where N is such that the N-gon does not tessellate the picture is more complicated and it would be interesting to see what

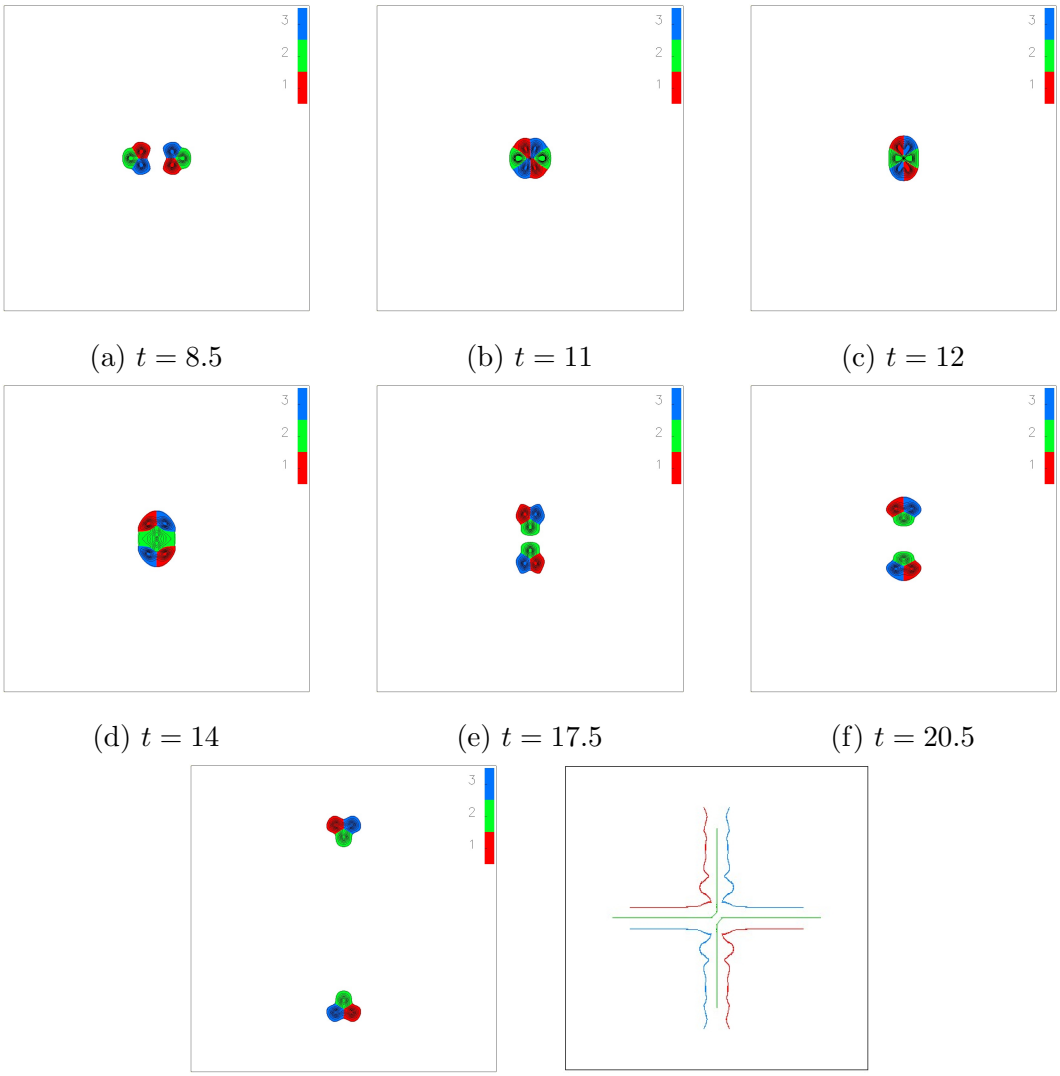

(a) $t = 8.5$ (b) $t = 11$ (c) $t = 12$

(d) $t = 14$ (e) $t = 17.5$ (f) $t = 20.5$

(g) $t = 50$ (h) Parton tracks

Figure 2.13: Energy density plots at various times during the scattering of two $N = 3$ single solitons each with speed 0.4 and with relative spatial rotation of π

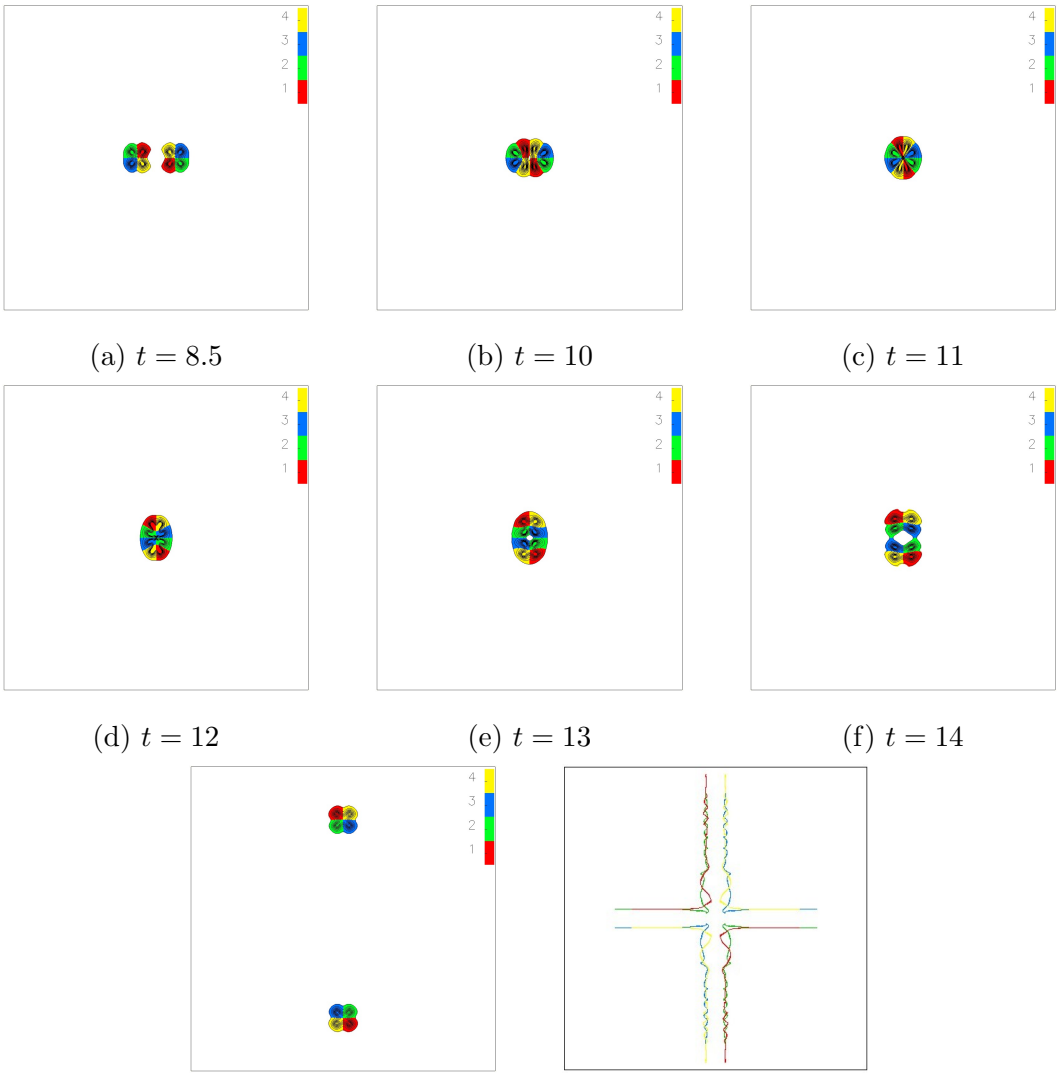

(a) $t = 8.5$ (b) $t = 10$ (c) $t = 11$

(d) $t = 12$ (e) $t = 13$ (f) $t = 14$

(g) $t = 30$ (h) Parton tracks

Figure 2.14: Energy density plots at various times during the scattering of two $N = 4$ single solitons each with speed 0.4 and with relative spatial rotation of π

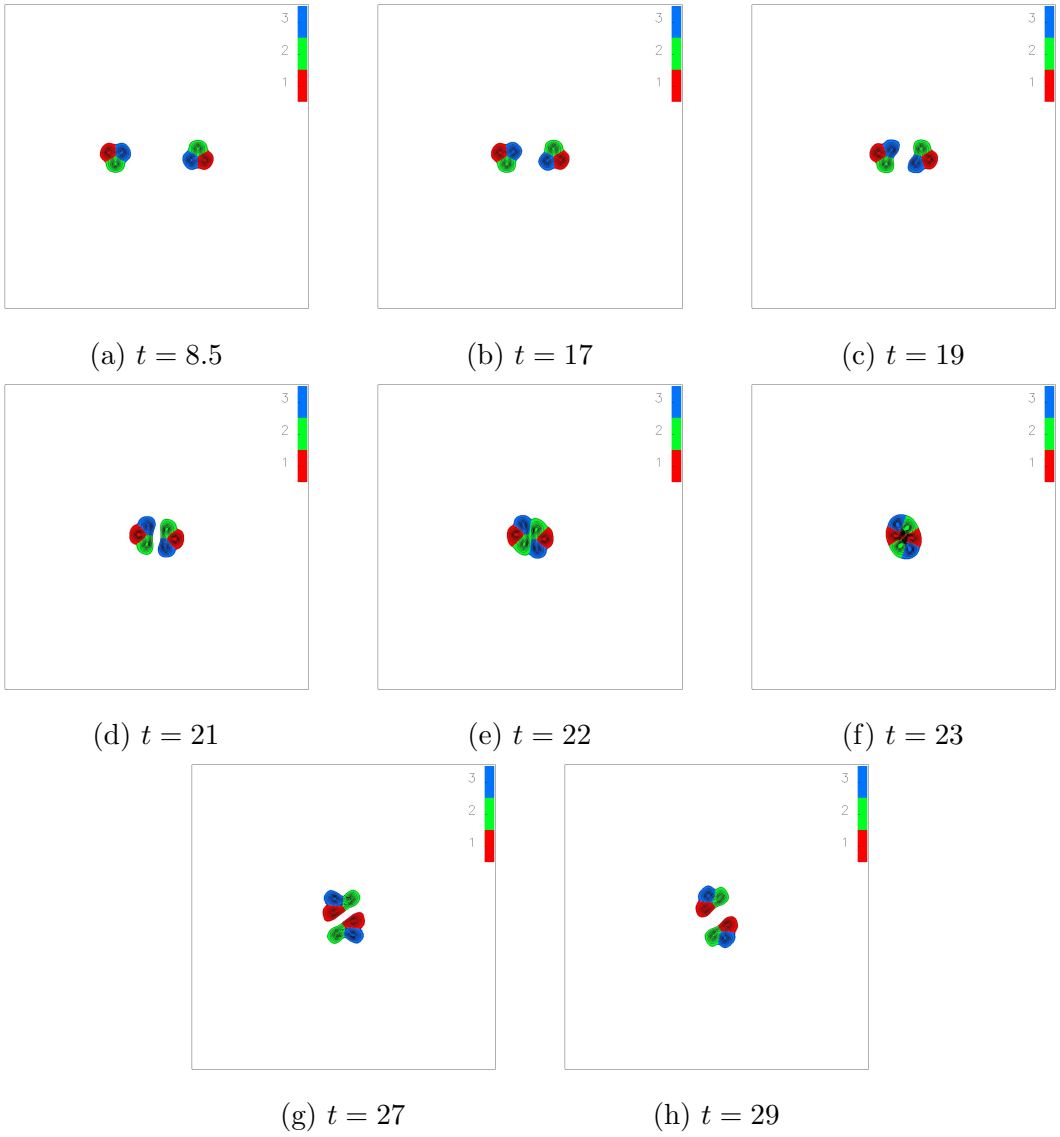

(a) $t = 8.5$ (b) $t = 17$ (c) $t = 19$

(d) $t = 21$ (e) $t = 22$ (f) $t = 23$

(g) $t = 27$ (h) $t = 29$

Figure 2.15: Energy density plots at various times during the scattering of two $N = 3$ single solitons each with speed 0.4 and with relative spatial rotation of π. The solitons' edges however, are not aligned.

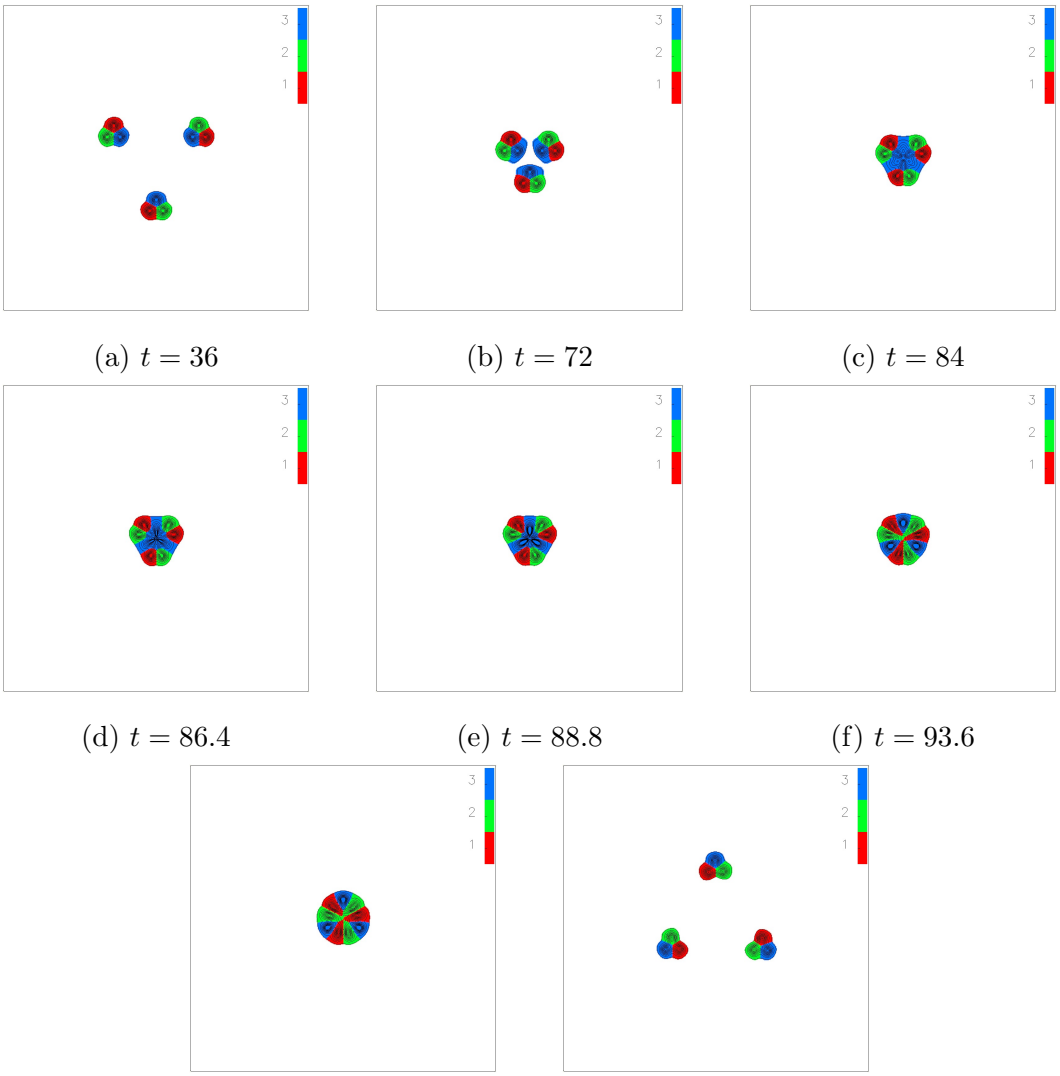

(a) $t = 36$ (b) $t = 72$ (c) $t = 84$

(d) $t = 86.4$ (e) $t = 88.8$ (f) $t = 93.6$

(g) $t = 96$ (h) $t = 168$

Figure 2.16: Energy density plots at various times during the scattering of three $N = 3$ single solitons each with speed 0.3 and with relative spatial rotation of $\frac{2\pi}{3}$.

happens here, whether basic tessellations occur through deformation of the solitons, or whether more complicated tessellations are evident.

For higher charges the number of possible polyform solutions grows exponentially and so checking all possible solutions in a full numerical scheme becomes a harder task. Thus a point particle approximation of solutions would be useful to predict the form of solutions to the problem as the charge increases. This would also mean positions of initial conditions could be made more accurate from such simulations. This could be easily implemented by approximating the field by point parton interactions modelled with Lennard-Jones type potentials between them [42]. It would be interesting to see if such potential could capture the behaviours seen in this study.

We have also seen that the dynamics of the broken baby Skyrme model are classically dependent upon the colour structure. We see that as well as the relative phase between the two solitons, at short range the individual orientations of each soliton become important. Solutions are in the maximally attractive channel when they have a relative phase of π and have their edges aligned. We have also proposed a way of understanding the scattering events in terms of the behaviour of interactions between individual partons.

It would be an obvious extension to this work to consider a similar symmetry breaking term in the full (3+1)-dimensional Skyrme model, and see whether we can consider scatterings in this higher dimensional model in terms of the resulting three-dimensional partons of such a theory. However, if a symmetry breaking term is included in the full model then the symmetry which is broken corresponds to the isospin symmetry of baryons. It is not clear what the physical consequences of the breaking of this isospin symmetry would be and would require careful thought. The (3+1)-dimensional Skyrme model obviously does not require a potential term to be able to evade Derrick's theorem, as we saw in the introduction to this thesis, and so a potential term may not play such a crucial role as with the baby Skyrme model so such extreme differences might not be found by breaking the symmetry. When studies have been undertaken in which a potential term has been included to study massive baryons it was found that solutions for high baryon number were quali-

tatively different to the corresponding massless solutions [16], so some qualitative differences might still be evident.

Chapter 3

The dynamics of domain wall Skyrmions

We have seen that baby Skyrmions are of interest as a lower dimensional analogue of the three-dimensional Skyrme model of QCD. As was also mentioned in the previous chapters the $(2+1)$-dimensional analogue, baby Skyrmions, are of interest in their own right since they have links to condensed matter systems. More concretely, the models used for these condensed matter systems are non-relativistic theories which have a resemblance to the baby Skyrme model. The Skyrme term does not appear in these models and is instead replaced by terms with a similar stabilising effect which may appear in non-relativistic theories. Structures similar to baby Skyrmions are found in theories such as fractional quantum Hall systems [21] and chiral magnets [22]. In these theories the Skyrme term is replaced with a non-local Coulomb term and a Dzyloshinskii-Moriya interaction term respectively.

For example, quantum Hall systems are described by a classical field theory model with static energy given by

$$E_{QH} = \nu^2 \int \partial_i \boldsymbol{\phi} \cdot \partial_i \boldsymbol{\phi} \, d^2\mathbf{x} + \lambda^2 \iint \frac{\mathcal{B}(\mathbf{x})\mathcal{B}(\mathbf{x}')}{|\mathbf{x}-\mathbf{x}'|} \, d^2\mathbf{x} \, d^2\mathbf{x}' + m^2 \int (1-\phi_3) \, d^2\mathbf{x} \quad (3.0.1)$$

where ν, λ and m are constants of the theory, $\boldsymbol{\phi}$ is the usual three-component unit vector and $\mathcal{B}(\mathbf{x})$ is the topological charge density at position $\mathbf{x}$, that is $\mathcal{B} = -\frac{1}{4\pi}\boldsymbol{\phi} \cdot (\partial_1 \boldsymbol{\phi} \times \partial_2 \boldsymbol{\phi})$. The first term of the static energy is obviously that of the pure sigma model, which describes the exchange interaction between Heisenberg spins.

While the final term is the standard Zeeman energy for spins in a magnetic field, which again is familiar from the baby Skyrme model as the standard potential term. The middle term here is the non-local Coulomb term, which plays the role of the Skyrme term in this theory. An application of Derrick's theorem shows that under a spatial rescaling this term scales inversely to the scaling of the Zeeman energy, and so stable solutions with non-trivial solutions may exist. One point to note however is that the Coulomb term scales linearly rather than quadratically such as the Skyrme term would under a spatial rescaling.

In two-dimensional chiral magnets we find such a system is described by [22]

$$E_\chi = \int \frac{J}{2}(\partial_i \boldsymbol{\phi} \cdot \partial_i \boldsymbol{\phi}) + \alpha \boldsymbol{\phi} \cdot (\tilde{\nabla} \times \boldsymbol{\phi}) - \mathbf{H} \cdot \boldsymbol{\phi}\, d^2\mathbf{x}, \tag{3.0.2}$$

where $\boldsymbol{\phi}$ is the unit three-component magnetisation vector, J is the ferromagnetic exchange coupling, α is the Dzyloshinskii-Moriya interaction constant and $\mathbf{H}$ is an external applied magnetic field to give the Zeeman energy. We also define $\tilde{\nabla} = (\partial_x, \partial_y, 0)$. This corresponds to the three dimensional model by making the field independent of the z-direction. The second term here is the Dzyloshinskii-Moriya interaction. Solutions to this theory as well as those relating to the quantum Hall systems have been seen to have similar features to baby Skyrmions.

From the above we see that such higher order terms like the Skyrme term are hard to motivate physically in such condensed matter models. Recently it has been found [43, 44, 45, 46] that static Skyrmions can exist in relativistic theories without a Skyrme term so long as the Skyrmion is located on a domain wall. Even without the inclusion of the Skyrme term it is found that the Skyrmion still has a finite fixed size deriving from the presence of the domain wall. The possibility of stable Skyrmions without the higher order derivative terms would mean that there would exist a range of physically relevant situations in which Skyrmions could arise in theories. If dynamics plays no role, then whether the system is relativistic or not does not matter, and so static solutions of such models may find applications in condensed matter systems. Domain walls also exist in numerous relativistic theories from a diverse range of theories. For example they are evident in cosmology where they occur in braneworld models, and in high energy physics within supersymmetric theories where domain walls play a significant role in breaking the supersymmetry

to leave fractions of supersymmetry. Thus the findings of this chapter might find applications in these fields which are quite different from our initial motivations.

To date studies of stable Skyrmions in relativistic theories without a Skyrme term have been restricted to numerical studies of a single Skyrmion on a domain wall in (2+1)-dimensions [46]. The form of fields within this new theory are rather different to that usually taken when a Skyrme term is included, so it is of interest to examine what new phenomena might occur in this model. In this work we look at the first numerical investigation of dynamics and multi-Skyrmions in a (2+1)-dimensional theory of Skyrmions located on a domain wall without a Skyrme term. Although the current work here is for a theory in (2+1)-dimensions, it is expected that the results presented here would generalise to similar theories in higher dimensions.

3.1 The model and its static Skyrmion

The theory we study in this chapter is a (2+1)-dimensional sigma model, with a particular choice of potential which is chosen to be the simplest example of a theory which exhibits properties required to support a Skyrmion on a domain wall, which we shall make more concrete later. However, the features we require are not very restrictive and our findings should hold for a wide range of different potentials and models.

The theory we concern ourselves with here is given by Lagrangian density

$$\mathcal{L} = \frac{1}{2}\partial_\mu \boldsymbol{\phi} \cdot \partial^\mu \boldsymbol{\phi} - \frac{m^2}{2}(\phi_1^2 + \phi_2^2) + \frac{gm^2}{2}(\phi_1^2 + \phi_2^2)^2\phi_2, \tag{3.1.3}$$

where $\boldsymbol{\phi} = (\phi_1, \phi_2, \phi_3)$ is a unit vector and x_μ are spacetime coordinates with $x_0 = t$, $x_1 = x$ and $x_2 = y$. The Lagrangian density also depends on m and g which are parameters of the theory satisfying $m > 0$ and $0 < g < 1$. The energy which (3.1.3) corresponds to is given by

$$E = \int \left\{ \frac{1}{2}\partial_t \boldsymbol{\phi} \cdot \partial_t \boldsymbol{\phi} + \frac{1}{2}\partial_i \boldsymbol{\phi} \cdot \partial_i \boldsymbol{\phi} + \frac{m^2}{2}(\phi_1^2 + \phi_2^2) - \frac{gm^2}{2}(\phi_1^2 + \phi_2^2)^2\phi_2 \right\} d^2x \tag{3.1.4}$$

where the Latin indices run over spatial components. The constraints on the parameters $m > 0$ and $g \in (0, 1)$ ensure that the energy density is non-negative. Our choice of potential breaks the symmetry to a discrete symmetry given by $\phi_1 \mapsto -\phi_1$ and

$\phi_3 \mapsto -\phi_3$. It has vacua when $\boldsymbol{\phi} = (0, 0, \pm 1)$ and this partially motivates our choice of potential. These antipodal vacua hold for all choices of $m > 0$ and $g \in (0, 1)$. The choice to fix the vacua for the parameters is not essential however, and indeed other potentials without this property have previously been studied [43, 44, 45, 46] where only linear and quadratic terms appear in the potential. Our choice to fix these simplifies the winding structure of the Skyrmion and is chosen purely for convenience. The leading behaviour of the potential is that of a uniaxial magnetocrsytalline anistropy term with one easy axis which has applications for a range of magnetic materials.

For a field to have finite energy we see that we require the field to tend to the same vacuum field at spatial infinity. For example fix $\boldsymbol{\phi} \to (0, 0, 1)$ as $x^2 + y^2 \to \infty$. Applying Derrick's theorem we know that without a term which is of higher order in derivatives we are unable to have finite energy static solutions other than the trivial solution where the field takes the vacuum at all points in the plane. As we have seen in the previous chapter, this is usually done by the addition of a Skyrme term

$$\mathcal{L}_{Skyrme} = -\frac{\kappa^2}{4}(\partial_\mu \boldsymbol{\phi} \times \partial_\nu \boldsymbol{\phi}) \cdot (\partial^\mu \boldsymbol{\phi} \times \partial^\nu \boldsymbol{\phi}) \tag{3.1.5}$$

to the Lagrange density (3.1.3). Such systems with the Skyrme term included have been studied previously for $g = 0$ [25]. The way that the winding is realised in this model for a charge one Skyrmion can be seen in Figure 3.1(a) for the case $g = 0$. The colouring of the field is determined by the value of ϕ_3 and the two-component vector (ϕ_1, ϕ_2) is shown. We see that ϕ_3 changes radially from its value at spatial infinity of 1 to take the value -1 at the centre of the soliton (which we have taken to be at the origin). Looking at the circle where $x^2 + y^2 = a^2$, for a finite and positive we see every point on the restriction of the target sphere with ϕ_3 fixed is given. We see this as the vector taking all possible directions. Thus we see that the field takes all possible values on the two-sphere. If we were to consider our potential with the Skyrme term included for the case of non-zero g we find a picture which is qualitatively the same, however we lose the axial symmetry related to the $O(2)$ symmetry being broken. We will see that the winding structure which our Skyrmions without a Skyrme term but located on a domain wall take are very different.

Before we discuss how to construct Skyrmions on the domain wall, we first discuss

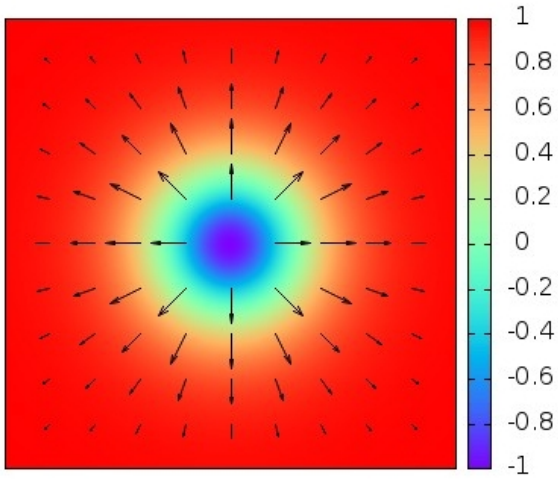

(a)

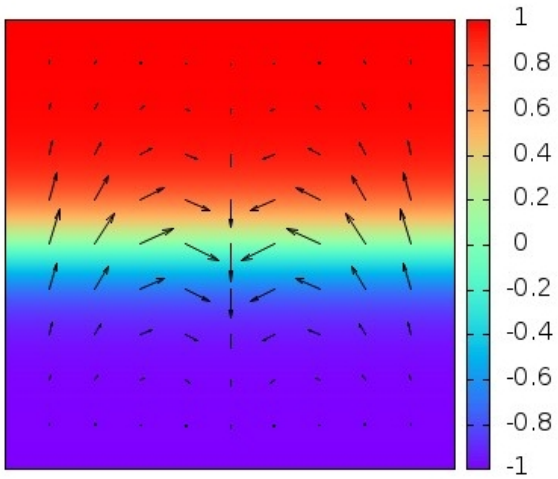

(b)

Figure 3.1: The winding structure in the (x, y) plane of a standard Skyrmion (a) and a Skyrmion on a domain wall (b). The colour represents the value of ϕ_3 and the arrow indicates the length and direction of the two-component vector (ϕ_1, ϕ_2).

the domain walls of the theory. One can calculate that the field equations derived from Lagrangian density (3.1.3) have solutions which are static domain walls, where the field is independent of x and interpolates between the two vacua of the theory. Since $\boldsymbol{\phi}$ is a three component vector we can choose for this interpolation to occur purely in the second and third components of the field. Explicitly, consider a solution of the form

$$\boldsymbol{\phi} = (0, \sin\theta, \cos\theta), \tag{3.1.6}$$

for $\theta(y)$ satisfying the boundary conditions $\theta \to \pi$ as $y \to -\infty$ and $\theta \to 0$ as $y \to \infty$ so that the field interpolates correctly for the domain wall, that is $\boldsymbol{\phi} \to (0, 0, \pm 1)$ as $y \to \pm\infty$. We also chose to fix the location of the domain wall at the x-axis by requiring $\theta(0) = \pi/2$.

Since the wall is independent of the x direction, it obviously has infinite energy, however it does have finite energy per unit length, called the tension of the domain wall. This is given by

$$\mu = \int \left\{ \frac{1}{2}\theta'^2 + \frac{m^2}{2}(\sin^2\theta - g\sin^5\theta) \right\} dy. \tag{3.1.7}$$

Variation of this tension gives us the static field equation satisfied by the domain wall profile function $\theta(y)$,

$$\theta'' - m^2\cos\theta\sin\theta(1 - \frac{5}{2}g\sin^3\theta) = 0. \tag{3.1.8}$$

We see that for $g = 0$ we have the explicit solution $\phi_3 = \cos\theta = \tanh(my)$ with corresponding tension $\mu = 2m$. For $g > 0$ we find that there are no elementary explicit solutions, however it is a simple task to obtain these domain wall solutions numerically. These solutions and their resulting energy density plots are shown in Figure 3.2 for a range of g. We see that although the value of g seems to have little impact upon the field itself, we can see that the appearance of the energy density is quite sensitive to the specific value of g.

Given such a domain wall we see that there is no dependence on the (ϕ_1, ϕ_2) components perpendicular to the domain wall, however in the above we have chosen for them to lie on the $\phi_1 = 0$ line. We can then impose a winding in these components along the domain wall, which will leave the domain wall in the y direction and which

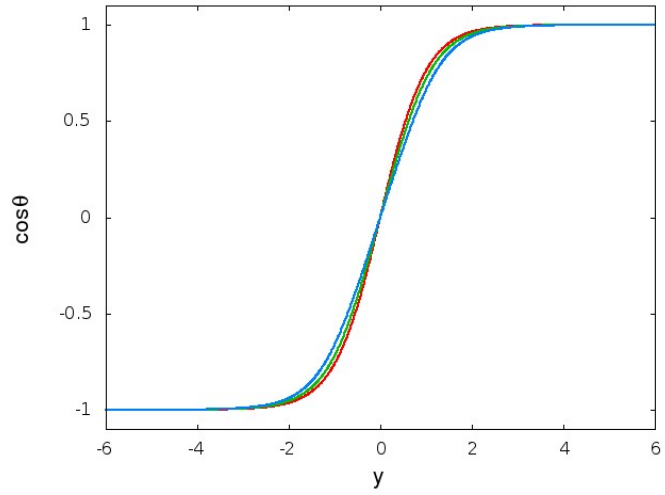

(a)

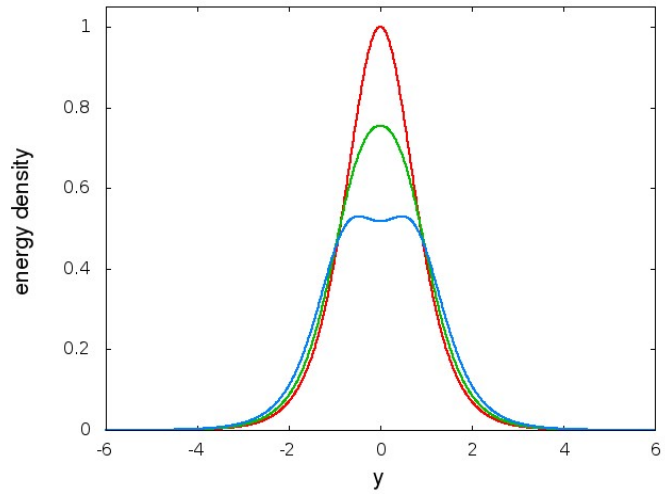

(b)

Figure 3.2: Plots of the field $\cos\theta$ of the wall (a) and the energy density (b) for three values of the parameter g are shown: $g = 0$ (red curves), $g = 0.25$ (green curves); $g = 0.5$ (blue curves).

we shall see will produce a Skyrmion on the domain wall. Explicitly we consider a field of the form

$$\boldsymbol{\phi} = (\sin\varphi\,\sin\theta, \cos\varphi\,\sin\theta, \cos\theta). \tag{3.1.9}$$

where φ is a function of x and t only. We will use this later as an initial condition to find the static Skyrmion on the domain wall.

If we ignore the back-reaction of the field φ on the domain wall profile field $\theta(y)$ we can obtain a $(1+1)$-dimensional effective theory for the Skyrmion dynamics along the domain wall. Restricting to the domain wall at $y = 0$, so where $\theta = \pi/2$, and substituting the field (3.1.9) into the Lagrangian density (3.1.3) we find

$$\mathcal{L}_{SG} = \frac{1}{2}(\partial_t\varphi)^2 - \frac{1}{2}(\partial_x\varphi)^2 + \frac{gm^2}{2}\cos\varphi - \frac{m^2}{2}, \tag{3.1.10}$$

which we can see is the Lagrange density of a sine-Gordon model as we saw in Chapter 1 in equation (1.3.6), up to an additional constant which is irrelevant. The vacuum solutions to this theory are given by $\varphi = 2\pi k$ for some $k \in \mathbb{Z}$. Since the field has infinite energy the kink field need not take vacuum values at spatial infinity. However, since we want the field to approximate Skyrmions, we want to introduce some integer winding in this direction, and so choose the field φ to take vacuum values at spatial infinity. This corresponds to the fact that we have $\boldsymbol{\phi} \to (0, 1, 0)$ as $x \to \pm\infty$ along the domain wall. Thus given $\varphi \to 2\pi N_\pm$ as $x \to \pm\infty$ we have a conserved kink number $N = N_+ - N_-$. The sine-Gordon model is integrable and the $N = 1$ static solution is given analytically by

$$\varphi = 4\arctan\left(\exp\left(m\sqrt{\frac{g}{2}}x\right)\right), \tag{3.1.11}$$

where we have located the kink at the origin. Using this kink function in our description of the field (3.1.9) gives us a planar configuration where we have a kink located on a domain wall. Even though it does not give us an exact solution to the field equations, it is in good agreement to numerical simulations of the full model as we shall discuss in more detail later.

An alternative approach to purely restricting to the particular case of $\theta = \pi/2$ relating to the domain wall is to integrate out the y dependence from the Lagrangian. This also gives us a sine-Gordon model with slightly different scales,

$$\widetilde{\mathcal{L}_{SG}} = \int \sin^2\theta\, dy \left(\frac{1}{2}(\partial_t\varphi)^2 - \frac{1}{2}(\partial_x\varphi)^2 - \frac{m^2}{2}\right) + \frac{gm^2}{2}\int \sin^5\theta\, dy \cos\varphi, \tag{3.1.12}$$

however since we have no analytic form of $\theta(y)$ this makes this method less tractable. These integrals can be computed numerically to find the scales of this alternate effective theory and it is found that while they are again similar to those found in the full theory, the more simplistic approach is in slightly better agreement when compared to the full theory and so it is the more simplistic approach to the restriction to the theory along the domain wall which we shall consider here.

The winding that is occurring on the (x, y)-plane for this domain wall Skyrmion can be seen in Figure 3.1(b). Parallel to the y axis we see that ϕ_3 increases monotonically from -1 to $+1$ as we saw for the pure domain wall solution, with the (ϕ_1, ϕ_2) component of the field having a fixed direction. Along lines parallel to the x direction we see that ϕ_3 is fixed, and so (ϕ_1, ϕ_2) has fixed magnitude, but the direction of the (ϕ_1, ϕ_2) vector undergoes one full rotation along these lines. As we expected from the effective kink theory, the (ϕ_1, ϕ_2) vector is asymptotically vertical at each end of the line. Thus we see that the field realises every point on the target sphere exactly once. The location of the domain wall Skyrmion then has the natural definition as the point at which the field takes the value $(0, -1, 0)$. Essentially, since we have that $\boldsymbol{\phi} \to (0, \sin\theta, \cos\theta)$ as $x \to \pm\infty$ we are identifying the edges at infinity in the x direction, and have also compactified to a point at positive and negative infinity in the y direction. Thus we have that topologically $\boldsymbol{\phi}$ is again a map between two spheres and so has associated topological charge as in the baby Skyrme model of

$$B = -\frac{1}{4\pi} \int \boldsymbol{\phi} \cdot (\partial_x \boldsymbol{\phi} \times \partial_y \boldsymbol{\phi})\, d^2x \tag{3.1.13}$$

which is equivalent to the integer number of twists introduced along the domain wall.

To obtain a true static unit charge domain wall Skyrmion we use the field generated by (3.1.9) and apply an energy minimising gradient flow algorithm using the static version of energy (3.1.4). Since m gives an overall scaling we may set it to be unity without any loss of generality, while in the numerical simulations we choose to set $g = \frac{1}{2}$ unless we state otherwise. We performed our simulations for a range of g and found that there was no difference in the qualitative features of the solutions to the theory. The numerical simulations were undertaken on a square lattice with

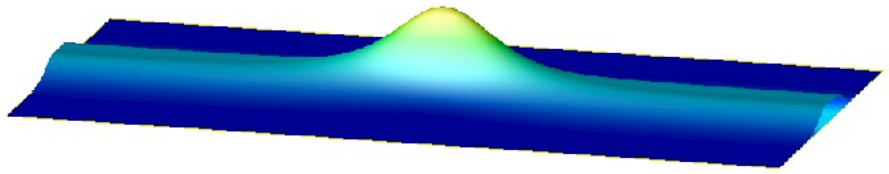

(a)

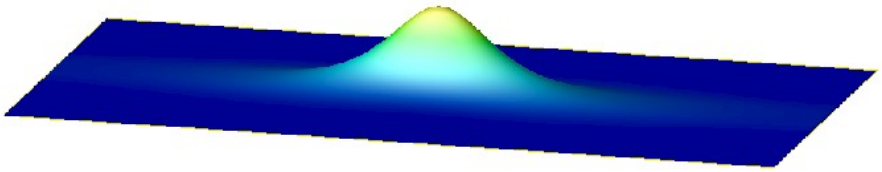

(b)

Figure 3.3: The energy density (a) and the topological charge density (b) of the static Skyrmion on a domain wall.

lattice spacing $\Delta x = \Delta y = 0.08$ and the smallest grid used contained 301×151 lattice points, with larger grids used for computations with multi-Skyrmions. Spatial derivatives are approximated by a fourth-order accurate finite difference scheme. We impose mixed boundary conditions onto the field such that it satisfies the Dirichlet condition $\boldsymbol{\phi} \to (0, 0, \pm 1)$ as $y \to \pm\infty$ and Neumann condition $\partial_x \boldsymbol{\phi} \to 0$ as $x \to \pm\infty$. Numerically these Dirichlet and Neumann boundary conditions are applied to the boundary of the numerical grid.

In Figure 3.3(a) we plot the energy density, the integrand of (3.1.4), of the field with unit charge. The domain wall can be clearly seen, with the Skyrmion located upon it. In Figure 3.3(b) for the same solution we plot the charge density, the integrand of (3.1.13). We see that as in the energy density plot there is a concentration of charge located at the location of the Skyrmion, however there is no charge density along the domain wall, since this does not contribute to the charge density.

We see that the domain wall Skyrmion appears to be stretched along the domain wall, rather than being axially symmetric as in the usual theory. We can understand this behaviour by considering the effective theories along and perpendicular to the domain wall. From equation (3.1.10), by considering the behaviour of the kink under

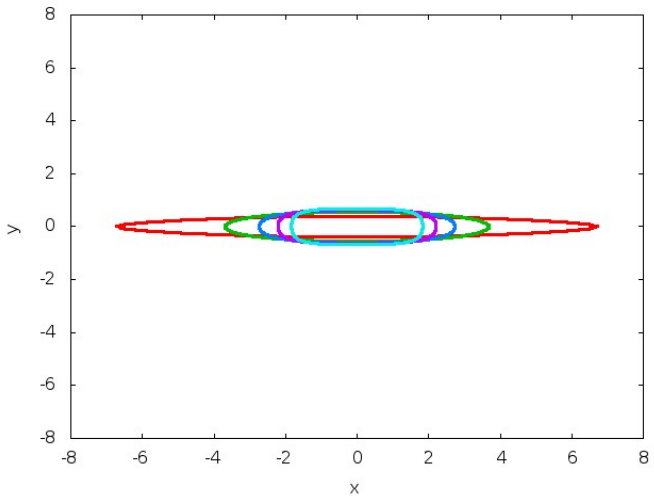

Figure 3.4: Plot of the isoline where the energy density is 1.0 for $m = 1$ and $g = 0.1$ (red), $g = 0.3$ (green), $g = 0.5$ (blue), $g = 0.7$ (magenta) and $g = 0.9$ (cyan). From this we see that the stretching of the domain wall Skyrmion along the domain wall decreases as a function of parameter g.

a rescaling in the x direction, we can see that the width of the kink scales with our parameters as $1/(m\sqrt{g})$. For the domain wall system such a derivation is more complicated due to the additional term contributing, however we know that in the limit $g \to 0$ the width of the domain wall scales as $1/m$. We therefore see that for small g the width of the kink is greater than that of the domain wall and hence the Skyrmion appears stretched along the domain wall. In Figure 3.4 we plot an isoline of the energy density for a range of g, while keeping m fixed. The choice of isoline, where the energy density was unity was chosen to give an idea of the stretching of the Skyrmion along the domain wall. We see that as g increases towards one this stretching effect along the domain wall is reduced.

Although the presence of a domain wall means that the energy is infinite, the amount of energy which is contributed purely from the Skyrmion is finite and can easily be calculated by taking the difference between the energy of the domain wall Skyrmion and the pure domain wall solutions. We have done this for a range of the parameter g so we can see how the parameter effects the energy of the soliton in the theory. We see in Figure 3.5 that the energy increases approximately linearly with g for most of the range of g.

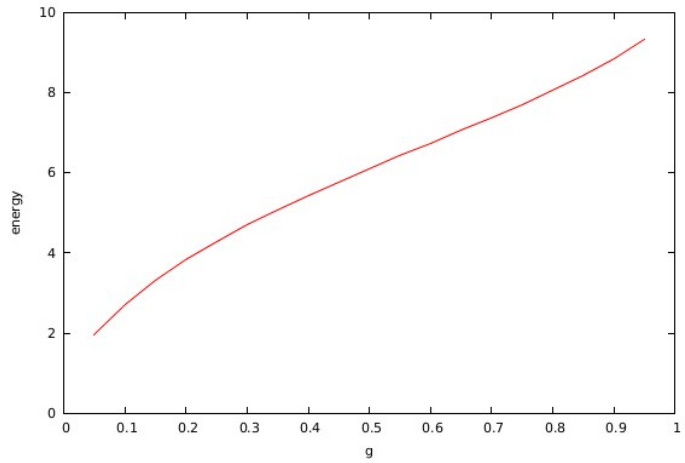

Figure 3.5: The energy of the static Skyrmion as a function of the parameter g, where we have negated the energy contribution from the domain wall.

3.2 Skyrmion Dynamics

To simulate the dynamics of domain wall Skyrmions we numerically solve the non-linear wave equations which follow from the variation of Lagrangian density (3.1.3). Spatial aspects of the numerical set up are as described for the static solutions presented. Time evolution is simulated numerically using a fourth-order Runge-Kutta method with a time step of $\Delta t = 0.02$.

To test the stability of the static solution presented previously we examine the evolution of a range of initial conditions generated by different perturbations of the static solution. An example of such an evolution can be seen in Figure 3.6, where we have introduced a perturbation of the domain wall from the line $y = 0$, as can be seen in the top image. This perturbation causes the domain wall to oscillate about the the line $y = 0$, but the Skyrmion remains intact and on the domain wall during this motion. The amplitude of these oscillations slowly decreases as the wall radiates, which is allowed due to our Neumann boundary conditions. Eventually the static domain wall is recovered. This provides strong evidence for the stability of the static domain wall Skyrmion found in the previous section.

We now consider two domain wall Skyrmions located on the same domain wall moving along the domain wall. We saw previously that along the domain wall a sine-Gordon effective theory can be derived for this. As it is known that two sine-

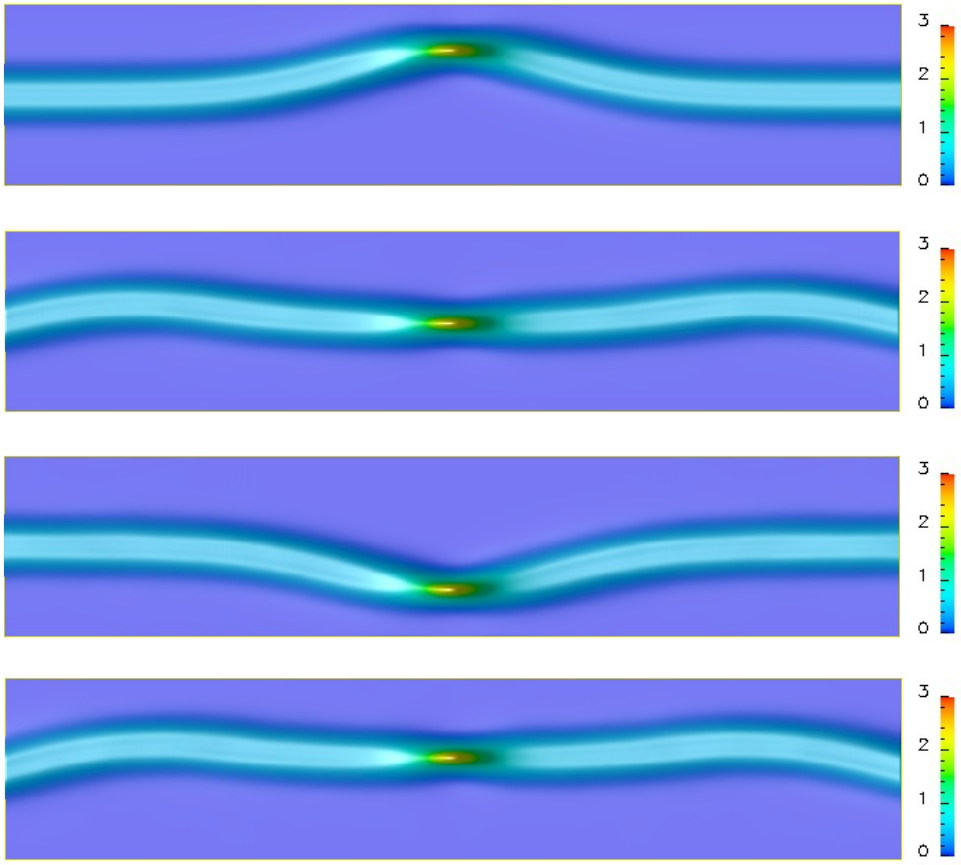

Figure 3.6: Energy density plots at increasing times (from top to bottom $t = 0, 25, 60, 100$) for a perturbed domain wall Skyrmion.

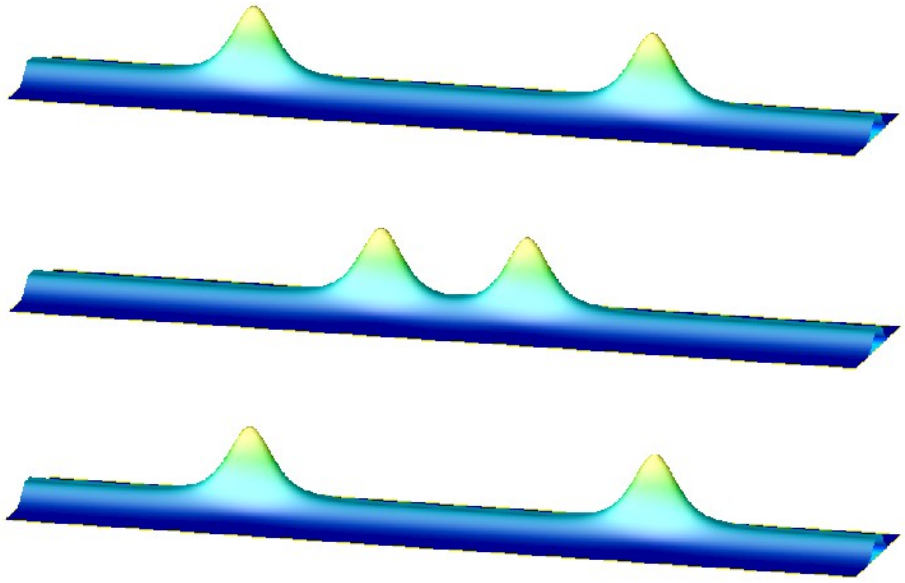

Figure 3.7: Energy density plots at increasing times (from top to bottom $t = 0, 54, 108$) for the scattering of two Skyrmions. Each Skyrmion has an initial velocity $v = 0.2$ towards the other Skyrmion.

Gordon kinks are repulsive [6], we would expect two domain wall Skyrmions in our model to also have a repulsive force between them. We confirm this is indeed the case by evolving a field with two well separated Skyrmions on the domain wall in time and seeing that they indeed repel away from each other. Further to this we can also study the scattering of two Skyrmions along the domain wall. An example of such a scattering is shown in Figure 3.7 where each domain wall Skyrmion is Lorentz boosted towards the other along the domain wall with speed $v = 0.2$. The Skyrmions approach a minimal separation before bouncing back due to the repulsive force in an almost elastic collision, with very little radiation being generated. We have studied scatterings for a range of initial velocities $0.1 \leq v \leq 0.7$ and have found similar behaviour in each case.

We see that the scattering above appears to be linear along the domain wall, so we would like to compare the scattering behaviour we have observed with that of our effective (1+1)-dimensional sine-Gordon kink theory found by restricting to along the domain wall. This theory is integrable and the solution of the scattering of two

sine-Gordon kinks is known analytically. In Chapter 1 we discussed the construction of such a field in more detail. The field is given by

$$\varphi = 4 \arctan\left(\frac{v \sinh(\gamma m \sqrt{\frac{g}{2}} x)}{\cosh(\gamma m \sqrt{\frac{g}{2}} v(t - t_0))}\right), \tag{3.2.14}$$

where $\gamma = 1/\sqrt{1 - v^2}$ and t_0 is the kink separation at time zero, which is fixed to match with the initial conditions of the full field theory simulations.

In Figure 3.8 we plot curves representing the field in a scattering at successive time points. We plot the scattering for $v = 0.2$ in the left column and for $v = 0.6$ in the right column. For each plot we show in red the curve of $-\phi_2$ where we restrict the field to that along the domain wall ($y = 0$). On the same plots in blue we plot $-\cos\varphi$ given by the exact sine-Gordon two-kink scattering solution in equation (3.2.14). We see that there is a good agreement between the full field dynamics restricted to the domain wall and the kink scattering in our effective theory. The main differences between them is that the minimal separation of the domain wall Skyrmions is less than that for the kink theory. The domain wall Skyrmions get closer together before they repel which we can understand as the Skyrmions exploring the extra dimension as they collide and squeeze together. This factor also results in the time taken for the the domain wall Skyrmions to be repelled to be longer than for the kink scattering and so we see a slight time delay in the bouncing back of the domain wall Skyrmions when comparing with the kinks of the effective theory. We can see this in Figure 3.8 where in the latter time steps shown the red curves are closer to the origin than the blue. This discrepancy becomes more evident as we increase the scattering speed v, as can be seen in the right column where the separation is very obviously different. The peaks of the red curve get much closer together than the blue curves, and the resulting time delay between them being repulsed becomes more pronounced. We interpret this as the increase in speed giving the domain wall Skyrmions more energy with which to explore the additional dimension.

This analogy with kinks suggests a range of possibilities for phenomena in the full model which are known to occur for kinks in the sine-Gordon theory such as breather states, which would be interesting if we find the corresponding Skyrmion anti-Skyrmion states occurring on the domain wall. It is not known however how the

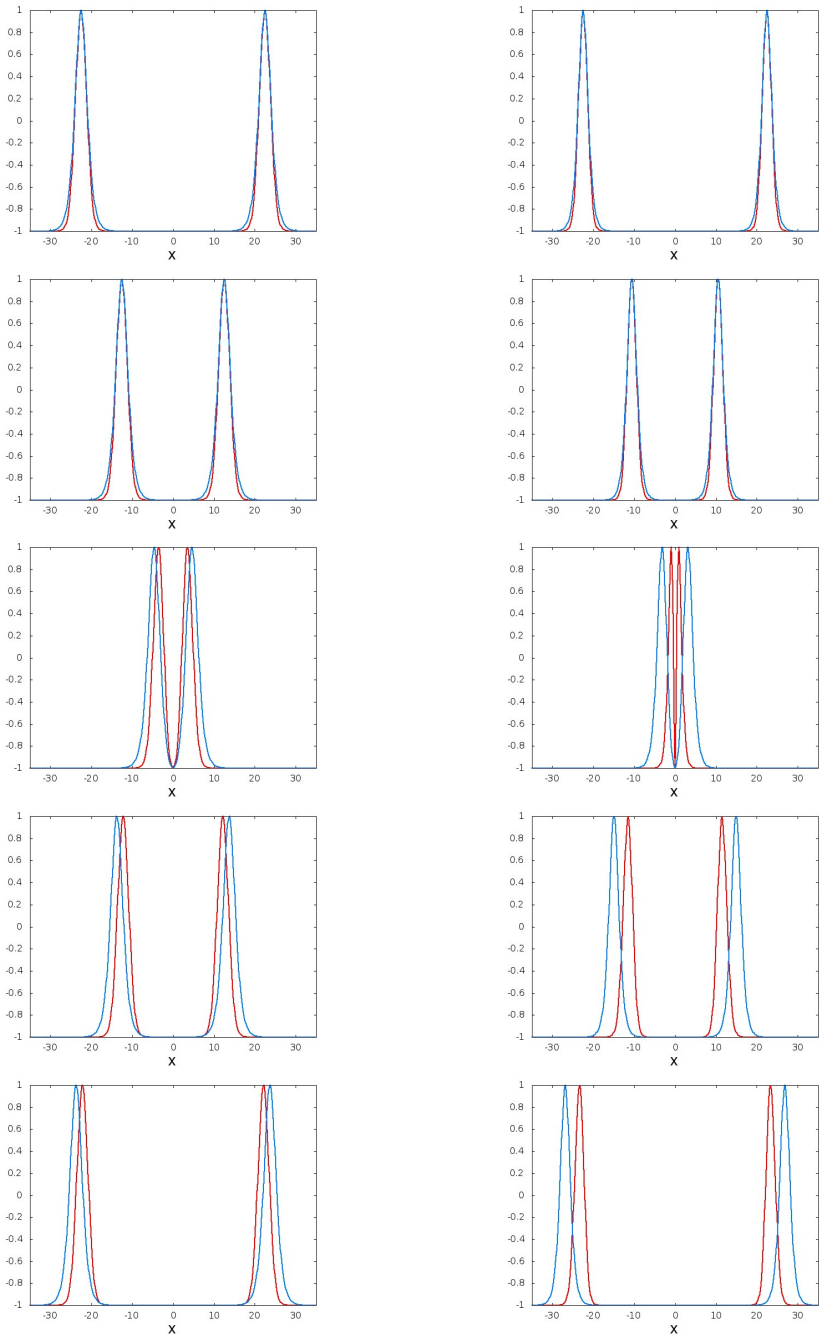

Figure 3.8: The field $-\phi_2$ (red curves) along the domain wall $y = 0$ at increasing times (from top to bottom) for an initial configuration in which each Skyrmion has an initial velocity v towards the other Skyrmion. The associated sine-Gordon approximation is also shown (blue curves). The images on the left are for $v = 0.2$ and times $t = 0, 50, 100, 150, 200$. The images on the right are for $v = 0.6$ and times $t = 0, 20, 40, 60, 80$.

effect of the additional dimension might impact upon the existence of such states. In such scatterings there would be a lot of kinetic energy due to the annihilation between Skyrmion and anti-Skyrmion, which may well dissipate in the additional direction. We now turn our attention to scattering of Skyrmions which is beyond the reach of this (1+1) effective kink theory by considering a scattering which is a fully planar process.

To implement this scattering we introduce multiple domain walls in the plane. Due to the vacuum structure of the theory, it is not possible to create two identical walls parallel to one another to then scatter. Instead we require one of these to be an anti-wall, which is realised by a wall configuration after the transformation $\phi_3 \mapsto -\phi_3$ has been applied. In general, wall and anti-wall configurations annihilate when located near each other initially. We see that in such a configuration after annihilation of the domain walls the Skyrmion would have no domain wall structure to provide it stability, and so we would expect no Skyrmions to survive such scattering events. Indeed this is what is found when such initial conditions are used in our simulations, with the Skyrmion collapsing and the field becoming an excited state of a single vacuum value.

Instead we consider the scattering of two domain walls with an anti-wall located between them. In this case there will be a remaining domain wall after annihilation for the resulting Skyrmions to be located on and so allow the possibility of stable domain wall Skyrmions after the scattering event. As the annihilation of domain walls introduces a lot of additional kinetic energy to the system a damping term has been included to the dynamical equations of motion to aid the dissipation of some of this kinetic energy. This aids visualisation since a large amount of kinetic energy can swamp the energy density contribution coming from the domain wall Skyrmion itself. A large amount of kinetic energy can also cause numerical difficulties when this radiation bounces back into the centre of the numerical grid, which is obviously not physical and a damping term helps to reduce this.

An example of such a scattering event is shown in Figure 3.9. There are domain walls located along $y = \pm 7$ and an anti-wall along $y = 0$. We position a domain wall Skyrmion on each of the walls at positions given by $(-1, -7)$ and $(1, 7)$. This

initial field can be seen in the top image of Figure 3.9. Initially we set all time derivatives of the field to be zero and evolve the field from rest. The attractive force between the walls and anti-wall generates motion of the two domain walls towards the anti-wall. Where the Skyrmions are located we see that the speed of the wall is reduced. Since we have offset the Skyrmions from each other in the x direction, those parts of the domain walls without the Skyrmions located on them annihilate with the anti-wall first. Thus after annihilation we have two half-walls each with the Skyrmion on, and which connect to each other to create a single domain wall with a distinctive sigmoid shape, as can be seen in the middle image of Figure 3.9. The domain wall then straightens and the Skyrmions on the domain wall repel each other as we have already seen for two Skyrmions on a single domain wall. This scattering behaviour provides further evidence for the stability of the domain wall Skyrmion in that these structures survive such a violent scattering process.

We have undertaken simulations for a range of initial conditions with different offset of Skyrmions in the x component and with different strengths of damping term and the features of the scatterings were qualitatively unchanged. We found that if there was no initial offset between the Skyrmions placed on the domain wall that there is nothing to break this inherent symmetry and the Skyrmions can no longer separate. This highly symmetric situation is however very unstable, with even tiny numerical effects enough to break the symmetry to yield similar scattering events to that described above.

3.3 Conclusions

In this chapter we have been looking at a particular model in which we find static Skyrmion solutions, but which does not include any higher order derivative terms. We have examined the stability of such solutions and found that although there is no topological term ensuring that they be stable, solutions have a finite scale so long as they are located on a domain wall. We have tested the stability of such static solutions by performing perturbations in the dynamical system.

We have looked at multi-Skyrmion scattering along the domain wall within

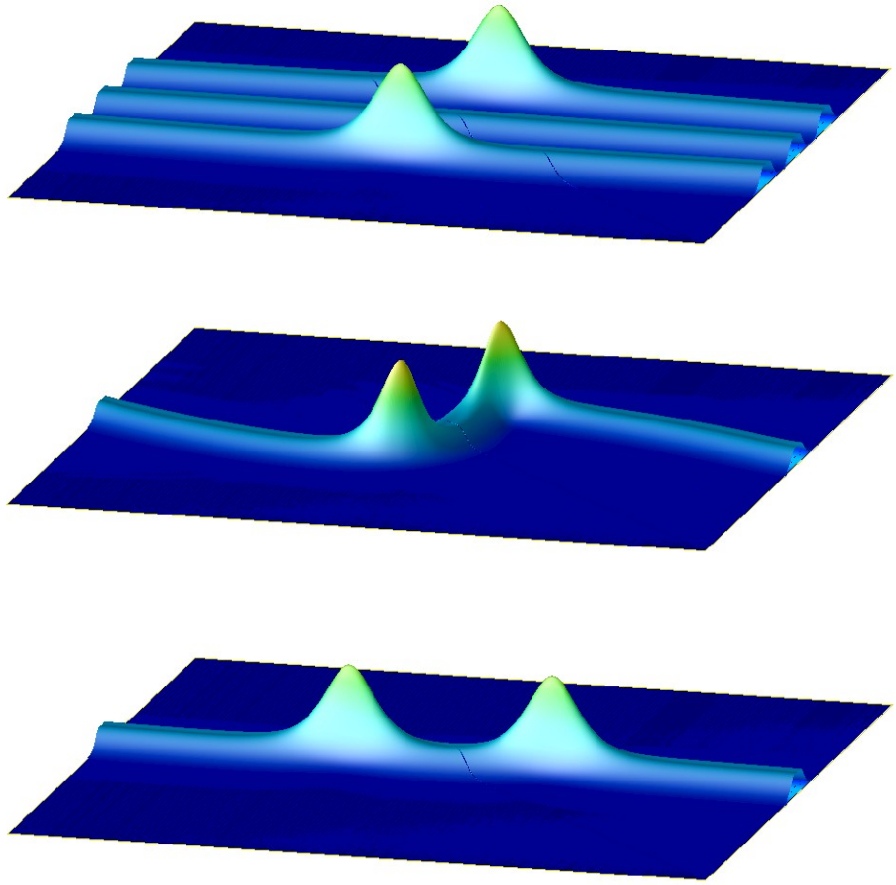

Figure 3.9: Energy density plots at increasing times for the evolution (with damping) of two Skyrmions that are initially on different domain walls. In the top image ($t = 0$) the two Skyrmions have initial positions $(-1, -7)$ and $(1, 7)$. There are walls along $y = \pm 7$ and an anti-wall along $y = 0$. All time derivatives are initially zero. In the middle image ($t = 60$) the Skyrmions have survived the wall anti-wall annihilation process. In the bottom image ($t = 135$) the Skyrmions are moving apart along the remaining straight wall.

the model and compared scattering along the domain wall to an effective $(1+1)$-dimensional theory of kink scattering. It was found that the full theory and this effective theory are in good agreement for scattering at low speeds, with some differences emerging at higher speeds. It would be interesting to see whether other phenomena of this effective theory such as breather states can exist in the model.

We have also seen more exotic scatterings of Skyrmions on multiple domain walls which make use of the planar structure of the theory. We have seen that the scattering events in such a theory can be quite complicated and differ from the usual dynamics found in theories where a Skyrme term is included. We have found that it is possible for domain wall Skyrmions on different domain walls to survive scattering events, and to move between different domain walls.

The current work also leaves open the question as to the existence of similar theories in which domain wall junctions occur with Skyrmions existing along these domain walls. Although the system which we consider here is unable to support such domain wall networks since it does not have a suitable vacuum structure [4, 47, 48], as our model only has the two vacua, it would be interesting to see whether such a theory could exist with stable domain wall Skyrmions. It would be interesting to find the effect such structures have on the dynamics, whether it would be possible for the Skyrmion to move along the domain walls in a similar way to how we have found for this model. In principle a simple change to our model by allowing for the case $g = 1$ should allow for such domain wall networks by introducing an additional vacuum value into the potential. However it is not clear how the presence of additional vacua in the theory would effect the stability and dynamics of such a theory.

The form of the potential has the leading behaviour of a uniaxial magnetocrystalline anisotropy term where one easy axis is introduced with which magnetisation alignment is preferred. Thus the choice of potential has some physical motivation. It would however be nice to try and find particular physical systems for magnetic materials with similar subleading anisotropy behaviour to that introduced in our choice of potential term.

For simplicity, our current work has been concerned with a planar theory. Similar models are known for (3+1)-dimensional theories [43, 44, 45] and we would expect

similar results to those detailed in this chapter to apply for these. It might be of interest to extend our simulations to these theories to see what type of behaviour is found, and whether further examples of complex scattering events can occur.

The higher derivative terms required for a Skyrme term are often problematic since these higher order terms do not tend to arise naturally within physical theories. On the other hand, domain walls are a phenomena which occur frequently in a wide range of models from many areas such as cosmology, high-energy physics and condensed matter systems. It is therefore of interest to look at the properties which our domain wall Skyrmions possess since they have the potential to be applicable to a wide range of physical theories.

Chapter 4

Cabling in the Skyrme-Faddeev model

In this chapter we concern ourselves with the Skyrme-Faddeev model. This is a (3+1)-dimensional modified $O(3)$ sigma model with a Skyrme term included. It has topological soliton solutions which take the form of knots and links. As we have seen in the introduction this model can be thought of as either a restriction of the three-dimensional Skyrme theory or as being constructed as strings formed of baby Skyrmions living in the plane transverse to the string direction. The Skyrme-Faddeev model has a number of applications. The model has potential links to low-energy QCD, with it having been suggested that this model may describe glueballs [30], and applications have also been suggested in condensed matter systems [31]. However, as mentioned in the Introduction, these are somewhat controversial and evidence has been found that this may not be the case. The model is also a good testing ground for knotted field structures which are expected to appear in a range of models.

As we recap briefly in the following section, the Skyrme-Faddeev has been shown to contain fields with the form of torus knots and links formed from unknots. In this chapter we shall present work on finding knots which are more general than this. For this we will introduce a number of definitions and notions from knot theory which we shall need. One useful classification is that knots are either torus knots, satellite knots or hyperbolic knots [49]. Torus knots are knots which can be drawn on the

surface of a torus without any crossings occurring on the surface. These types of knot are well known to occur in the model. The trivial unknot is also obviously of this type. The second set of knots which we wish to consider are called satellite knots. Consider a knot K_1 lying within a solid torus. If we then knot the solid torus into a knot K_2 then the resulting knot is a satellite knot. Cable knots, which we will see more of in this chapter, are a special case of these where K_1 and K_2 are torus knots. The satellite knot category contains all composite knots, knots formed by joining two knots together. The final class contains all knots which do not fall into either of the other categories. A knot is hyperbolic if its compliment (that is S^3 with a neighbourhood of the knot removed) can be given a metric of constant curvature -1. If a knot is hyperbolic then one can define its hyperbolic volume as the volume of the complement with respect to this metric. This quantity is a knot invariant in that any depiction of such a knot will have the same hyperbolic volume. We shall refer to the hyperbolic volume of knots later in this chapter. We shall also mention two tabulations of knots with a low number of crossings. The first is the table compiled by Rolfsen [50] which is of the form n_i where n denotes the (unsigned) crossing number and i labels each knot. We also refer to hyperbolic knots via their Callahan-Dean-Weeks-Champanerkar-Kofman-Patterson notation [51, 52, 53] which is of the form kn_i where the k differentiates it from Rolfsen's notation, n denotes the number of hyperbolic tetrahedra which are needed to cover the knot complement (and so gives an idea of the complexity of the knot) and i labels each knot.

It is well known that the solitons of the Skyrme-Faddeev model, hopfions, can take the form of torus knots [34], however it was an open question whether any other types of knot existed in the model. In this chapter we present a method of constructing fields which are knotted as cable knots. We then see that solutions of these forms are indeed seen in the model, as well as finding the first known solutions which are knotted in the form of hyperbolic knots.

4.1 The Skyrme-Faddeev model

The Skyrme-Faddeev model involves a map $\boldsymbol{\phi} : \mathbb{R}^3 \to S^2$, which we parametrise as a three-component unit vector. Since in this chapter we are considering only static fields, we may define the Skyrme-Faddeev model via the static energy functional of this field. From the Lagrangian corresponding to (1.6.49) we find the static energy

$$E = \frac{1}{32\pi^2\sqrt{2}} \int \partial_i \boldsymbol{\phi} \cdot \partial_i \boldsymbol{\phi} + \frac{1}{2}(\partial_i \boldsymbol{\phi} \times \partial_j \boldsymbol{\phi}) \cdot (\partial_i \boldsymbol{\phi} \times \partial_j \boldsymbol{\phi})\, d^3x. \tag{4.1.1}$$

For the field to have a finite energy it must tend towards a constant vector at spatial infinity, which we choose to be $\lim_{|\mathbf{x}|\to\infty} \boldsymbol{\phi}(\mathbf{x}) = \boldsymbol{\phi}_\infty = (0, 0, 1)$ without loss of generality. This identification leads to a one-point compactification of physical space so the field is a map $\boldsymbol{\phi} : S^3 \to S^2$ and so has topological conserved quantity given by the Hopf invariant, which we discussed in more detail in the Introduction. It will be useful to use the notion of the Hopf charge as the the linking number of the preimage of two distinct points of the target S^2 [33]. A sketch of this is shown in Figure 1.4 for the preimages of two points for a configuration with $Q = 1$.

In this study we restrict to solutions with positive Hopf charge, since solutions with a negative charge can be obtained by a spatial reflection, which changes the sign of the charge. It will also be useful to note that one can consider the Hopf charge as being composed of the crossing number of the the location curve plus the winding number of the second curve about this. However these individually are not topologically conserved quantities since the crossing number is obviously not preserved under a type-I Reidemeister move.

Recall that the energy functional (4.1.1) obeys the Vakulenko-Kapitanskii bound [35]

$$E \geq c\,|Q|^{3/4}, \tag{4.1.2}$$

where the sublinear growth of the energy is due to the use of complicated Sobolev inequalities. This can be understood physically as a consequence of the creation of additional charge through the knotting and linking of solitons. The inequality has been proven for $c = (3/16)^{3/8} \approx 0.534$ [36], although it is believed this value is not optimal, with it conjectured by Ward that $c = 1$ should be the optimal value [37].

In previous studies it has been observed that solutions exceed Ward's conjectured bound by approximately 20%, which is a phenomenon found in other Skyrme models.

No analytic solutions to the model defined by energy functional (4.1.1) are known, but it has been demonstrated in previous numerical work that the qualitative structure of solutions can be captured by fields generated via rational maps [34,54,55]. An energy minimisation scheme can then be implemented to find solutions. We begin by mapping physical space $(x_1, x_2, x_3) \in \mathbb{R}^3$ to the unit three-sphere $(Z_1, Z_0) \in S^3 \subset \mathbb{C}^2$ via the map

$$(Z_1, Z_0) = \left((x_1 + ix_2)\frac{\sin f}{r}, \cos f + i\frac{\sin f}{r}x_3 \right), \tag{4.1.3}$$

where $r^2 = x_1^2 + x_2^2 + x_3^2$ and $f(r)$ is a monotonically decreasing function satisfying $f(0) = \pi$ and $f(\infty) = 0$. The Riemann sphere coordinate of the field $\boldsymbol{\phi}$ is then given by rational map $W : S^3 \subset \mathbb{C}^2 \to \mathbb{CP}^1$ given by

$$W(Z_1, Z_0) = \frac{\phi_1 + i\phi_2}{1 + \phi_3} = \frac{p(Z_1, Z_0)}{q(Z_1, Z_0)}, \tag{4.1.4}$$

for some polynomial functions p and q with no common factors and which have no common roots on the two-sphere. Since we have fixed the field at infinity it is natural to interpret the location of the soliton as the preimage of $\boldsymbol{\phi} = (0, 0, -1)$, the antipodal point to $\boldsymbol{\phi}_\infty$. Thus the location of the hopfion is given by the centreline of the string-like solitons. It can be seen that this location relates to where $q(Z_1, Z_0) = 0$ in the rational map, while the numerator $p(Z_1, Z_0)$ describes the behaviour of the field about this centreline and so is important for defining the Hopf charge of the ansatz. We also require $p(Z_1, Z_0)$ to be such that $W \to 0$ as $r \to \infty$, to satisfy the boundary conditions of the field.

The topological charge generated by a given rational map of the form (4.1.4) can be calculated by considering a natural extension of W. Let $\widetilde{W} : \mathbb{B}^4 \subset \mathbb{C}^2 \to \mathbb{C}^2$ given by $(Z_1, Z_0) \mapsto (p(Z_1, Z_0), q(Z_1, Z_0))$. Here $(Z_1, Z_0) \in \mathbb{B}^4$ are given by relaxing the constraint of (Z_1, Z_0) lying on S^3, to $|Z_1|^2 + |Z_0|^2 \leq 1$. Consider the preimages of a regular point close to the roots of $\widetilde{W}$. Consider a three-sphere about each of these preimages, such that the roots of $\widetilde{W}$ are contained within the three-spheres. $\widetilde{W}$ imposes, up to some normalisation, a unit vector field in S^3 on the four-ball excluding the roots of $\widetilde{W}$. Since p and q are holomorphic, the map from each

three-sphere to the vector field has unit topological charge. Taking a connected sum of these spheres maintains the charge and one can then deform this surface to the boundary of the four-ball. Thus the topological charge of the mapping from the S^3 forming the boundary of the four-ball to the vector field taking values in S^3 has topological charge given by the number of preimages under $\widetilde{W}$ of a regular point. The standard Hopf mapping is then used and we see that any normalisation factor in the definition of the vector field cancels, so we regain W. Since under the standard Hopf mapping, the Hopf charge of the map is the topological charge of the map between three-spheres, it follows that the Hopf degree of W is the number of preimages inside the four-ball of a regular point under $\widetilde{W}$.

We now briefly recap the types of rational map that have been used previously and introduce our notation for referring to these. Axially symmetric solutions have long been known to exist in the model, and fields with the correct structure are generated by the rational map,

$$W = \frac{Z_1^m}{Z_0^n}, \tag{4.1.5}$$

for m and n positive integers. This field describes an axial solution which winds n times longitudinally and m times in the meridional direction. This results in a field configuration with $Q = mn$, since $(Z_1^m, Z_0^n) = (\epsilon, \epsilon)$ has mn solutions. We shall denote such field configurations by $\mathcal{A}_{m,n}$. These appear for low charges as the energy minima of the system. An example of a solution with such a form is given by the charge one energy minima $\mathcal{A}_{1,1}$ which is shown in Figure 4.1(a). Further examples of this form can also be seen in the next chapter.

A knotted field configuration of the form of an (a, b)-torus knot is given by

$$W = \frac{Z_1^\alpha Z_0^\beta}{Z_1^a + Z_0^b}, \tag{4.1.6}$$

for a and b coprime, α a positive integer and β a non-negative integer. We can see that this must indeed form a torus knot since it is known that the intersection of the plane curve $Z_1^a + Z_0^b = 0$ and the unit three-sphere results in an (a, b)-torus knot [56]. To find the number of preimages of $(Z_1^\alpha Z_0^\beta, Z_1^a + Z_0^b) = (\epsilon, 0)$ we note that solutions of this are contained within solutions to $Z_1^\alpha Z_0^\beta = \epsilon$ and $Z_1^{a\beta} = (-1)^\beta Z_0^{b\beta}$. Solving this second pair of equations we find $Z_1^{a\beta+b\alpha} = (-1)^\beta \epsilon^b$ and for each Z_1

from the first equation we have β roots which Z_0 can satisfy. Thus this system has $\beta(a\beta + b\alpha)$ solutions. It remains to determine how many of these will correspond to solutions of the first set of equations. We note that the second set of equations can be written as equations $Z_1^\alpha Z_0^\beta = \epsilon$ and $\lambda_1 Z_1^a = -\lambda_2 Z_0^b$ for λ_i being β'th roots of unity. Obviously this only satisfies the first set of equations for $\lambda_1 = \lambda_2$, so only $a\beta + b\alpha$ of the solutions also satisfy the first set of equations. Thus the rational map must have Hopf charge $Q = a\beta + b\alpha$. An (a, b)-torus knot is equivalent to an (b, a)-torus knot, so we shall denote such fields by $\mathcal{K}_{a,b}$ with the convention that $a > b$. An example of a hopfion knotted in such a way is found at charge seven, as shown in Figure 4.1(c).

A rational map with denominator that is reducible into distinct factors generates a field with multiple components, each relating to a factor of the denominator. This allows us to construct a field that takes the form of a link. For example, a link of $\mathcal{A}_{m,1}$ and $\mathcal{A}_{n,1}$ is given by rational map

$$W = \frac{Z_1^{m+1} + Z_1^{n+1} + Z_0(Z_1^m - Z_1^n)}{2(Z_1^2 - Z_0^2)} = \frac{Z_1^m}{2(Z_1 - Z_0)} + \frac{Z_1^n}{2(Z_1 + Z_0)}, \tag{4.1.7}$$

where we see that each of the constituent parts is of the form of (4.1.5) after a suitable transformation of the denominator to form the correct linking behaviour. We shall denote this link structure for torus knots as $\mathcal{L}^{\ell_1,\ell_2,\cdots}_{Q_1(a_1,b_1),Q_2(a_2,b_2),\cdots}$. Since we take preimages of points which are close, one can naturally distinguish a pair of curves per component of the link. The subscript gives the linking number Q_i of this pair of curves for each component with form $\mathcal{K}_{a_i,b_i}$. The corresponding superscript then gives the additional charge gained by linking of the location curve with the second preimage of other components. Thus the Hopf charge of the link is given by summing the Q_i and ℓ_i. For example, (4.1.7) gives $\mathcal{L}^{1,1}_{m(1,1),n(1,1)}$, however in the case where components are trivial torus knots of the form $\mathcal{A}_{m,1}$, we shall shorten our notation to denote these as $\mathcal{L}^{1,1}_{m,n}$, and so coincide with the notation of [34], in which more examples of rational maps to generate links can be found. Note also that if a and b in (4.1.6) are not coprime the torus knot construction degenerates to form a link. Examples of solutions which have the form of this field are shown in Figures 4.1(b) and 4.1(d) for charges five and nine respectively. Further examples of low charge hopfions are shown in more detail in the next chapter.

(a) $1\mathcal{A}_{1,1}$ (b) $5\mathcal{L}_{2,1}$ (c) $7\mathcal{K}_{3,2}$ (d) $9\mathcal{L}^{2,2,2}_{1,1,1}$

Figure 4.1: A selection of well known lower charge solutions demonstrating the forms of solutions. Position curves (blue) and linking curve (green) are shown.

4.2 Cable knots and links

We now turn our attention to finding rational maps which describe fields with the form of cable knots. These are a generalisation of torus knots, and so are a good candidate to appear in the Skyrme-Faddeev model. Given an (m_1, n_1)-torus knot, we can define a tubular neighbourhood about this knot. One can then embed the torus on which a (m_2, n_2)-torus knot lies onto this neighbourhood. The resulting knot formed by this embedding is called the (n_2, m_2) cable on the (m_1, n_1)-torus knot. We shall denote a field knotted in such a way by $\mathcal{C}^{n_2,m_2}_{m_1,n_1}$. Note that, unlike torus knots, the ordering of the parameters in the superscript is now important as in general $\mathcal{C}^{n_2,m_2}_{m_1,n_1}$ is not equivalent to $\mathcal{C}^{m_2,n_2}_{m_1,n_1}$. In Figure 4.2 we sketch the construction of $\mathcal{C}^{2,3}_{3,2}$. In Figure 4.2(b) we see, in green, the thickened neighbourhood of a trefoil knot. We embed the torus of a second trefoil knot, shown in Figure 4.2(a), on to this resulting in knot $\mathcal{C}^{2,3}_{3,2}$ drawn in black in 4.2(b). We have assumed above that each pair (m_i, n_i) are coprime since they label torus knots, however if we relax this condition such that (m_2, n_2) are no longer coprime then we find a link in the neighbourhood of the (m_1, n_1)-torus knot, which is called a cable link. In general we can think of the $\mathcal{C}^{n_2,m_2}_{m_1,n_1}$ knot as being formed from n_2 strands in the neighbourhood of a (m_1, n_1) torus knot, with the strands crossing each other m_2 more times than that imposed by the (m_1, n_1) torus knot.

We now wish to construct a field that is knotted in such a way. Recall that an algebraic link can be described as the intersection of S^3_ξ, the three-sphere of radius $\xi > 0$, with the algebraic plane curve $C = \{(x, y) \in \mathbb{C}^2 : F(x, y) = 0\}$, for some complex polynomial $F(x, y)$ vanishing at $(0, 0) \in \mathbb{C}^2$ and under certain conditions

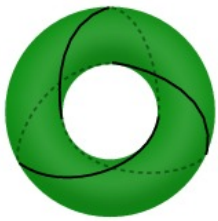

(a) The $(2,3)$-torus knot (the trefoil) on the surface of a torus.

(b) The $\mathcal{C}^{2,3}_{3,2}$ cable knot, lying on a neighbourhood of a trefoil.

Figure 4.2: Sketches of construction of cable knots

on ξ. If $\xi = 1$ is a sufficient radius for the three-sphere to give the desired knot on intersection with C, then we merely need to set $q(Z_1, Z_0) = F(Z_1, Z_0)$. This will be the case for all the knots considered here, however if it were not the case it is simple enough to rescale the coordinates (Z_1, Z_0) such that the parametrisation would work. Given an $F(x, y)$ we can study the Puiseux expansion for y in terms of a fractional power series in x using Newton polygons. From this expansion the type of knot this will generate can be found. However, this would be a long search to find a suitable complex polynomial. Instead we wish to start from such an expansion and generate the corresponding irreducible complex polynomial which it relates to. This is easily achieved following the prescription of [57]. Briefly, to do this we rewrite our complex variables such that $x, y \in \mathbb{C}[t]$, then

$$F(x, y) = \det(yI_n - V) \tag{4.2.8}$$

where $n = \deg(x)$, I_n is the $n \times n$ identity matrix and $V(x)$ is the $n \times n$ matrix defined by

$$yt^{i-1} = \sum_{j=1}^{n} V_{ij} t^{j-1}. \tag{4.2.9}$$

To show that an expansion generates a particular knot we resort to an approach first used by Kähler [58] and instead of $C \cap S^3_\xi$ consider $C \cap D_\xi$, where $D_\xi = \{(x, y) \in \mathbb{C}^2 : |x| = \xi, |y| \leq \xi\}$. It can be shown [59] that a sufficient condition for $C \cap D_\xi$ to be isomorphic to $C \cap S^3_\xi$ is for the radial vector (x, y) to be nowhere orthogonal to all the tangent vectors on C restricted to the four-ball of radius ξ with the origin removed, $\mathbb{B}^4_\xi \backslash \{(0, 0)\}$. Using this alternative description of the knot it is much easier to see the form of the knot, as we shall see in the following.

Before using these methods to find rational maps which produce cable knots, we make this method a little clearer with an example of a field which is knotted as a trefoil, the $(3,2)$-torus knot. As we have seen from the form of the denominator of 4.1.6 we know that $F(x,y) = x^3 + y^2$ from which the expansion is easy to find and show that this indeed describes a trefoil knot. Rather than this we suppose that we do not know the exact form of $F(x,y)$, instead we consider an expansion of the form $y = \eta x^{3/2}$ for some $\eta \in \mathbb{C}$. We note this satisfies the constraint regarding $C \cap S^3_\xi$ being isomorphic to $C \cap D^3_\xi$ thus we consider the latter. This is parametrised by $(x,y) = (\xi t^2, \eta \xi^{3/2} t^3)$ for $t \in S^1 \subset \mathbb{C}$. Thus we have that it traverses in x direction twice and three times in the y direction. Since D_ξ is a solid torus we see that the expansion relates to a trefoil knot. Applying our construction, writing $x, y \in \mathbb{C}[t]$ we get $x = t^2$ and $y = \eta t^3$. Using these in equation (4.2.8) we find

$$F(x,y) = \det \begin{pmatrix} y & -\eta x \\ -\eta x^2 & y \end{pmatrix} = y^2 - \eta^2 x^3, \tag{4.2.10}$$

We see that this coincides with our case for $\eta = i$. Now since we see that $C \cap D_\xi$ gives a torus knot for all ξ, it holds particularly when $\xi = 1$, and so we can simply set $q(Z_1, Z_0) = F(Z_1, Z_0)$.

We now return to our derivation of a rational map with the form of a cable knot. Consider an expansion of the form

$$y = x^{m_1/n_1} + \eta x^{m_2/n_1 n_2}, \tag{4.2.11}$$

for non-zero $\eta \in \mathbb{C}$ and positive integers m_i, n_i which are pairwise coprime and satisfy $1 < m_1/n_1 < m_2/n_1 n_2$. It can be shown [57] that this then generates the (n_2, m_2)-cable on $\mathcal{K}_{m_1,n_1}$. To see this we first note that this satisfies the isomorphism condition since the complex tangent converges to $y = 0$ as we approach the origin. Thus in a small neighbourhood of the origin the vector (x,y) is nowhere orthogonal to all the tangent vectors, since on the curve $|y| \ll |x|$. Considering the intersection with the solid torus, since $|x| = \xi$ is small we see that the leading behaviour in small ξ will come from the first term, so $y \approx x^{m_1/n_1}$. This is parametrised by $(x,y) = (\xi t^{n_1}, \xi^{m_1/n_1} t^{m_1})$ for $t \in S^1 \subset \mathbb{C}$. We see that the curve traverses n_1 times in the x direction, and m_1 times in the y direction, obviously tracing out $\mathcal{K}_{m_1,n_1}$, and

so our knot lies in a neighbourhood of this. Considering the second term, we see that as the curve traverses longitudinally about $\mathcal{K}_{m_1,n_1}$ it rotates m_2/n_2 about the tube of the neighbourhood. Thus it traverses about this neighbourhood n_2 longitudinally and m_2 times in the meridional direction, and so describes an (n_2, m_2) cable on $\mathcal{K}_{m_1,n_1}$ as claimed. For the cases we consider here it is sufficient to take $\xi = 1$, and so (4.2.11) can be used to find fields with a cable knot structure. The first non-trivial knot from this construction is for $\mathcal{C}^{2,7}_{3,2}$ which from expansion (4.2.11) gives

$$F(x, y) = y^4 - 2x^3y^2 - 4\eta^2x^5y + x^6 - \eta^4x^7 \tag{4.2.12}$$

and since we can take $\xi = 1$ it follows that we have rational map

$$W = \frac{Z_1^\alpha Z_0^\beta (Z_1 - Z_0)^\gamma}{Z_0^4 - 2Z_1^3Z_0^2 - 4\eta^2 Z_1^5 Z_0 + Z_1^6 - \eta^4 Z_1^7}, \tag{4.2.13}$$

for α a non-negative integer, β a positive integer and $\gamma \in \{0, 1\}$. The optional term, corresponding to γ is included to enable fields to be generated which have odd topological charge.

We also note that not all values of η will provide us with a rational map that will work. For some values of η a pinching of the location tube occurs which makes such an initial condition unstable. This occurs for the rational map (4.2.13) when we take the value $\eta = 1$. The pinching of this initial condition can be seen in Figure 4.3, where the isosurface about the location curve gets narrower and we see that the curve does not close. We see that this pinching occurs in the x_1 direction, and so if we restrict to the values of the field along $(x_1, 0, 0)$ we can then plot the value of the third component of the field. We see that where the location curve is located this field takes the value of -1. However where we would expect the curve to be the field appears to be approximately constant at 1. We see that for this range Z_1 and Z_0 are real and so can plot the numerator and denominator separately. We see that the issue caused in this case is that the roots of the numerator and denominator coincide, so that W remains finite even though the denominator is zero at that point. Note however that this issue is easily resolved by simply choosing an alternative value for η such that the roots do not coincide. Similar plots to those for $\eta = 1$ are shown in Figure 4.3 when a value of $\eta = 1/2$ is taken in the rational maps for comparison. We can see that for this choice of parameter the pinching no longer occurs.

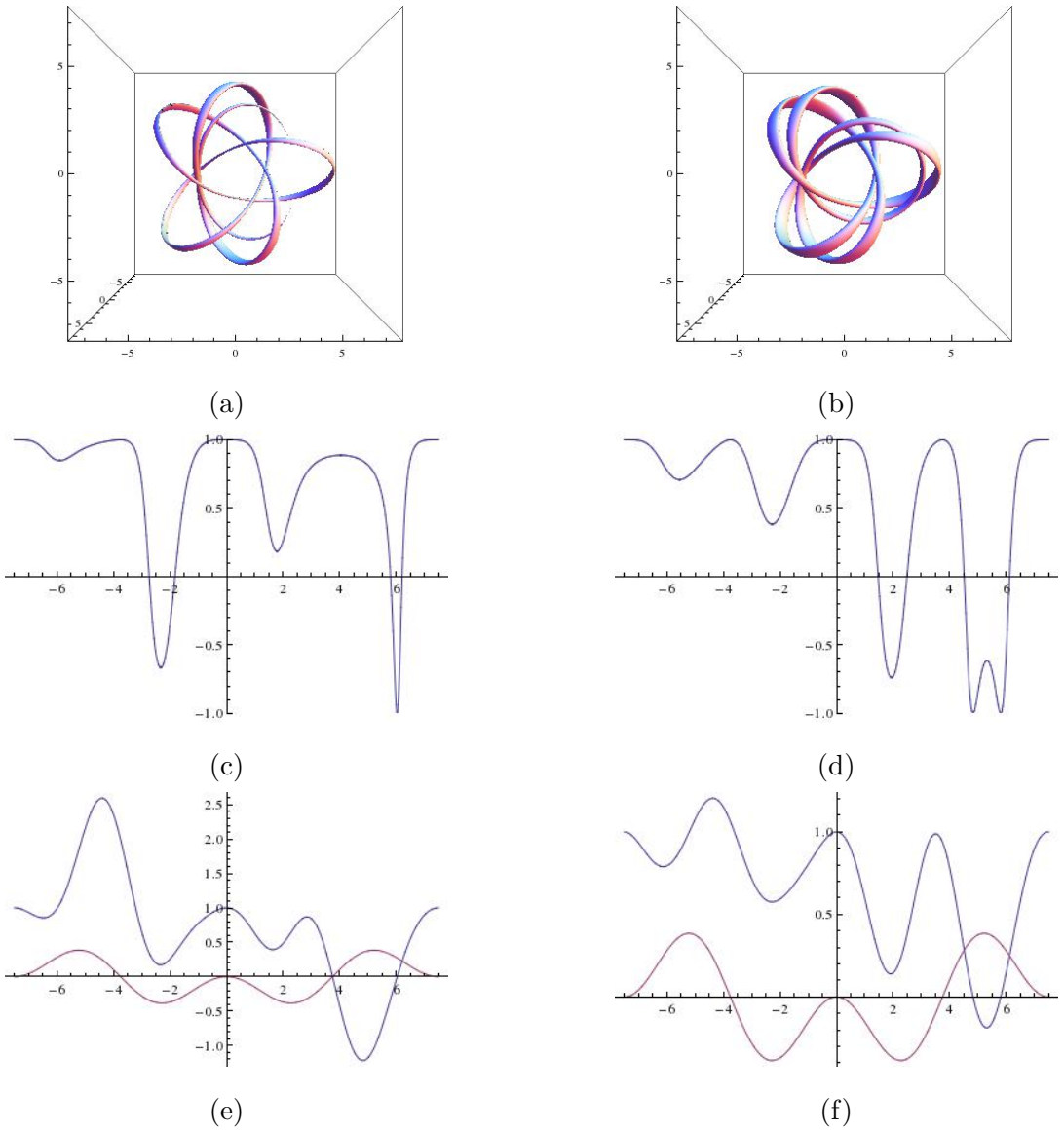

Figure 4.3: Various aspects of the initial field for different values of η demonstrating the pinching of the field. In the left column we have $\eta = 1$, while on the right we take $\eta = 1/2$. In (a) and (b) we plot an isosurface $\phi_3 = -0.8$ of the initial field generated from (4.2.13) for $\alpha = 2$, $\beta = 1$, $\gamma = 0$. We then restrict to the line $(x_1, 0, 0)$ and plot in (c) and (d) the field ϕ_3, and in (e) and (d) plot the numerator (red) and denominator (blue) of the rational map.

The constraint on integers m_i, n_i in (4.2.11) is stronger than we would wish for and results in the generation of more complex fields than we want to consider initially. We would like to find rational maps describing more simple cable knots. Consider the expansion

$$y = x^{3/2} + \eta x^{3/4}, \tag{4.2.14}$$

for non-zero $\eta \in \mathbb{C}$. This obviously does not satisfy the conditions on equation (4.2.11), so we need to consider the isomorphy condition again. Although in this case the tangent approaches a vector orthogonal to (x, y), since the origin of the four-ball is excluded, this does not forbid the isomorphy. We can explicitly check that it holds for $\xi > 1$. In this regime, an expansion in $1/\xi$ shows the leading behaviour is still given by $\mathcal{K}_{3,2}$, with the curve lying in a neighbourhood of this knot. Applying the same logic as above we see this gives a $\mathcal{C}^{2,3}_{3,2}$ knot. We find that $\xi = 1$ is again sufficient, so we find that

$$F(x, y) = y^4 - 2x^3y^2 - 4\eta^2x^3y + x^6 - \eta^4x^3 \tag{4.2.15}$$

and so a rational map which generates such a knotted field is given by

$$W = \frac{Z_1^\alpha Z_0^\beta (Z_1 - Z_0)^\gamma}{Z_0^4 - 2Z_1^3Z_0^2 - 4\eta^2 Z_1^3 Z_0 + Z_1^6 - \eta^4 Z_1^3}, \tag{4.2.16}$$

for α a non-negative integer, β a positive integer and $\gamma \in \{0, 1\}$. Similar arguments also hold for constructing fields with similar cable knot structure not satisfying the condition for (4.2.11). When m_2, n_2 are not coprime, one gets cable links. These can be constructed as the sum of two components each having the form of (possibly trivial) cable knots with m_2, n_2 not coprime, where they differ by a suitable shift in the complex parameter η. In the cases we consider we find that each link is a trefoil, but where the additional terms in each denominator result in the two components of the link winding about each other correctly. With this construction it is easier to fix the winding of each component independently. We discuss this in more detail in Appendix A.

Finally, before presenting the results of implementing such knotted fields as initial conditions, we wish to comment on the topological charge which rational maps (4.2.13) and (4.2.16) generate. Using the approach of counting the preimages of the

related mapping, as we did for the torus knot ansatz, one finds Z_1 must satisfy a polynomial equation of a particular degree. One might naïvely expect this to be the topological charge, however some of these polynomial roots scale inversely with $|\epsilon|$, and lie outside the unit ball so need to be excluded. This means that although the charge can be calculated for any given α, β and γ, finding a generic formula for the charge is complicated. The case for $\gamma = 0$ can be derived analytically by considering related maps in the same homotopy class such that the roots of the polynomials remain within/outside the four-ball[1]. Take rational map (4.2.16) for example and consider the roots of

$$(Z_1^\alpha Z_0^\beta, Z_0^4 - 2Z_1^3 Z_0^2 - 4s\eta^2 Z_1^3 Z_0 + Z_1^6 - s\eta^4 Z_1^3) \tag{4.2.17}$$

for $s \in [0, 1]$. We see that these have roots where $Z_1 = Z_0 = 0$ or $Z_0 = 0$ and $Z_1^3 = s\eta^4$. For $|\eta| < 1$ these roots lie within the four-ball. Thus we can take $s \to 0$. Now consider the mapping

$$(Z_1^\alpha Z_0^\beta, Z_0^4 - 2sZ_1^3 Z_0^2 + Z_1^6) \tag{4.2.18}$$

for $s \in [0, 1]$. All roots now occur at $Z_1 = Z_0 = 0$ and so we can again take $s \to 0$. Thus (4.2.16) with $\gamma = 0$ is in the same homotopy class as a particular torus knot, and so has charge $4\alpha + 6\beta$. Similar arguments are satisfied by (4.2.13) for $\gamma = 0$.

For $\gamma = 1$ we can consider a similar argument. Again using the example of (4.2.16), consider the roots of

$$(Z_1^\alpha Z_0^\beta (Z_1 - Z_0), Z_0^4 - 2Z_1^3 Z_0^2 - 4s\eta^2 Z_1^3 Z_0 + Z_1^6 - s\eta^4 Z_1^3) \tag{4.2.19}$$

for $s \in [0, 1]$. We see that these have roots where $Z_1 = Z_0 = 0$, $Z_0 = 0$ and $Z_1^3 = s\eta^4$ or $Z_1 = Z_0$ and $Z_1^3 - 2Z_1^2 + (1 - 4s\eta^2)Z_1 - s\eta^4 = 0$. For choices of η small enough, such that these roots remain inside/outside the three-sphere, we can then take $s \to 0$ and remain in the same homotopy class. Consider

$$(Z_1^\alpha Z_0^\beta (Z_1 - sZ_0), Z_0^4 - 2Z_1^3 Z_0^2 + Z_1^6) \tag{4.2.20}$$

[1]The author would like to thank Martin Speight for pointing out this argument for the calculation of Hopf charge for these mappings.

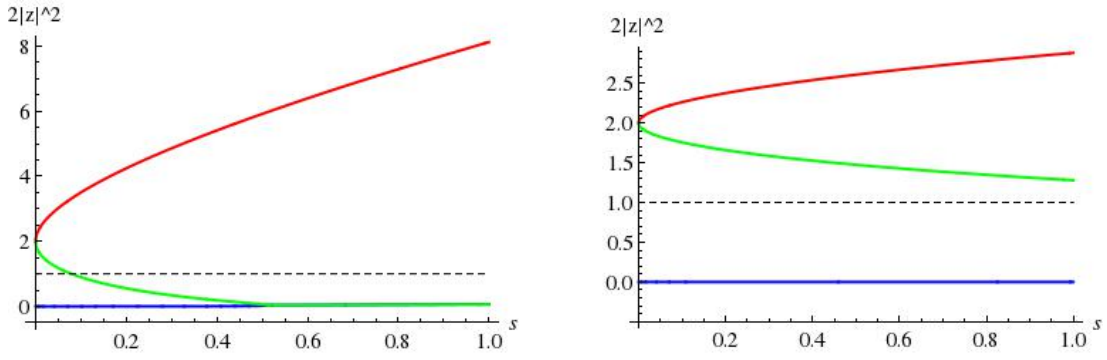

(a) $\eta = 0.5$ (b) $\eta = 0.1$

Figure 4.4: Plots of $2|z|^2$ for the roots to $z^3 - 2z^2 + (1 - 4s\eta^2)z - s\eta^4 = 0$ for $s \in [0, 1]$ for different values of η. Also marked is the value at which the root lies on the three-sphere.

for $s \in [0, 1]$. Roots now occur for $Z_1 = Z_0 = 0$ or $Z_1 = sZ_0$ and $1-2s^3Z_0+s^6Z_0^2 = 0$. These roots remain inside/outside the four-ball as $s \to 0$. Finally consider

$$(Z_1^{\alpha+1}Z_0^{\beta}, Z_0^4 - 2sZ_1^3Z_0^2 + Z_1^6) \tag{4.2.21}$$

for $s \in [0, 1]$. All roots lie at $Z_1 = Z_0 = 0$ and so can take $s \to 0$. Thus we again find that if our choice of η is sufficient, then (4.2.16) with $\gamma = 1$ is in the same homotopy class as a particular torus knot and so has charge $4(\alpha + 1) + 6\beta$. It remains to determine whether the choice of η is sufficiently small.

We find that our choice of $\eta = 1/2$ does not satisfy this condition. As can be seen in Figure 4.4(a) in such a limit one of the roots cross the boundary of the four-ball, and so the above argument does not hold. For a different choice of η which is small enough, as in Figure 4.4(b) where $\eta = 0.1$, this argument would hold. Instead we need to resort to numerically calculating the number of preimages within the four-ball. Similar results hold for $\gamma = 1$ for the other rational maps used and we need to resort to numerically calculating the number of preimages. The corresponding tables for the topological charges of given initial field configurations are shown in Appendix A.

4.3 Numerical Results

The numerical simulations have been carried out on a cubic grid with $(301)^3$ grid points and with lattice spacing $dx = 0.06$. Points on the edge of the grid are fixed to be $\boldsymbol{\phi}_\infty$. The energy of a given initial field as described in the previous sections is then minimised by the approach of [34]. The field is evolved according to field equations derived from the Skyrme-Faddeev Lagrange density (1.6.49), where only the second order kinetic terms from the sigma model term are considered. Whenever the potential energy of the system increases the kinetic energy is removed. This approach results in an algorithm which converges faster than standard gradient flow algorithms whilst avoiding the numerically costly matrix inversion which the complete dynamical field equations would entail. Limitations of the numerics also required us to scale W in some of the initial conditions so the field changes more smoothly.

We present our solutions by plotting an isosurface where $\phi_3 = -0.95$ which is the boundary of a tubular neighbourhood of the position of the soliton. We also plot a neighbourhood of a point close to the position curve to encapsulate the twisting of the field, and so enable us to see the Hopf charge as the linking number of these two curves. We choose this second point to be $\boldsymbol{\phi} = (\sqrt{2\mu - \mu^2}, 0, \mu - 1)$ for $\mu = 0.1$ and take an isosurface about this value. In some cases, the isosurface plotted interacts and makes it difficult to determine the form of the solution. In these cases to resolve the curve it was necessary to consider preimages of $\phi_3 = -1$ as the isoline where $\phi_1 = \phi_2 = 0$ where we restrict to field values on the southern hemisphere of the target S^2 to aid interpolation.

We now present the results for hopfions with topological charge sixteen to thirty–six. For each topological charge a range of initial field configurations are subjected to the energy minimisation scheme, and we record in Tables 4.1 and 4.2 the energy of configurations, along with a comparison to Ward's conjectured bound. We find that solutions for higher charges obey a similar growth in energy as found for lower charge solutions and in the other Skyrme-type models, exceeding Ward's bound by a little over 20%. Plots of solutions showing the location curve and curve showing twist can be found in Figures 4.5, 4.6, 4.7, 4.8 and 4.9.

Q	Initial $\to$ final	E	$E/Q^{3/4}$
16	$\mathcal{K}_{3,2}, \mathcal{K}_{5,3} \to \mathcal{K}_{5,3}$	9.887	1.236
	$\mathcal{K}_{5,4} \to \mathcal{L}^{4,4}_{4,4}$	9.904	1.238
	$\mathcal{L}^{2,2,2}_{4,3,3}, \mathcal{C}^{2,5}_{3,2}, \mathcal{C}^{2,7}_{3,2} \to \mathcal{L}^{3,3}_{8(3,2),2}$	9.919	1.240
	$\mathcal{C}^{2,3}_{3,2}, \mathcal{K}_{4,3} \to \mathcal{K}_{4,3}$	9.969	1.246
	$\mathcal{L}^{5,5}_{4(3,2),2(3,2)} \to \mathcal{L}^{4,4}_{5(3,2),3}$	10.057	1.257
	$\mathcal{K}_{5,2} \to \mathcal{L}^{3,3}_{7(3,2),3}$	10.165	1.271
17	$\mathcal{K}_{5,3}, \mathcal{K}_{7,3} \to \mathcal{L}^{3,3}_{8(3,2),3}$	10.355	1.237
	$\mathcal{K}_{4,3} \to \mathcal{L}^{3,3}_{9(3,2),2}$	10.422	1.245
	$\mathcal{C}^{2,5}_{3,2} \to \mathcal{L}^{3,3,3,3}_{2,1,1,1}$	10.424	1.245
	$\mathcal{C}^{2,3}_{3,2}, \mathcal{C}^{2,7}_{3,2}, \mathcal{K}_{5,4} \to \mathcal{L}^{4,3,3}_{5(3,2),1,1}$	10.487	1.253
	$\mathcal{K}_{7,2} \to \mathcal{K}_{7,2}$	10.952	1.308
18	$\mathcal{K}_{4,3}, \mathcal{K}_{5,3} \to \mathcal{K}_{5,3}$	10.821	1.238
	$\mathcal{C}^{2,3}_{3,2} \to \mathcal{L}^{4,3,3}_{6(3,2),1,1}$	10.832	1.240
	$\mathcal{C}^{2,5}_{3,2}, \mathcal{C}^{2,7}_{3,2}, \mathcal{K}_{5,4}$ $\mathcal{L}^{5,5}_{4(3,2),4(3,2)} \to \mathcal{L}^{3,3}_{11(5,2),1}$	10.835	1.240
	$\mathcal{K}_{7,2} \to \boldsymbol{\mathcal{H}_{4.851}}$	10.838	1.240
	$\mathcal{K}_{7,3} \to \mathcal{L}^{3,3}_{8(3,2),4}$	10.850	1.242
19	$\mathcal{C}^{2,5}_{3,2}, \mathcal{C}^{2,7}_{3,2} \to \mathcal{K}_{5,4}$	11.295	1.241
	$\mathcal{K}_{4,3}, \mathcal{K}_{5,3}, \mathcal{L}^{5,5}_{7(3,2),2(3,2)} \to \mathcal{K}_{5,3}$	11.311	1.243
	$\mathcal{K}_{5,4} \to \mathcal{L}^{4,3,3}_{6(3,2),2,1}$	11.315	1.243
	$\mathcal{C}^{2,3}_{3,2}, \mathcal{L}^{6,6}_{5(3,2),2(3,2)} \to \mathcal{L}^{4,4}_{7(3,2),4}$	11.322	1.245
	$\mathcal{K}_{7,3} \to \mathcal{K}_{7,3}$	11.427	1.256
	$\mathcal{K}_{7,2} \to \mathcal{K}_{7,2}$	12.008	1.319
20	$\mathcal{K}_{7,3} \to \mathcal{L}^{4,4,4}_{3,3,2}$	11.730	1.240
	$\mathcal{L}^{5,5}_{6(3,2),4(3,2)} \to \mathcal{K}_{5,4}$	11.753	1.243
	$\mathcal{C}^{2,3}_{3,2}, \mathcal{C}^{2,5}_{3,2}, \mathcal{C}^{2,7}_{3,2},$ $\mathcal{K}_{4,3}, \mathcal{L}^{6,6}_{4(3,2),4(3,2)} \to \mathcal{L}^{4,4,4}_{4,2,2}$	11.753	1.243
	$\mathcal{K}_{5,3} \to \mathcal{L}^{4,4}_{9(3,2),3}$	11.832	1.251
	$\mathcal{K}_{5,4} \to \mathcal{L}^{3,3,3,3}_{2,2,2,2}$	11.839	1.252
	$\mathcal{K}_{7,2} \to \mathcal{K}_{7,2}$	12.517	1.324

Q	Initial $\to$ final	E	$E/Q^{3/4}$
21	$\mathcal{C}^{2,3}_{3,2}, \mathcal{C}^{2,5}_{3,2}, \mathcal{C}^{2,7}_{3,2}, \mathcal{K}_{5,4} \to \mathcal{L}^{3,3}_{13(4,3),2}$	12.091	1.233
	$\mathcal{K}_{7,3} \to \mathcal{L}^{4,4,4}_{3,3,3}$	12.181	1.242
	$\mathcal{L}^{6,6}_{7(3,2),2(3,2)} \to \mathcal{L}^{4,4}_{11(5,2),2}$	12.250	1.249
	$\mathcal{K}_{5,3} \to \mathcal{K}_{5,3}$	12.271	1.251
	$\mathcal{K}_{7,2} \to \mathcal{K}_{7,2}$	13.075	1.333
22	$\mathcal{L}^{5,5}_{6(3,2),6(3,2)} \to \mathcal{L}^{4,3,3}_{8(3,2),2,2}$	12.446	1.225
	$\mathcal{K}_{5,4} \to \mathcal{K}_{5,4}$	12.455	1.226
	$\mathcal{C}^{2,3}_{3,2}, \mathcal{C}^{2,5}_{3,2}, \mathcal{C}^{2,7}_{3,2} \to \boldsymbol{\mathcal{C}^{2,3}_{3,2}}$	12.509	1.231
	$\mathcal{L}^{6,6}_{6(3,2),4(3,2)} \to \mathcal{L}^{5,4,3}_{7(3,2),2,1}$	12.655	1.246
	$\mathcal{K}_{7,3} \to \mathcal{L}^{4,4,4}_{4,3,2}$	12.663	1.247
	$\mathcal{K}_{5,3} \to \mathcal{L}^{4,4}_{9(3,2),5}$	12.883	1.268
	$\mathcal{K}_{7,2} \to \mathcal{K}_{7,2}$	13.696	1.348
23	$\mathcal{K}_{5,4} \to \mathcal{K}_{5,4}$	12.955	1.233
	$\mathcal{C}^{2,3}_{3,2}, \mathcal{C}^{2,5}_{3,2}, \mathcal{C}^{2,7}_{3,2} \to \boldsymbol{\mathcal{C}^{2,5}_{3,2}}$	12.959	1.234
	$\mathcal{L}^{5,5}_{9(3,2),4(3,2)} \to \mathcal{L}^{4,3,3}_{8(3,2),3,2}$	12.962	1.234
	$\mathcal{K}_{7,3} \to \mathcal{K}_{7,3}$	13.162	1.253
	$\mathcal{K}_{5,3} \to \mathcal{L}^{4,4}_{11(5,2),4}$	13.163	1.253
	$\mathcal{K}_{7,2} \to \mathcal{L}^{4,4}_{13(5,2),2}$	13.171	1.254
24	$\mathcal{C}^{2,3}_{3,2}, \mathcal{C}^{2,5}_{3,2}, \mathcal{C}^{2,7}_{3,2},$ $\mathcal{K}_{5,4}, \mathcal{L}^{5,5}_{9(3,2),5(3,2)}, \to \mathcal{L}^{6,6}_{6(3,2),6(3,2)}$ $\mathcal{L}^{6,6}_{6(3,2),6(3,2)}$	13.282	1.225
	$\mathcal{K}_{7,2} \to \mathcal{L}^{5,5}_{7(3,2),7(3,2)}$	13.284	1.225
	$\mathcal{K}_{5,3} \to \mathcal{L}^{3,3}_{17(5,3),1}$	13.439	1.239
	$\mathcal{K}_{7,3} \to \mathcal{L}^{6,6}_{8(3,2),4}$	13.628	1.257
25	$\mathcal{C}^{2,3}_{3,2}, \mathcal{C}^{2,5}_{3,2}, \mathcal{C}^{2,7}_{3,2} \to \mathcal{L}^{6,6}_{7(3,2),6(3,2)}$	13.752	1.230
	$\mathcal{K}_{5,4} \to \mathcal{K}_{5,4}$	13.811	1.235
	$\mathcal{L}^{5,5}_{9(3,2),6(3,2)} \to \mathcal{L}^{4,4}_{15(4,3),2}$	13.861	1.240
	$\mathcal{K}_{5,3}, \mathcal{K}_{7,3} \to \mathcal{K}_{7,3}$	14.026	1.255
	$\mathcal{K}_{7,2} \to \mathcal{L}^{5,5}_{11(5,2),4}$	14.112	1.262

Table 4.1: Initial field configurations and the form of the numerical solution and then the energy E and $E/Q^{3/4}$ for a comparison with Ward's conjectured bound for charges sixteen to twenty-five. Solutions not formed of torus knots are marked in bold.

Q	Initial $\rightarrow$ final	E	$E/Q^{3/4}$
26	$\mathcal{C}^{2,3}_{3,2}, \mathcal{C}^{2,5}_{3,2}, \mathcal{C}^{2,7}_{3,2} \rightarrow \mathcal{L}^{6,6}_{7(3,2),7(3,2)}$	14.057	1.221
	$\mathcal{K}_{5,4} \rightarrow \mathcal{L}^{6,6}_{8(3,2),6(3,2)}$	14.159	1.230
	$\mathcal{K}_{5,3}, \mathcal{K}_{7,3} \rightarrow \mathcal{K}_{7,3}$	14.490	1.258
	$\mathcal{K}_{7,2} \rightarrow \mathcal{L}^{4,4,4}_{6,4,4}$	14.697	1.276
27	$\mathcal{C}^{2,3}_{3,2}, \mathcal{C}^{2,5}_{3,2}, \mathcal{C}^{2,7}_{3,2} \rightarrow \boldsymbol{\mathcal{C}^{2,5}_{3,2}}$	14.578	1.231
	$\mathcal{K}_{7,2} \rightarrow \mathcal{L}^{6,6}_{9(3,2),6(3,2)}$	14.699	1.241
	$\mathcal{L}^{5,5}_{11(3,2),6(3,2)} \rightarrow \mathcal{L}^{6,6,4}_{6(3,2),3,2}$	14.711	1.242
	$\mathcal{K}_{5,4} \rightarrow \mathcal{L}^{4,4}_{17(4,3),2}$	14.743	1.245
	$\mathcal{K}_{7,3} \rightarrow \mathcal{L}^{5,5}_{14(5,2),3}$	14.948	1.262
	$\mathcal{K}_{5,3} \rightarrow \mathcal{L}^{5,5}_{13(5,2),4}$	14.977	1.264
28	$\mathcal{C}^{2,3}_{3,2}, \mathcal{C}^{2,5}_{3,2}, \mathcal{C}^{2,7}_{3,2}, \mathcal{L}^{5,5}_{9(3,2),9(3,2)} \rightarrow \boldsymbol{\mathcal{C}^{2,3}_{3,2}}$	14.878	1.222
	$\mathcal{K}_{5,4} \rightarrow \mathcal{L}^{6,4,4,4}_{4,2,2,2}$	15.023	1.234
	$\mathcal{K}_{5,3} \rightarrow \mathcal{L}^{6,5,5}_{6,3,3}$	15.198	1.249
	$\mathcal{K}_{7,2} \rightarrow \mathcal{K}_{8,3}$	15.382	1.264
	$\mathcal{K}_{7,3} \rightarrow \mathcal{K}_{7,3}$	15.420	1.267
29	$\mathcal{C}^{2,3}_{3,2}, \mathcal{C}^{2,5}_{3,2}, \mathcal{C}^{2,7}_{3,2} \rightarrow \mathcal{L}^{6,6}_{9(3,2),8(3,2)}$	15.396	1.232
	$\mathcal{K}_{5,3} \rightarrow \mathcal{L}^{5,5}_{17(5,3),2}$	15.399	1.232
	$\mathcal{K}_{5,4} \rightarrow \boldsymbol{\mathcal{C}^{2,7}_{3,2}}$	15.455	1.237
	$\mathcal{L}^{5,5}_{11(3,2),8(3,2)} \rightarrow \mathcal{L}^{6,6}_{13(4,3),4}$	15.478	1.239
	$\mathcal{K}_{7,2} \rightarrow \mathcal{K}_{8,3}$	15.852	1.268
	$\mathcal{K}_{7,3} \rightarrow \mathcal{L}^{6,5,5}_{5,4,4}$	15.988	1.279

Q	Initial $\rightarrow$ final	E	$E/Q^{3/4}$
30	$\mathcal{L}^{5,5}_{11(3,2),9(3,2)} \rightarrow \mathcal{L}^{5,5}_{18(5,3),2}$	15.713	1.226
	$\mathcal{C}^{2,3}_{3,2}, \mathcal{C}^{2,5}_{3,2}, \mathcal{C}^{2,7}_{3,2} \rightarrow \boldsymbol{\mathcal{C}^{2,5}_{3,2}}$	15.802	1.233
	$\mathcal{K}_{5,4} \rightarrow \boldsymbol{\mathcal{C}^{2,7}_{3,2}}$	15.851	1.237
31	$\mathcal{C}^{2,3}_{3,2}, \mathcal{C}^{2,5}_{3,2}, \mathcal{C}^{2,7}_{3,2}, \mathcal{L}^{5,5}_{13(3,2),8(3,2)} \rightarrow \boldsymbol{\mathcal{C}^{2,7}_{3,2}}$	16.294	1.240
	$\mathcal{K}_{5,4} \rightarrow \mathcal{L}^{6,6}_{15(4,3),4}$	16.319	1.242
32	$\mathcal{L}^{5,5}_{11(3,2),11(3,2)} \rightarrow \mathcal{L}^{6,6,5,5}_{3,3,2,2}$	16.516	1.228
	$\mathcal{K}_{5,4} \rightarrow \mathcal{L}^{6,4,4,4}_{8(3,2),2,2,2}$	16.523	1.228
	$\mathcal{C}^{2,3}_{3,2}, \mathcal{C}^{2,5}_{3,2}, \mathcal{C}^{2,7}_{3,2} \rightarrow \boldsymbol{\mathcal{C}^{2,5}_{3,2}}$	16.736	1.244
33	$\mathcal{C}^{2,3}_{3,2}, \mathcal{C}^{2,5}_{3,2} \rightarrow \mathcal{L}^{8,8}_{11(5,2),6(3,2)}$	16.925	1.229
	$\mathcal{C}^{2,7}_{3,2}, \mathcal{L}^{5,5}_{13(3,2),10(3,2)} \rightarrow \boldsymbol{\mathcal{H}_{3.609}}$	17.096	1.242
	$\mathcal{K}_{5,4} \rightarrow \mathcal{L}^{7,7,5,5}_{3,3,2,1}$	17.149	1.246
34	$\mathcal{K}_{5,4} \rightarrow \mathcal{L}^{6,6,5,5}_{4,4,2,2}$	17.334	1.231
	$\mathcal{L}^{5,5}_{13(3,2),11(3,2)} \rightarrow \boldsymbol{\mathcal{H}_{3.609}}$	17.368	1.234
	$\mathcal{C}^{2,3}_{3,2}, \mathcal{C}^{2,5}_{3,2}, \mathcal{C}^{2,7}_{3,2} \rightarrow \boldsymbol{\mathcal{C}^{2,3}_{3,2}}$	17.715	1.258
35	$\mathcal{K}_{5,4} \rightarrow \mathcal{L}^{8,8}_{13(4,3),6(3,2)}$	17.713	1.231
	$\mathcal{L}^{5,5}_{14(3,2),11(3,2)} \rightarrow \boldsymbol{\mathcal{H}_{3.609}}$	17.903	1.244
	$\mathcal{C}^{2,3}_{3,2}, \mathcal{C}^{2,5}_{3,2}, \mathcal{C}^{2,7}_{3,2} \rightarrow \mathcal{L}^{7,7}_{11(3,2),10(3,2)}$	18.331	1.274
36	$\mathcal{C}^{2,3}_{3,2}, \mathcal{C}^{2,7}_{3,2} \rightarrow \boldsymbol{\mathcal{L}^{4,4}_{26(2,3;3,2),2}}$	18.019	1.226
	$\mathcal{C}^{2,5}_{3,2} \rightarrow \boldsymbol{\mathcal{H}_{3.609}}$	18.178	1.237
	$\mathcal{K}_{5,4} \rightarrow \mathcal{L}^{8,5,5}_{15(4,3),2,1}$	18.275	1.243
	$\mathcal{L}^{5,5}_{13(3,2),13(3,2)} \rightarrow \boldsymbol{\mathcal{L}^{6,6}_{20\mathcal{H}_{2.828},4}}$	18.400	1.252

Table 4.2: Initial field configurations and the form of the numerical solution and then the energy E and $E/Q^{3/4}$ for a comparison with Ward's conjectured bound for charges twenty-six to thirty-six. Solutions not formed of torus knots are marked in bold.

For charges up to twenty-one we find that initial conditions which take the form of cable knots are unstable and result in fields resembling torus knots or links composed of torus knots with unknotted components. For this range of charge cable knot solutions are not expected since the charge due to the winding of the field is small – or even negative. However they give a complicated unstable initial field configurations and so provide a good starting condition to find energy minima. For each charge we find that there are a range of link solutions comprising a trefoil and an approximately axial hopfion with the charge shared between components in various ways. At charge sixteen we recover the solution $16\mathcal{L}^{2,2}_{8(3,2),2}$ first found in [34] (where it was denoted $\mathcal{X}_{16}$), and also find lower energy configurations $16\mathcal{K}_{5,3}$ and $16\mathcal{L}^{4,4}_{4,4}$. At charge seventeen we find a solution of the form $17\mathcal{L}^{3,3,3,3}_{2,1,1,1}$ which is the first known example of a four-component link in the model, however the torus link $17\mathcal{L}^{3,3}_{8(3,2),3}$ was the lowest energy configuration found. For charges eighteen and nineteen torus knot configurations were found to have the lowest energy, given by $18\mathcal{K}_{5,3}$ and $19\mathcal{K}_{5,4}$ respectively. The lowest energy configuration found for charge twenty is the link $20\mathcal{L}^{4,4,4}_{3,3,2}$, and for charge twenty-one the link $21\mathcal{L}^{3,3}_{13(4,3),2}$ has the lowest energy.

At charge twenty-two we find the first example of a hopfion with the field taking the form of a cable knot. We find that there is a local energy minimum of the form $22\mathcal{C}^{2,3}_{3,2}$ which exceeds the lowest energy solution found for that charge, a solution of the form $22\mathcal{L}^{4,3,3}_{8(3,2),2,2}$, by less than 1%. Similarly for charge twenty-three we again find a cable knot, this time it has the form of $23\mathcal{C}^{2,5}_{3,2}$ and is even closer to the lowest energy solution found, $23\mathcal{K}_{5,4}$. We find that for charges twenty-four to twenty-six the cable-knotted fields relax to resemble cable links, which are the minimal energy solutions found for these charges. These are the first examples known of solutions which are of the form of a link with two components being non-trivial torus knots. We then find that cable knots occur again for $27\mathcal{C}^{2,5}_{3,2}$, $28C^{2,3}_{3,2}$ and that this time they appear as the energy minimum found. For charge twenty-nine we again find a cable link being the minimal energy configuration, before finding local energy minima cable knots $30\mathcal{C}^{2,5}_{3,2}$, $31\mathcal{C}^{2,7}_{3,2}$, $32\mathcal{C}^{2,5}_{3,2}$ and $34\mathcal{C}^{2,3}_{3,2}$.

When one should expect cable knotted fields to appear in the theory seems to be a complicated question, with many possible factors influencing this such as the

twist of the field, the length and the self-interaction of strands. We note that for the cases of cable knots with odd charge we can see that the length of solutions appears longer than those with even charge. This can be understood since it is energetically favourable for the twisting about the core to align with a certain phase - as in the baby Skyrme model. We approximate the twist per unit length as constant, and the length to be approximately equal for each strand. The winding of the field can occur more smoothly with an odd number of twists for the cases we consider here, since the number of crossings is odd which corresponds to fields with even charge. When this lengthening of solutions becomes unfavourable we see a transition to cable links.

For some charges we find that the cable knotted initial fields relax to other structures. For charge thirty-six the lowest energy solution we have found is a link where one component is of the form of a charge twenty-six cable knot $\mathcal{C}^{2,3}_{3,2}$. We extend our notation for links to denote this $36\mathcal{L}^{4,4}_{26(2,3;3,2),2}$. For charge eighteen we find a local minimum of the energy which is the first known solution with the structure of a hyperbolic knot. One can use the SnapPy program [60] to calculate that it has hyperbolic volume 4.85117 and can identify it as knot 10_{139} in Rolfsen notation, or $k5_{22}$ in Callahan-Dean-Weeks-Champanerkar-Kofman-Patterson notation. We denote this by its hyperbolic volume as $\mathcal{H}_{4.851}$. For charges thirty-four to thirty-six we find further examples of knotted structures which take the form of hyperbolic knots. We see that for these charges the fields are knotted in the same way, and one can calculate that it has hyperbolic volume 3.60869 and can classify this knot as the knot $k4_4$. We therefore denote it as $\mathcal{H}_{3.609}$. Finally, we also find at charge thirty-six a link with one of the components being a hyperbolic knot. In this case we can identify it as the knot $k3_1$, which has hyperbolic volume 2.82812 and so denote the link as $\mathcal{L}^{6,6}_{20\mathcal{H}_{2.828},4}$.

4.4 Conclusion

In this chapter we have presented new rational maps which generate fields with a knotted structure of the form of cable knots. We have then also demonstrated that fields with such configurations are stable solutions in the Skyrme-Faddeev model

(a) $16\mathcal{K}_{5,3}$ (b) $16\mathcal{L}^{4,4}_{4,4}$ (c) $16\mathcal{L}^{3,3}_{8(3,2),2}$ (d) $16\mathcal{K}_{4,3}$

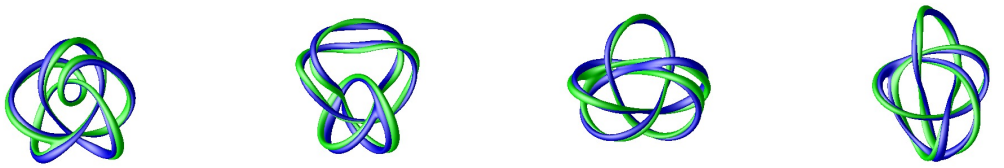

(e) $16\mathcal{L}^{4,4}_{5(3,2),3}$ (f) $16\mathcal{L}^{3,3}_{7(3,2),3}$ (g) $17\mathcal{L}^{3,3}_{8(3,2),3}$ (h) $17\mathcal{L}^{3,3}_{9(3,2),2}$

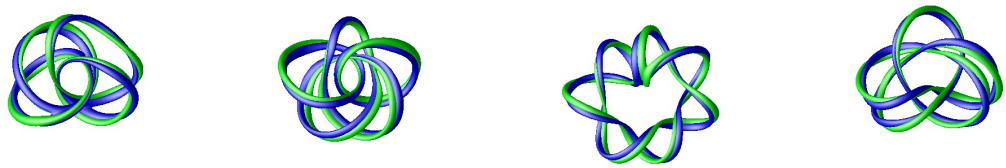

(i) $17\mathcal{L}^{3,3,3,3}_{2,1,1,1}$ (j) $17\mathcal{L}^{4,3,3}_{5(3,2),1,1}$ (k) $17\mathcal{K}_{7,2}$ (l) $18\mathcal{K}_{5,3}$

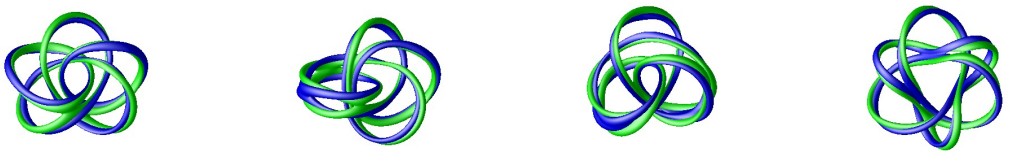

(m) $18\mathcal{L}^{4,3,3}_{6(3,2),1,1}$ (n) $18\mathcal{L}^{3,3}_{11(5,2),1}$ (o) $\mathbf{18\mathcal{H}_{4.851}}$ (p) $18\mathcal{L}^{3,3}_{8(3,2),4}$

Figure 4.5: The position curves (blue) and linking curve (green) for a range of solutions with topological charge $16 \leq Q \leq 18$. Solutions not formed of torus knots are marked in bold.

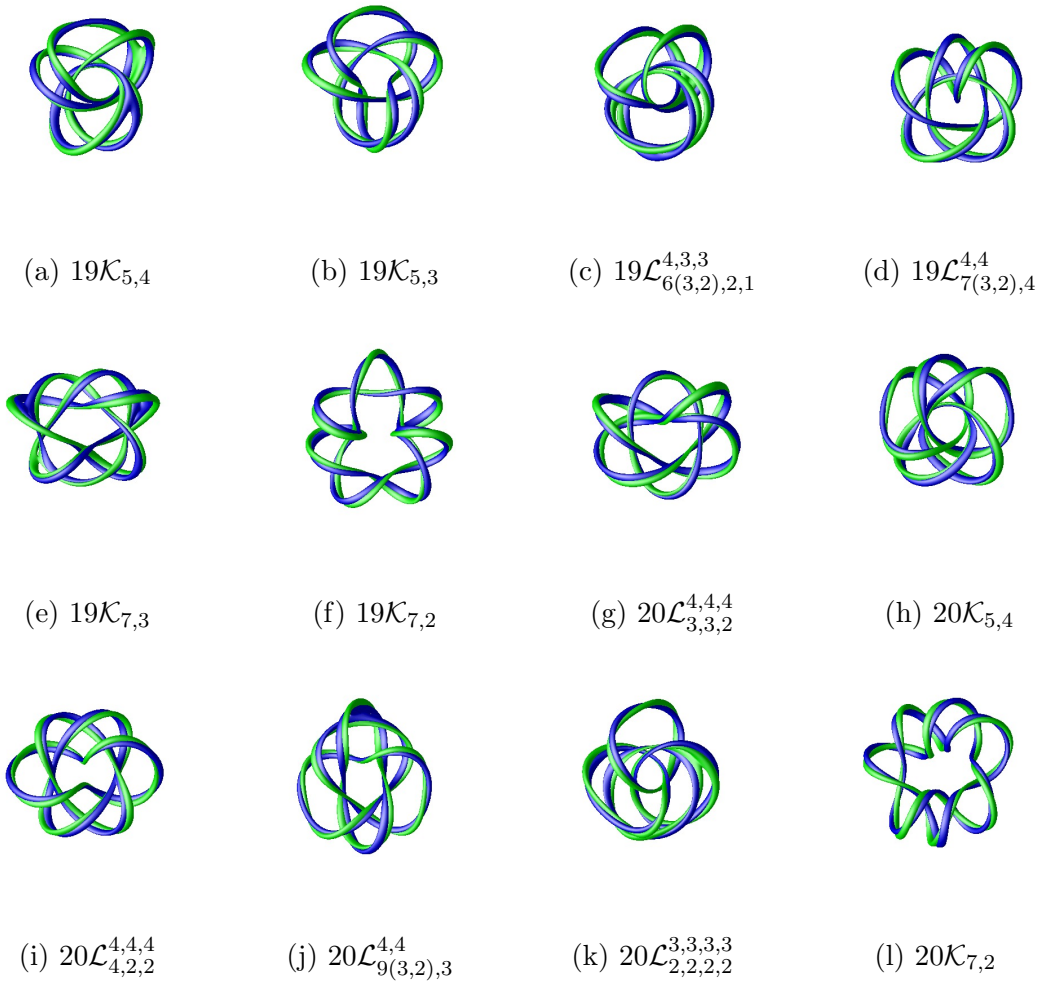

(a) $19\mathcal{K}_{5,4}$ (b) $19\mathcal{K}_{5,3}$ (c) $19\mathcal{L}^{4,3,3}_{6(3,2),2,1}$ (d) $19\mathcal{L}^{4,4}_{7(3,2),4}$

(e) $19\mathcal{K}_{7,3}$ (f) $19\mathcal{K}_{7,2}$ (g) $20\mathcal{L}^{4,4,4}_{3,3,2}$ (h) $20\mathcal{K}_{5,4}$

(i) $20\mathcal{L}^{4,4,4}_{4,2,2}$ (j) $20\mathcal{L}^{4,4}_{9(3,2),3}$ (k) $20\mathcal{L}^{3,3,3,3}_{2,2,2,2}$ (l) $20\mathcal{K}_{7,2}$

Figure 4.6: The position curves (blue) and linking curve (green) for a range of solutions with topological charge $19 \leq Q \leq 20$. Solutions not formed of torus knots are marked in bold.

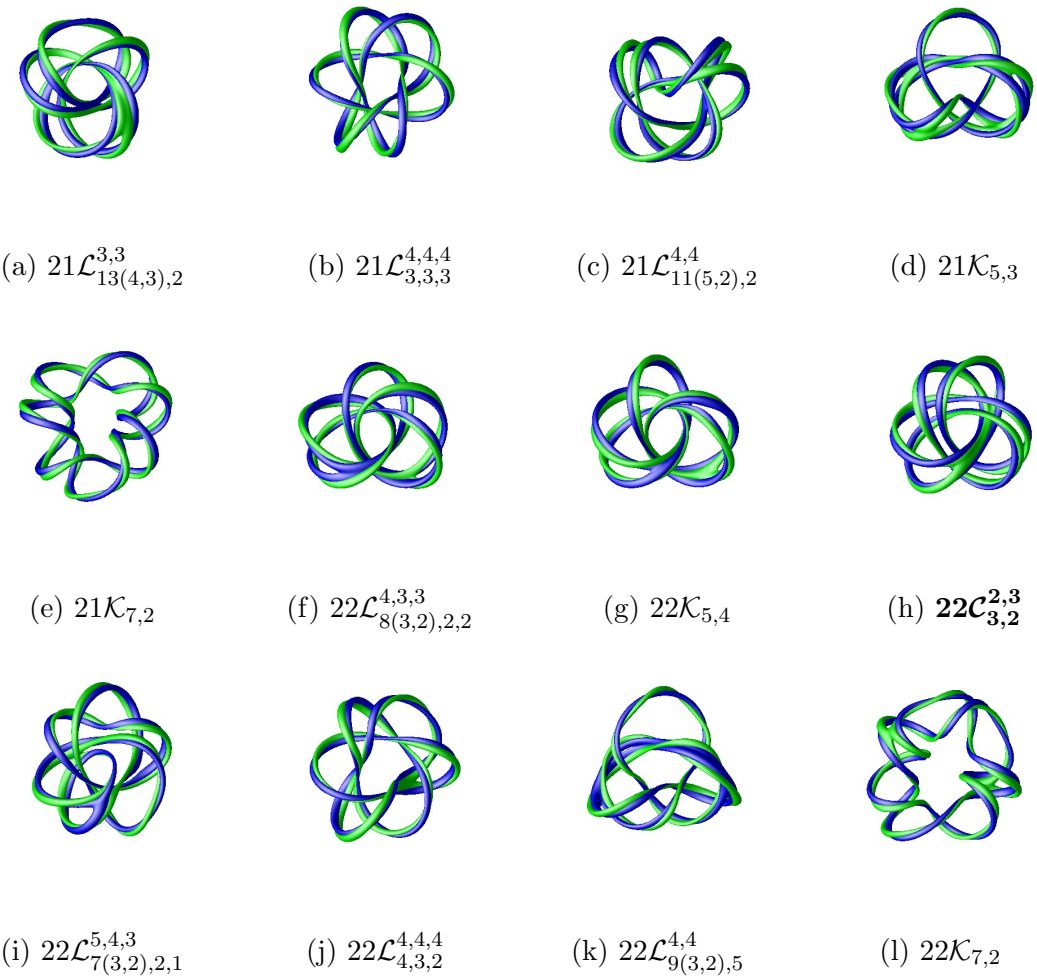

(a) $21\mathcal{L}^{3,3}_{13(4,3),2}$ (b) $21\mathcal{L}^{4,4,4}_{3,3,3}$ (c) $21\mathcal{L}^{4,4}_{11(5,2),2}$ (d) $21\mathcal{K}_{5,3}$

(e) $21\mathcal{K}_{7,2}$ (f) $22\mathcal{L}^{4,3,3}_{8(3,2),2,2}$ (g) $22\mathcal{K}_{5,4}$ (h) $\mathbf{22\mathcal{C}^{2,3}_{3,2}}$

(i) $22\mathcal{L}^{5,4,3}_{7(3,2),2,1}$ (j) $22\mathcal{L}^{4,4,4}_{4,3,2}$ (k) $22\mathcal{L}^{4,4}_{9(3,2),5}$ (l) $22\mathcal{K}_{7,2}$

Figure 4.7: The position curves (blue) and linking curve (green) for a range of solutions with topological charge $21 \leq Q \leq 22$. Solutions not formed of torus knots are marked in bold.

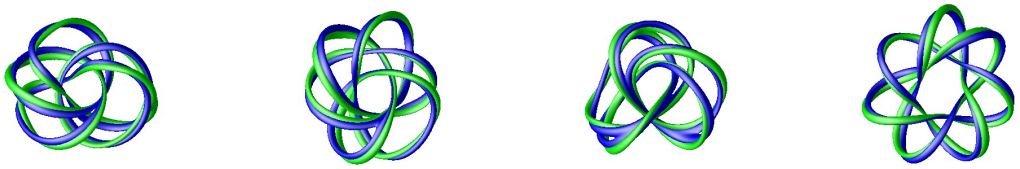

(a) $23\mathcal{K}_{5,4}$ (b) $\mathbf{23\mathcal{C}^{2,5}_{3,2}}$ (c) $23\mathcal{L}^{4,3,3}_{8(3,2),3,2}$ (d) $23\mathcal{K}_{7,3}$

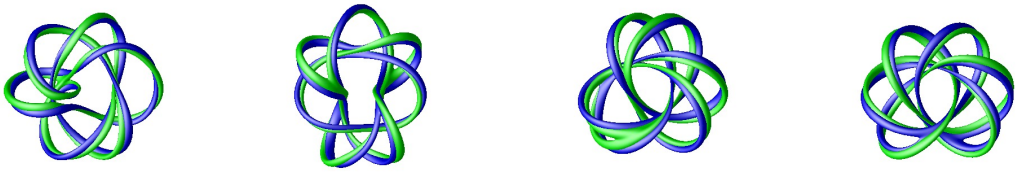

(e) $23\mathcal{L}^{4,4}_{11(5,2),4}$ (f) $23\mathcal{L}^{4,4}_{13(5,2),2}$ (g) $24\mathcal{L}^{6,6}_{6(3,2),6(3,2)}$ (h) $24\mathcal{L}^{5,5}_{7(3,2),7(3,2)}$

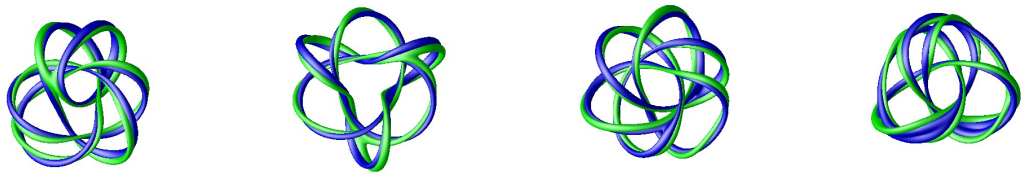

(i) $24\mathcal{L}^{3,3}_{17(5,3),1}$ (j) $24\mathcal{L}^{6,6}_{8(3,2),4}$ (k) $25\mathcal{L}^{6,6}_{7(3,2),6(3,2)}$ (l) $25\mathcal{K}_{5,4}$

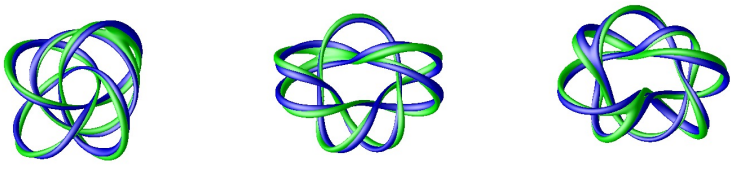

(m) $25\mathcal{L}^{4,4}_{15(4,3),2}$ (n) $25\mathcal{K}_{7,3}$ (o) $25\mathcal{L}^{5,5}_{11(5,2),4}$

Figure 4.8: The position curves (blue) and linking curve (green) for a range of solutions with topological charge $23 \leq Q \leq 25$. Solutions not formed of torus knots are marked in bold.

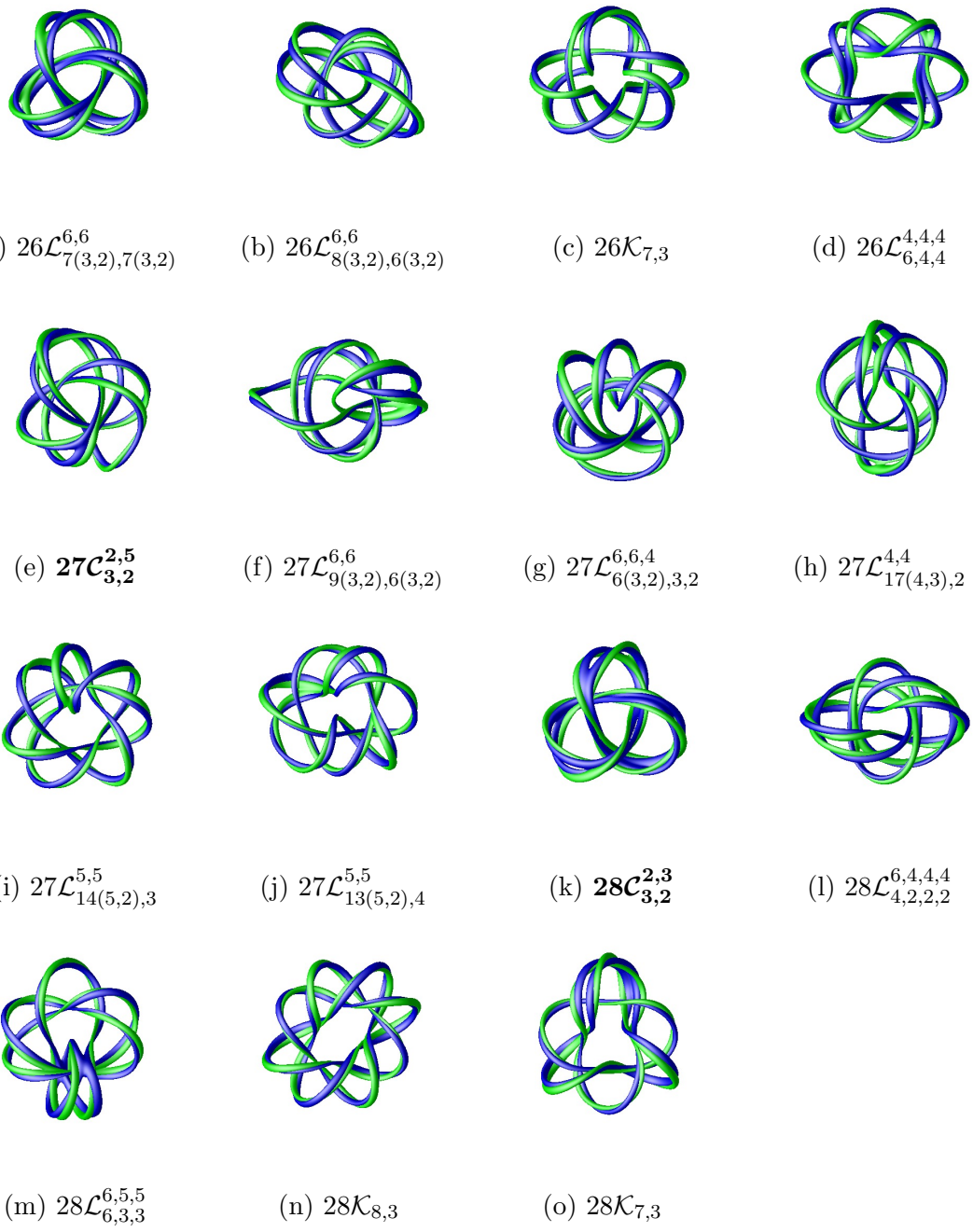

(a) $26\mathcal{L}^{6,6}_{7(3,2),7(3,2)}$ (b) $26\mathcal{L}^{6,6}_{8(3,2),6(3,2)}$ (c) $26\mathcal{K}_{7,3}$ (d) $26\mathcal{L}^{4,4,4}_{6,4,4}$

(e) $\mathbf{27\mathcal{C}^{2,5}_{3,2}}$ (f) $27\mathcal{L}^{6,6}_{9(3,2),6(3,2)}$ (g) $27\mathcal{L}^{6,6,4}_{6(3,2),3,2}$ (h) $27\mathcal{L}^{4,4}_{17(4,3),2}$

(i) $27\mathcal{L}^{5,5}_{14(5,2),3}$ (j) $27\mathcal{L}^{5,5}_{13(5,2),4}$ (k) $\mathbf{28\mathcal{C}^{2,3}_{3,2}}$ (l) $28\mathcal{L}^{6,4,4,4}_{4,2,2,2}$

(m) $28\mathcal{L}^{6,5,5}_{6,3,3}$ (n) $28\mathcal{K}_{8,3}$ (o) $28\mathcal{K}_{7,3}$

Figure 4.9: The position curves (blue) and linking curve (green) for a range of solutions with topological charge $26 \leq Q \leq 28$. Solutions not formed of torus knots are marked in bold.

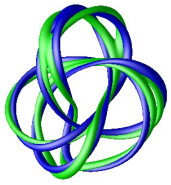

(a) $29\mathcal{L}^{6,6}_{9(3,2),8(3,2)}$

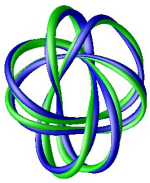

(b) $29\mathcal{L}^{5,5}_{17(5,3),2}$

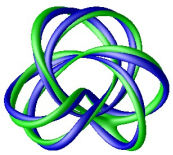

(c) $\mathbf{29\mathcal{C}^{2,7}_{3,2}}$

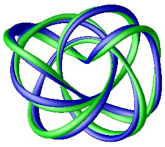

(d) $29\mathcal{L}^{6,6}_{13(4,3),4}$

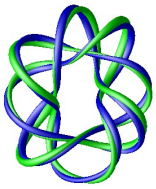

(e) $29\mathcal{K}_{8,3}$

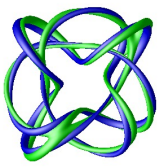

(f) $29\mathcal{L}^{6,5,5}_{5,4,4}$

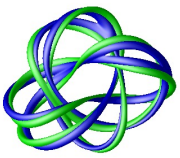

(g) $30\mathcal{L}^{5,5}_{18(5,3),2}$

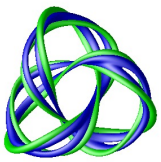

(h) $\mathbf{30\mathcal{C}^{2,5}_{3,2}}$

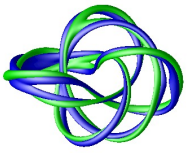

(i) $\mathbf{30\mathcal{C}^{2,7}_{3,2}}$

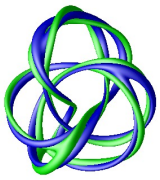

(j) $\mathbf{31\mathcal{C}^{2,7}_{3,2}}$

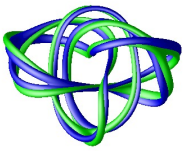

(k) $31\mathcal{L}^{6,6}_{15(4,3),4}$

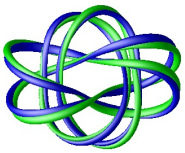

(l) $32\mathcal{L}^{6,6,5,5}_{3,3,2,2}$

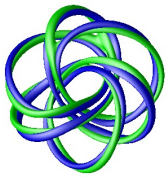

(m) $32\mathcal{L}^{6,4,4,4}_{8(3,2),2,2,2}$

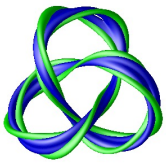

(n) $\mathbf{32\mathcal{C}^{2,5}_{3,2}}$

Figure 4.10: The position curves (blue) and linking curve (green) for a range of solutions with topological charge $29 \leq Q \leq 32$. Solutions not formed of torus knots are marked in bold.

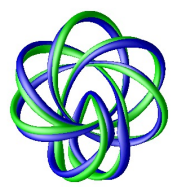

(a) $33\mathcal{L}^{8,8}_{11(5,2),6(3,2)}$

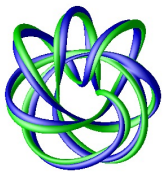

(b) $\mathbf{33\mathcal{H}_{3.609}}$

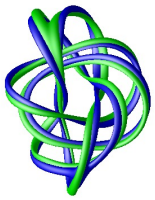

(c) $33\mathcal{L}^{7,7,5,5}_{3,3,2,1}$

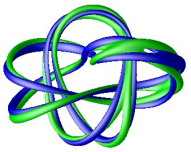

(d) $34\mathcal{L}^{6,6,5,5}_{4,4,2,2}$

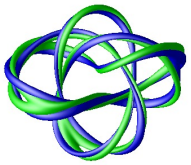

(e) $\mathbf{34\mathcal{H}_{3.609}}$

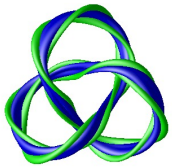

(f) $\mathbf{34\mathcal{C}^{2,3}_{3,2}}$

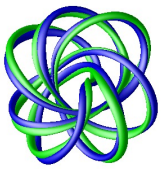

(g) $35\mathcal{L}^{8,8}_{13(4,3),6(3,2)}$

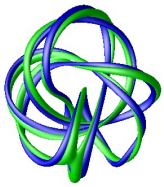

(h) $\mathbf{35\mathcal{H}_{3.609}}$

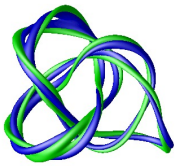

(i) $35\mathcal{L}^{7,7}_{11(3,2),10(3,2)}$

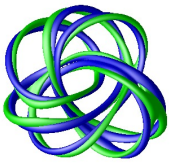

(j) $\mathbf{36\mathcal{L}^{4,4}_{26(2,3;3,2),2}}$

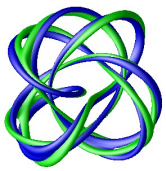

(k) $\mathbf{36\mathcal{H}_{3.609}}$

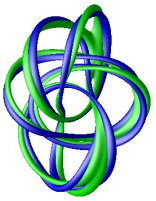

(l) $36\mathcal{L}^{8,5,5}_{15(4,3),2,1}$

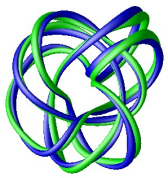

(m) $\mathbf{36\mathcal{L}^{6,6}_{20\mathcal{H}_{2.828},4}}$

Figure 4.11: The position curves (blue) and linking curve (green) for a range of solutions with topological charge $33 \leq Q \leq 36$. Solutions not formed of torus knots are marked in bold.

and in doing so have found the first known hopfions which are not of the form of torus knots. We have also found examples of the first known hyperbolic knots in the model. It has also been demonstrated that for higher charge solutions in the theory the energy continues to be in agreement with Ward's bound.

A number of different knotted structures have arisen in the model which would be interesting to explore further. In this current study hopfions taking the form of hyperbolic knots have arisen from an unstable ansatz of different structures. A rational map which generates a field of the form of hyperbolic knots would enable the study of these knots in more detail. We see that the first such case found in this study occurred at charge eighteen, and so would expect such hyperbolic knots to be present for relatively low charges. Cable knots themselves also have a natural extension, iterated torus knots, created by embedding these cable knots themselves on to a torus knot. It would be intriguing to see whether this iterated behaviour is something we can expect to occur in this model for large charge.

Similar knotted structures are also evident in a range of related models, such as the Nicole [61,62], Aratyn-Ferreira-Zimerman [63,64] and extended Skyrme-Faddeev [65] models. One would expect similarly knotted fields to appear as solutions in these models and it would be interesting to check whether these occur. The construction of knotted fields is used in a range of models in an analogous way to the Skyrme-Faddeev model, such as in knotted light fields [66], and so our construction might have applications in these situations.

Chapter 5

Hopfions as elastic rods

In this chapter we shall discuss some current work being undertaken. As we have seen in the previous chapter, the Skyrme-Faddeev model, given by static energy density (4.1.1) has static soliton solutions called hopfions which take the form of knotted and linked field solutions. These are classified by the topological charge, called the Hopf charge, associated with the homotopy group of maps $\pi_3(S^2) = \mathbb{Z}$. For more details on these static solutions we refer the reader to Chapter 4.

The solutions which we find in this theory exhibit features which are common in elastic rod theory. Firstly we note that solutions appear with tube-like position curves, as we see in plots. We also see that for low charge, we have axially symmetric solutions for Hopf charge one and two, as can be seen in the top row of Figure 5.2, however for charge three we see that the solution becomes buckled. Such buckling instabilities are well known in elastic rods and so motivated the study using elastic rods. Finally we note that simulations are numerically intensive in the full three-dimensional model and initial field conditions resembling certain knots are not always easy to find. These reasons motivated a study by Harland *et al.* [67] to derive an approximation to the Skyrme-Faddeev model using elastic rods. In this study the Skyrme-Faddeev solutions were compared with those of a related elastic rod model for charges up to seven. In this chapter we reproduce these elastic rod results and extend them up to charge twelve. We then apply the elastic rod model to a range of other knots to try and understand the characteristics which we would expect a knotted field in the Skyrme-Faddeev model to have. Where numerical val-

ues are mentioned in this chapter for the Skyrme-Faddeev model these have been implemented as detailed in Chapter 4, but with $(151)^3$ grid points for convenience.

5.1 The elastic rod model

Given the arclength parametrised centreline of a knot, $\mathbf{r}(s) \in \mathbb{R}^3$, we can define the Frenet frame of the curve. Denoting the derivative with respect to the arclength parameter by $'$, we define the tangent vector $\mathbf{T}(s) = \mathbf{r}'(s)$. The normal to the curve is given by $\mathbf{N}(s) = \mathbf{T}'(s)/|\mathbf{T}'(s)|$, and the curvature binormal by $\mathbf{B} = \mathbf{T} \times \mathbf{N}$. The Frenet frame is then the basis $\{\mathbf{T}, \mathbf{N}, \mathbf{B}\}$. The derivatives of these are given by

$$\begin{pmatrix} \mathbf{T}' \\ \mathbf{N}' \\ \mathbf{B}' \end{pmatrix} = \begin{pmatrix} 0 & \kappa & 0 \\ -\kappa & 0 & \tau \\ 0 & -\tau & 0 \end{pmatrix} \begin{pmatrix} \mathbf{T} \\ \mathbf{N} \\ \mathbf{B} \end{pmatrix}, \tag{5.1.1}$$

which defines the curvature $\kappa(s)$ and torsion $\tau(s)$ of the curve. We then consider a rod where the radius of the transverse disk is $1/\kappa(s)$. We can then define tubular coordinates of the rod $\{s, \rho, \theta\}$ related to $\mathbf{x} \in \mathbb{R}^3$ by

$$\mathbf{x} = \mathbf{r}(s) + \frac{\rho}{\kappa(s)} \left(\cos\theta \mathbf{N} + \sin\theta \mathbf{B}\right), \tag{5.1.2}$$

for ρ and θ polar coordinates of the unit disk. We also have a degree-one map from the transverse disk to S^2 via

$$\boldsymbol{\phi} = (\sin f \cos(\theta + \alpha), \sin f \sin(\theta + \alpha), \cos f), \tag{5.1.3}$$

for some twist function $\alpha(s)$ which satisfies $\alpha(L) = \alpha(0) + 2\pi m$ for some $m \in \mathbb{Z}$, and for $f(\rho)$ a monotonic function satisfying $f(0) = \pi$ and $f(1) = 0$. Outside this disk we set $\boldsymbol{\phi}$ as the vacuum. This then uniquely defines a field $\boldsymbol{\phi}$ for all points in $\mathbb{R}^3$ so long as there are no self-intersections of the tubular region. Recall that the static energy of the Skyrme-Faddeev model is of the form

$$E = \int \partial_i \boldsymbol{\phi} \cdot \partial_i \boldsymbol{\phi} + \frac{1}{2} (\partial_i \boldsymbol{\phi} \times \partial_j \boldsymbol{\phi}) \cdot (\partial_i \boldsymbol{\phi} \times \partial_j \boldsymbol{\phi}) \, d^3x. \tag{5.1.4}$$

One can show in a straight forward but lengthy calculation that in these tubular coordinates we have

$$\begin{aligned}\nabla = \frac{\mathbf{T}}{1-\rho\cos\theta}\partial_s + \kappa\left(\sin\theta\mathbf{B} + \cos\theta\mathbf{N} + \frac{\rho\kappa'\mathbf{T}}{\kappa^2(1-\rho\cos\theta}\right)\partial_\rho \\ +\frac{\kappa}{\rho}\left(\cos\theta\mathbf{B} - \sin\theta\mathbf{N} - \frac{\tau\rho\mathbf{T}}{\kappa(1-\rho\cos\theta)}\right)\partial_\theta\end{aligned} \tag{5.1.5}$$

Using this in the static energy and with the initial field given in (5.1.3) one can then find

$$E = \int_0^L \left\{ b_1 + c_1\kappa^2 + (\alpha' - \tau)^2\left(\frac{b_2}{\kappa^2} + c_2\right) + \frac{\kappa'^2}{\kappa^4}\left(b_3 + c_3\kappa^2\right)\right\} ds, \tag{5.1.6}$$

where constants b_i are derived from the sigma-model term and c_i from the Skyrme term. The particular form of these constants are given by

$$b_1 = \int \frac{1-\rho\cos\theta}{\rho}(f'^2\rho^2 + \sin^2 f)\,\mathrm{d}\rho\mathrm{d}\theta, \tag{5.1.7}$$

$$b_2 = \int \frac{\rho\sin^2 f}{1-\rho\cos\theta}\,\mathrm{d}\rho\mathrm{d}\theta, \tag{5.1.8}$$

$$b_3 = \int \frac{\rho^3 f'^2}{1-\rho\cos\theta}\,\mathrm{d}\rho\mathrm{d}\theta, \tag{5.1.9}$$

$$c_1 = \frac{1}{2}\int \frac{1}{\rho}(1-\rho\cos\theta)f'^2\sin^2 f\,\mathrm{d}\rho\,\mathrm{d}\theta, \tag{5.1.10}$$

$$c_2 = c_3 = \frac{1}{2}\int \frac{\rho f'^2\sin^2 f}{1-\rho\cos\theta}\,\mathrm{d}\rho\,\mathrm{d}\theta, \tag{5.1.11}$$

however the explicit form of these is not important in what follows. Following [67], a phenomenological approach is taken, and we consider the system where $b_2 = b_3 = c_3 = 0$. This removes terms which depend inversely of the curvature, as well as the derivatives of the curvature. Rescaling the energy and length scales gives us

$$E = \int_0^L \left\{1 + \kappa^2 + C(\alpha' - \tau)^2\right\} ds, \tag{5.1.12}$$

for some constant C. We note from the first term that the length of the rod is not fixed but is itself determined by energy minimisation. The constant C is constrained by considering when we wish the buckling of the axial rod to occur, and then by comparison of the ratio of energy and length between the charge one and charge two hopfions. To find where the elastic rod will buckle we consider Michell's buckling instability of the rod.

We now briefly explain the derivation of this instability as shown in [68]. We use the director basis $\{\mathbf{d}_1, \mathbf{d}_2, \mathbf{d}_3\}$ for the rod, which is related to the Frenet frame by a rotation

$$\begin{pmatrix} \mathbf{d}_1 \\ \mathbf{d}_2 \\ \mathbf{d}_3 \end{pmatrix} = \begin{pmatrix} 0 & \cos\chi & \sin\chi \\ 0 & -\sin\chi & \cos\chi \\ 1 & 0 & 0 \end{pmatrix} \begin{pmatrix} \mathbf{T} \\ \mathbf{N} \\ \mathbf{B} \end{pmatrix}, \tag{5.1.13}$$

thus it follows the frame evolves as $\mathbf{d}_i' = \mathbf{u} \times \mathbf{d}_i$ where $\mathbf{u} = (\kappa \sin\chi, \kappa\cos\chi, \tau + \chi')$ is the twist vector of the director frame. For a static rod which is naturally straight and with no body force, the force vector $\mathbf{n}$ and moment of force vector $\mathbf{m}$ obey

$$\mathbf{n}' = \mathbf{0}, \tag{5.1.14}$$

$$\mathbf{m}' + \mathbf{d}_3 \times \mathbf{n} = \mathbf{0} \tag{5.1.15}$$

which is closed by the constitutive relation

$$\mathbf{m} = \sum_{i=1}^{3} \frac{\partial W}{\partial u_i} \mathbf{d}_i, \tag{5.1.16}$$

where $W(\mathbf{u})$ is the strain-energy density. For energy given by (5.1.12) we see that we have strain-energy density

$$W(\mathbf{u}) = 1 + u_1^2 + u_2^2 + C u_3^2, \tag{5.1.17}$$

where the angle of the director basis is related to the twist rate as $\chi = -\alpha$. This gives us that

$$\mathbf{m} = 2\kappa\mathbf{B} + 2C\gamma\mathbf{T}, \tag{5.1.18}$$

where γ is the twist function associated to u_3. We note that since the elastic rod we are considering is isotropic we have that $W(\mathbf{u}) = W(0, \kappa, \tau + \chi')$. Using the moment of force vector $\mathbf{m}$, and solving for the force vector $\mathbf{n}$ using the static equations, one finds by resolving each component that the corresponding equations are

$$\gamma' = 0, \tag{5.1.19}$$

$$C\gamma\kappa' - \tau\kappa - 2\tau\kappa' = 0, \tag{5.1.20}$$

$$\kappa'''\kappa + \kappa^2(C\gamma - 2\tau)\tau' + \kappa'(\kappa^3 - \kappa'') = 0. \tag{5.1.21}$$

To identify where bifurcations may occur and an axial ring may lose stability with respect to out-of-plane and torsional deformations we consider small variations from the axial ring. We see from the first equation that the twist must be constant. We suppose the axial ring has curvature K and we know that an axial rod has no torsion. We thus take $\kappa = K + \epsilon\kappa_1$ and $\tau = \epsilon\tau_1$ and expand to first order in ϵ. These give

$$\epsilon C\gamma\kappa_1' - \epsilon\tau_1 K = 0 \tag{5.1.22}$$

$$K\epsilon\kappa_1''' + \epsilon K^2\tau_1' C\gamma + \epsilon\kappa_1' K^3 = 0 \tag{5.1.23}$$

We then find that these lead to

$$\kappa_1''' + (K^2 + C^2\gamma^2)\kappa_1' = 0. \tag{5.1.24}$$

If we restrict to periodic solutions of the form $\kappa_1 = \exp(insK)$ for some non-zero $n \in \mathbb{Z}$ we find we have a solution if $n^2K^2 = K^2 + C^2\gamma^2$, or rearranging for

$$n^2 - 1 = C^2\gamma^2 K^{-2}, \tag{5.1.25}$$

which has the first non-trivial solutions for $n = 2$, in which case we find that

$$\gamma = \sqrt{3}K/C. \tag{5.1.26}$$

Since the charge of an axial rod is the total twist of the rod, we have that $2\pi Q = 2\pi\gamma/K$. Thus we find that the circular ring will buckle for charge Q satisfying

$$Q > \frac{\sqrt{3}}{C}, \tag{5.1.27}$$

which occurs first for $Q = 3$ if $\frac{1}{\sqrt{3}} < C < \frac{\sqrt{3}}{2}$. This fixes C to lie within a particular range, however to set C to be a specific value we compare the energy these give to those found in the Skyrme-Faddeev model.

For axially symmetric solutions of length L we find curvature $\kappa = 2\pi/L$ and torsion $\tau = 0$. We can then take the twist function to be linear, $\alpha = 2\pi Qs/L$. Substituting these in to energy (5.1.12) and integrating we find that

$$E = L + \frac{4\pi^2}{L} + \frac{4\pi^2 CQ^2}{L}, \tag{5.1.28}$$

which we can then minimise to find the energy and length of axial rod solutions in the model. We find that for an axial rod

$$E_Q^{\bigcirc} = 4\pi\sqrt{1+CQ^2} \tag{5.1.29}$$

when it has length

$$L_Q^{\bigcirc} = 2\pi\sqrt{1+CQ^2}. \tag{5.1.30}$$

By comparing these values with the full numerical simulations it was found that since the elastic rod approximation underestimates the soliton energy from the twisting of the rod, a higher value of C makes these closer to those seen in the full model. We therefore follow Harland *et al.* [67] and choose to set $C = 0.85$. Comparing with the full numerical model we find that this gives us $E_2^{\bigcirc}/E_1^{\bigcirc} = L_2^{\bigcirc}/L_1^{\bigcirc} = 1.54$ compared with $E_2^{SF}/E_1^{SF} = 1.63$ and $L_2^{SF}/L_1^{SF} = 1.45$, and so agrees to within 6%. Thus we see that $1\mathcal{A}_{1,1}$ has energy $E_1^{\bigcirc} = 17.09$ and $2\mathcal{A}_{2,1}$ has energy $E_2^{\bigcirc} = 26.36$.

We know from the considerations of the Michell instability that for charge three and above buckling occurs and we no longer have analytic solutions. Instead we must resort to numerical methods. Also an additional constraint needs to be included in our considerations to ensure that the elastic rod does not self-intersect, since we know that the approximation breaks down at this point. We start by making an additional approximation that the rod is of constant thickness R. For this additional constraint to not affect the previous results mentioned, we know that the thickness of the rod must satisfy $2\pi R \leq L_1^{\bigcirc}$. As we mentioned before it is found that the elastic rod model underestimates the energy of the full model, so we maximise the rod energy by choosing R as the upper limit of this, so $R = 1.36$.

For winding number greater than three the solution buckles and the analytical study breaks down. However, as we know that links occur frequently in the Skyrme-Faddeev model we can consider links formed of components with charges one and two, which can be considered analytically. For these components to be links they must have a radius large enough such that it can be linked to the other component. This means that we find charge one and two components must satisfy $L_Q^{\odot} \geq 4\pi R$ and the energy is least when this bound is saturated. Using this in equation (5.1.28)

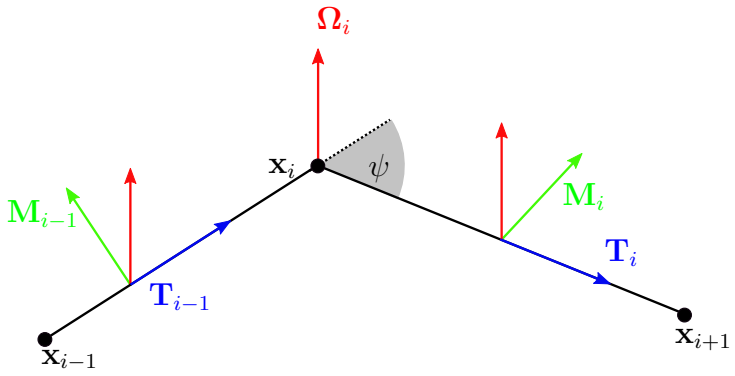

Figure 5.1: A sketch of a section of the discretised curve, showing points $\mathbf{x}_i$, the associated unit tangent vectors $\mathbf{T}_i$, material vectors $\mathbf{M}_i$ and the curvature binormal vector $\mathbf{\Omega}_i$. We also show the rotation angle ψ about the curvature binormal vector which corresponds to parallel transport along the discretised curve.

it follows

$$E_Q^{\odot} = \frac{\pi}{R}\left(4R^2 + 1 + CQ^2\right) \tag{5.1.31}$$

So for solutions formed of axial links we find the energy analytically. The energy of $4\mathcal{L}^{1,1}_{1,1}$ is given by $2E_1^{\odot} = 42.73$, while for $5\mathcal{L}^{1,1}_{2,1}$ is given by $E_1^{\odot} + E_2^{\odot} = 48.62$. Finally $6\mathcal{L}^{1,1}_{2,2}$ can be found to have energy $2E_2^{\odot} = 54.51$.

5.2 Numerical results

In this section we discuss the numerical methods used to find solutions to the elastic rod model we are considering for non-axial rods. The methods used and described in this study have been considered in detail in [69]. Firstly we discretise the curve so that it is described by $n+1$ points $\{\mathbf{x}_0 \cdots \mathbf{x}_n\}$. We then define straight edges between these as points $\mathbf{e}_i = \mathbf{x}_{i+1} - \mathbf{x}_i$, with $\mathbf{x}_{n+1}$ identified with $\mathbf{x}_0$. We then can also introduce tangent vectors associated to each edge of the curve $\mathbf{T}_i = \mathbf{e}_i/|\mathbf{e}_i|$. Define the curvature in terms of the curvature binormal vector

$$\mathbf{\Omega}_i = (\kappa \mathbf{B})_i = \frac{2\mathbf{e}_{i-1} \times \mathbf{e}_i}{|\mathbf{e}_{i-1}||\mathbf{e}_i| + \mathbf{e}_{i-1} \cdot \mathbf{e}_i}. \tag{5.2.32}$$

We see that the curvature associated to vertex $\mathbf{x}_i$ is just the magnitude of the curvature binormal vector, so $\kappa_i^2 = |\mathbf{\Omega}_i|^2$.

We also need to describe the twist of the rod. To do this we introduce a material unit vector $\mathbf{M}_i$ associated to each tangent vector $\mathbf{T}_i$ such that $\mathbf{M}_i \cdot \mathbf{T}_i = 0$. We see that the curvature binormal vector is also orthogonal to $\mathbf{T}_i$ and so we have an orthonormal basis $\{\mathbf{T}_i, \mathbf{\Omega}_i/\kappa_i, \mathbf{T}_i \times \mathbf{\Omega}_i/\kappa_i\}$. Since the curvature binormal is also orthogonal to $\mathbf{T}_{i-1}$ we can use it to define a similar orthogonal basis for this point with $\mathbf{T}_{i-1}$. Thus we can use the material vector to define angle θ_i by

$$\mathbf{M}_i = \frac{1}{\kappa_i}\left(\cos(\theta_i)\mathbf{\Omega}_i + \sin(\theta_i)\mathbf{T}_i \times \mathbf{\Omega}_i\right) \tag{5.2.33}$$

and similarly define θ_{i-1} as

$$\mathbf{M}_{i-1} = \frac{1}{\kappa_i}\left(\cos(\theta_{i-1})\mathbf{\Omega}_i + \sin(\theta_{i-1})\mathbf{T}_{i-1} \times \mathbf{\Omega}_i\right). \tag{5.2.34}$$

Then it follows that the discretised twist rate $\gamma_i = \theta_i - \theta_{i-1}$ of the material vector is given by

$$\sin(\gamma_i) = \kappa_i^{-2}\left[(\mathbf{M}_{i-1} \cdot \mathbf{T}_{i-1} \times \mathbf{\Omega}_i)(\mathbf{\Omega}_i \cdot \mathbf{M}_i) - (\mathbf{M}_i \cdot \mathbf{T}_i \times \mathbf{\Omega}_i)(\mathbf{\Omega}_i \cdot \mathbf{M}_{i-1})\right] \tag{5.2.35}$$

We then note that since κ_i and γ_i defined above are integrated quantities along the section of the curve that they relate to, we then need to divide each by $(|\mathbf{e}_{i-1}| + |\mathbf{e}_i|)/2$ to get a point-wise one. We thus find that the discretised energy is given by

$$E = \sum_{i=0}^{n}\left\{|\mathbf{e}_i| + \frac{2(\kappa_i^2 + C\gamma_i^2)}{|\mathbf{e}_{i-1}| + |\mathbf{e}_i|}\right\}, \tag{5.2.36}$$

where we have simplifed the first term of the summation by using that we have identified $\mathbf{x}_{n+1}$ and $\mathbf{x}_0$.

It is known [70] that for this thickened rod to not self-intersect we require for $\kappa(s) \leq 1/R$ and that $R \leq \frac{1}{2}\min\mathcal{I}$ where

$$\mathcal{I} = \{|\mathbf{r}(s) - \mathbf{r}(s')| : s \neq s', (\mathbf{r}(s) - \mathbf{r}(s')) \cdot \mathbf{T}(s) = 0 = (\mathbf{r}(s) - \mathbf{r}(s')) \cdot \mathbf{T}(s')\}. \tag{5.2.37}$$

The first of these conditions ensures that the elastic rod cannot bend to the extent that it intersects with itself, while the second prevents points from different sections

of the curve becoming too close that they would intersect. These conditions can be discretised to give the following two conditions [71]. Firstly we require that

$$\frac{2\kappa_i}{|\mathbf{e}_{i-1}| + |\mathbf{e}_i|} \leq 1/R \tag{5.2.38}$$

for all i, and secondly require that $R \leq \frac{1}{2}\min \mathcal{I}_D$ where $\mathcal{I}_D$ is now the discretised set

$$\mathcal{I}_D = \{|\mathbf{x}_i - \mathbf{x}_j| : \mathbf{x}_i \neq \mathbf{x}_j \text{ turning points of } |\mathbf{x} - \mathbf{x}_i| \text{ and } |\mathbf{x} - \mathbf{x}_j| \text{ respectively}\} \tag{5.2.39}$$

where we call $\mathbf{x}_i$ a turning point of $|\mathbf{x} - \mathbf{x}_j|$ if the distance goes from increasing to decreasing or visa versa as points along the along curve are considered. That is, $\mathbf{x}_i$ a turning point if $|\mathbf{x}_i - \mathbf{x}_j| > |\mathbf{x}_{i-1} - \mathbf{x}_j|$ and $|\mathbf{x}_{i-1} - \mathbf{x}_j| < |\mathbf{x}_{i-2} - \mathbf{x}_j|$, or if $|\mathbf{x}_i - \mathbf{x}_j| < |\mathbf{x}_{i-1} - \mathbf{x}_j|$ and $|\mathbf{x}_{i-1} - \mathbf{x}_j| > |\mathbf{x}_{i-2} - \mathbf{x}_j|$. It has been shown that these conditions tend toward the corresponding continuous conditions as the number of points in the discretisation increases [72, 73]. Finally we also need to maintain these points equally distributed along the curve. To do this we introduce a penalty function which penalises the length between points being unequal.

In this current study the curve is discretised with $n = 100$ and the energy is minimised using a simulated annealing method. Given an initial curve a point is chosen at random and a proposed change is either accepted or rejected with a probability depending on the energy difference and the temperature of the system. This temperature is then gradually reduced to give the energy minimum. We have completed studies of these numerical methods for the cases where we have analytic solutions and find that our numerical methods agree with the energy and length found there with an error of less than 1%. We have repeated results for the model for charges up to seven as first undertaken in [67] and extended this for higher charges. A selection of our results are shown in Figures 5.2, 5.3 and 5.4 where we have plotted the rod in blue, with radius $R/2$ to aid visualisation, and the material vector is indicated in green. The energies found are presented in Table 5.1 where they are normalised against the unit charge solution.

For charge three we see that the solution buckles, as we expect from the choice of C and our analysis of Michell's instability. For charge four we see that we are

unable to reproduce the type of solution found in the Skyrme-Faddeev model, where a solution of the form $4\mathcal{A}_{2,2}$ is found. This can either be thought of as two charge one solutions on top of each other or as having a cross-section formed from a charge two baby Skyrmion. Both of these identifications however cannot be realised in the elastic rod model since these are either not of the form of the ansatz (5.1.3) or would need the elastic rods to overlap which is not possible in the model. We do however find the linked solution $4\mathcal{L}^{1,1}_{1,1}$ analytically as described above. A solution of this form is not found in the Skyrme-Faddeev model but since the elastic rod is unable to cross there are such cases which need to be considered. At charge seven we see that the trefoil knotted solution has the lowest energy of all the forms which are considered. We see that this transition occurs exactly as we would wish for it to in comparison with the Skyrme-Faddeev model.

For charges above seven, beyond those studied in [67], we see that the elastic rod model is not so accurate at predicting the order of the energies which solutions have. We expect this is due to the neglected terms in the model beginning to have an effect. However, the energy values of the possible solutions found which relate to the Skyrme-Faddeev model are vaguely of a similar range of energy values for a given charge, whilst solutions which are not seen in the Skyrme-Faddeev model are of higher energy. Therefore, although we are not able to predict accurately the minimal energy solution, the elastic rod model will still provide us with a useful way to determine whether a particular knot occurring is feasible for a given charge. For example, we see that the energy for $10\mathcal{K}_{4,3}$ and $11\mathcal{K}_{4,3}$ is much greater than the other possibilities, and from our knowledge of the Skyrme-Faddeev model we know this is indeed the case, since such solutions have not been found.

5.3 A search for non-torus knots

As we detailed in the previous chapter, it has been recently shown that non-torus knots can occur in the Skyrme-Faddeev model, with cable knots and hyperbolic knots having been found. A large number of knots are known to exist for a relatively low number of crossings, for example, there are two hundred and fifty prime knots

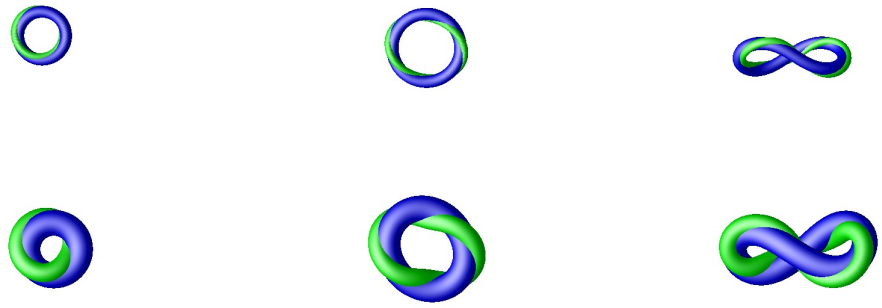

Figure 5.2: Solutions for charges one to three for the Skyrme-Faddeev model (top) and the elastic rod approximation (bottom). Note that the approximation captures the buckling of the charge three solution.

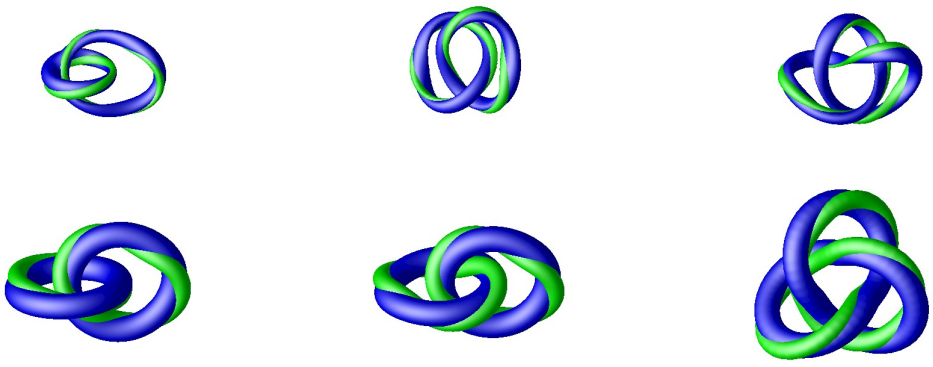

Figure 5.3: Solutions for charges five to seven for the Skyrme-Faddeev model (top) and the elastic rod approximation (bottom). Note that the model also captures the link solutions and the trefoil solution.

Type	E_N^{SF}	E_N^{ER}
$1\mathcal{A}_{1,1}$	1.0	1.0
$2\mathcal{A}_{2,1}$	1.63	1.54
$3\mathcal{A}_{3,1}$	2.28	2.06
$4\mathcal{L}_{1,1}^{1,1}$	-	2.50
$4\mathcal{A}_{2,2}$	2.86	-
$5\mathcal{L}_{2,1}^{1,1}$	3.43	2.84
$5\mathcal{K}_{3,2}$	-	3.08
$5A_{5,1}$	-	3.09
$6\mathcal{L}_{2,2}^{1,1}$	3.85	3.19
$6\mathcal{K}_{3,2}$	-	3.27
$6A_{6,1}$	-	3.61
$7\mathcal{K}_{3,2}$	4.35	3.54
$7\mathcal{L}_{2,3}^{1,1}$	-	3.75

Type	E_N^{SF}	E_N^{ER}
$8\mathcal{K}_{3,2}$	4.86	3.89
$8\mathcal{L}_{2,4}^{1,1}$	-	4.26
$8\mathcal{L}_{2,2}^{2,2}$	-	4.26
$8\mathcal{L}_{3,3}^{1,1}$	4.83	4.32
$8\mathcal{K}_{5,2}$	-	4.41
$9\mathcal{L}_{2,3}^{2,2}$	-	4.28
$9\mathcal{K}_{3,2}$	5.30	4.34
$9\mathcal{K}_{5,2}$	-	4.52
$9\mathcal{L}_{1,1,1}^{2,2,2}$	5.29	4.70
$9\mathcal{L}_{3,4}^{1,1}$	-	4.83
$10\mathcal{K}_{5,2}$	-	4.72
$10\mathcal{L}_{3,3}^{2,2}$	5.82	4.81
$10\mathcal{K}_{3,2}$	5.84	4.86

Type	E_N^{SF}	E_N^{ER}
$10\mathcal{L}_{1,1,2}^{2,2,2}$	5.72	4.94
$10\mathcal{K}_{4,3}$	-	5.30
$11\mathcal{K}_{5,2}$	6.22	4.97
$11\mathcal{L}_{3,4}^{2,2}$	6.20	5.01
$11\mathcal{L}_{1,2,2}^{2,2,2}$	6.13	5.20
$11\mathcal{K}_{3,2}$	6.31	5.39
$11\mathcal{K}_{4,3}$	-	5.39
$12\mathcal{K}_{5,2}$	6.67	5.30
$12\mathcal{L}_{2,2,2}^{2,2,2}$	6.50	5.44
$12\mathcal{K}_{4,3}$	6.48	5.54
$12\mathcal{L}_{4,4}^{2,2}$	-	5.56
$12\mathcal{K}_{7,2}$	-	5.78
$12\mathcal{K}_{3,2}$	6.66	5.93

Table 5.1: Table comparing energies in the Skyrme-Faddeev model and the elastic rod approximation, each normalised against the energy for the $\mathcal{A}_{1,1}$ solution.

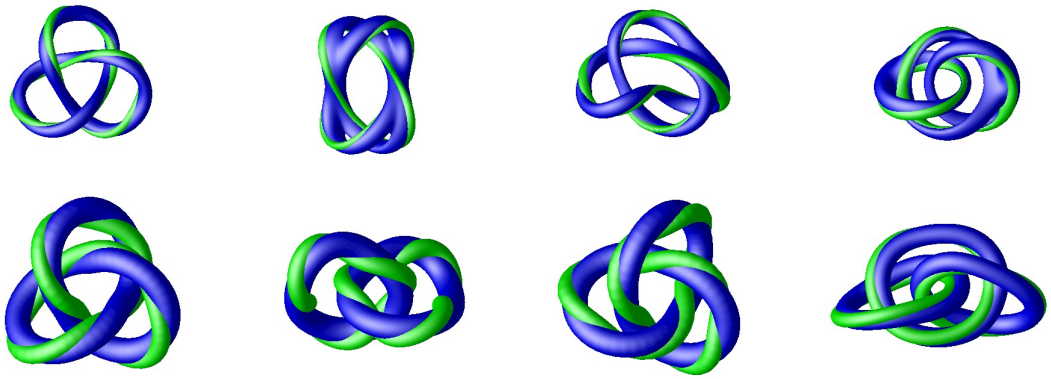

Figure 5.4: Solutions for charges eight and nine for the Skyrme-Faddeev model (top) and the corresponding elastic rod approximation (bottom).

with up to ten crossings. A prime knot is a knot which cannot be thought of as the sum of two or more other knots with fewer crossings. Only six of these knots are of the torus type, and have been found in the Skyrme-Faddeev model. We have seen the first example of a non-torus knot occurring in the Skyrme-Faddeev model with ten crossings in the previous chapter. We would like to try and predict which types of knots we are likely to expect within the Skyrme-Faddeev model to focus the search for rational maps which can be used to generate initial fields in the full model.

The drawback of studying these knots in the full model is that constructions via rational map ansatz are not easy to generalise and can take a large amount of work to find, with no guarantee that a field knotted in such a way exists in the model. In comparison, the elastic rod approximation gives a very simple description of the knot which is easily applicable to any knot. The way that the elastic rod model is constructed also means that any initial knot cannot self-intersect and so change to give a different knot. It can be a downside to the elastic rod approximation that a wide range of possible knot configurations have to be considered for each charge to ensure that the minimum is indeed found. However, in this section it will actually be a useful feature, since a knot of a particular form can be compared energetically with the energy minima for all charges, rather than only being able to compare knots when they occur in the full model.

Another strength of the elastic rod model which we are yet to mention is that given a solution, it is straight-forward to use this to generate an initial field in the full model which has this structure. Although these fields are not solutions to the full theory, and indeed there is no guarantee that such a solution will exist in the theory, the elastic rod model makes generating such initial fields trivial. This is achieved by making use of ansatz (5.1.3). The initial conditions which arise from this are not quite as smooth as those generated by a rational map ansatz, however such a construction can help us to narrow the possibilities of the knots which occur in the Skyrme-Faddeev model.

We start this study by using the elastic rod model to demonstrate how useful it can be in understanding why certain subclasses of knots will not occur in the

model. The first case we consider is that of positive knots. It is known that some knots should not be expected to arise within the Skyrme-Faddeev model. As we have mentioned previously, the Hopf charge of a solution can be considered as the sum of the (signed) crossing number and the number of twists of the material frame about the position curve. Recall also that we have seen that there is a term in the energy which corresponds to the length of the hopfion. It then follows quite straightforwardly that if there was a mixture of positive and negative crossings, the length of the knot would be greater than a knot with only the net number of positive crossings. Therefore the energy of the hopfion which is not of the form of a positive knot would be greater and without the benefit of gaining additional charge. Thus we would expect all the hopfions to have the form of positive knots. It is known that all torus knots are positive.

The first case of a non-positive knot is the figure-eight knot, denoted 4_1 in Rolfson notation. This is achiral, a spatial reflection does not change the knot, and therefore it must have signed crossing number zero. It is therefore the most removed from a positive knot that a knot is able to be, with all the Hopf charge of such a configuration coming purely from the twisting contribution. We can use an initial configuration in which $\{\mathbf{x}_i\}$ describe a figure-eight knot. The results of such a study are shown in Table 5.2 and a solution of the elastic rod approximation is shown in Figure 5.5(a) which has charge five. We see that the energy of these solutions is much higher than those found previously at these charges. This shows us unequivocally that this form of solution is not preferred for the Skyrme-Faddeev model. We can show that this is indeed the case, by using our solutions for the figure-eight elastic rod to create an initial condition. When we use these with the numerical methods described in the previous chapter we find that solutions quickly relax to solutions usually seen in the Skyrme-Faddeev model at these charges.

Thus we see that we should be considering positive knots for the Skyrme-Faddeev model. This reduces to give us fifteen possible prime knots of ten or fewer crossings, excluding the torus knots. The simplest example of such a knot is the three-twist knot (5_2 in Rolfson notation). The energies found from such a computation are shown in Table 5.3 and an example of such a solution is shown in Figure 5.5(b).

Q	$E_N^{ER}(4_1)$	Minimal energy
1	3.77	1.0
2	3.91	1.54
3	4.08	2.06
4	4.31	2.50
5	4.61	2.84

Table 5.2: We show the normalised energy of a figure-eight knot in the elastic rod approximation, next to which we give the minimal energy elastic rod solution found for that charge.

(a) Figure-eight (b) Three-twist

Figure 5.5: Plots of solutions of the elastic rod model for particular non-torus knots. We have shown the charge five figure-eight knot and the charge ten three-twist knots.

Q	$E_N^{ER}(5_2)$	Minimal energy
6	4.48	3.19
7	4.59	3.54
8	4.76	3.89
9	4.98	4.28
10	5.27	4.72
11	5.61	4.97
12	6.00	5.30

Table 5.3: We show the normalised energy of a three-twist knot in the elastic rod approximation, next to which we give the minimal energy elastic rod solution found for that charge.

We see that energetically these are, although not near the energy minimum, closer to the range of solutions considered previously. However since these are still higher than the energy minimum found we again would not expect such an initial condition to exist in the full Skyrme-Faddeev model. This is indeed what is found when the solutions to the elastic rod model are used as an initial field in a field relaxation algorithm for the Skyrme-Faddeev model. We therefore need to consider further restrictions on the form of the knots. We discuss this in the next section.

5.4 Conclusions and Outlook

In this current on-going work we have examined the elastic rod approximation of the Skyrme-Faddeev model and have found that the energy values found for charges above seven are approximately in agreement with those found in the Skyrme-Faddeev model, but the ordering of the energy of configurations does no longer hold. However, it provides us with a way of easily deciding whether a type of solution is feasible to occur at certain charges. It is expected that the elastic rod model would give a more accurate depiction of the ordering of energy values if additional terms were to be included in the model.

We then used this to attempt to focus our search for the type of knots one could

expect to occur in the theory. We have seen that for some cases knots agree with the conjecture that we should be restricting to positive knots. It remains to be shown that this is the case for a wider range of knots, however it can be motivated from the form of the energy derived here. We have also seen that further restrictions are needed, since some positive knots have been seen not to have comparable energy to the minima found in this study. We conjecture that as well as restricting to positive knots, one must also restrict to those which are fibred. A knot is fibred if it is possible to fill space with a series of surfaces whose boundary is given by the knot. This makes physical sense since for the Skyrme-Faddeev model, the centreline of the knot is but one preimage and we would like the transition to other preimages to occur smoothly. The evidence that such a restriction on the classes of knots should be considered is that all the forms of knots found within the Skyrme-Faddeev model to date have been both positive and fibred. This is the case when initial conditions have gone to very different final states in energy minimisation algorithms.

Obviously much further work is needed to substantiate these ideas, however the elastic rod model provides a good way to decide whether they have any traction. If a restricted group of knots could be found, it would also provide a good way to test this before attempting to find a rational map to provide a smooth knotted field with the required structure.

Chapter 6

Concluding Remarks

In this chapter we make some final conclusions on the topics covered in this thesis. We have introduced a number of key principles which occur in the theories of topological solitons such as the existence and stability of solitons within a field theory. These details, covered in Chapter 1, we then applied to some concrete examples. Firstly we discussed a $(1+1)$-dimensional sine-Gordon kink theory, which as well as being a simple toy model of topological solitons to introduce the ideas, also occurs as an effective theory in the study of Skyrmions located on a domain wall where there is no Skyrme term included. We then also introduced a range of Skyrme models in both $(2+1)$ and $(3+1)$-dimensional theories.

We introduced the $(3+1)$-dimensional Skyrme model and then the $(2+1)$-dimensional analogue of this, the baby Skyrme model. Both of these theories are categorised by a generalised winding number which is a topological invariant and so classifies the possible solutions of the theory. We have seen in Chapters 2 and 3 particular examples of these lower dimensional theories. We have studied in Chapter 2 a particular choice of potential which breaks the symmetry of the system to a discrete symmetry. This creates a structure which can be thought of as including a classical colour dependence to the model. We investigated the static solutions of such a theory for a variety of theories with different numbers of colours present. We found that the link between solutions of the three colour theory with polyiamonds can be extended for theories with a higher number of colours to polyforms. We also detailed some of the effects this has on the polyform structure one might expect.

We then detailed our research of the dynamics of two baby Skyrmions with such a broken symmetry. We found that the scattering of two solitons exhibited the expected right-angled scattering and that parton exchange occurred in the model. It was found that the the scattering of the fields could be understood by a simple set of rules dictating the behaviour of individual parton scattering.

In Chapter 3 we were again looking at an $O(2)$ sigma model with a particular choice of potential. The motivation for this study was to consider a theory in which the Skyrme term was not included since this can be difficult to motivate physically. Instead the stability of the solution derives from it being located on a domain wall in the theory. We detail our research on the model, examining the stability of the static solutions found in the theory. We consider the scattering of two Skyrmions along the domain wall and find that the behaviour is well modelled at low speeds by an effective sine-Gordon kink theory as mentioned above. We then proceeded to study more exotic scatterings beyond the scope of the effective theory and found that the Skyrmions were able to survive scatterings where they were initially located on different domain walls which then collided.

We then turned our attention to the Skyrme-Faddeev model, which is a $(3+1)$-dimensional model with a similar structure to the Skyrme models but which exhibits solutions taking the form of knotted and linked fields. All solutions previously found were of fields which were knotted as torus knots or links thereof. In Chapter 4 we gave details of the construction of fields which have the form of a generalisation of torus knots called cable knots. We then demonstrated that at higher charges such fields form stable energy minima of the system. We detailed static solutions of the model for charges up to thirty-six and also found in the study examples of other knotted structures where fields had the form of hyperbolic knots.

Finally we presented some current work in which we use an approximation of the Skyrme-Faddeev model with an elastic rod to try to probe the type of knotted fields one should expect within the Skyrme-Faddeev model. We extend the known results of this approximation to hopfions of charge up to twelve. We then use this model to understand why particular types of knots are not preferred in the model before making some conjectures on the form of knots which should be found within the

model. We demonstrate these for some particular choices of knots, however further work is needed to make these claims more concrete.

Bibliography

[1] P. Jennings and T. Winyard, *Broken planar Skyrmions - statics and dynamics*, *JHEP* **1401** (2014) 122, [arXiv:1306.5935].

[2] P. Jennings and P. Sutcliffe, *The dynamics of domain wall Skyrmions*, *J.Phys.* **A46** (2013) 465401, [arXiv:1305.2869].

[3] P. Jennings, *Cabling in the Skyrme-Faddeev model*, arXiv:1412.8597.

[4] N. Manton and P. Sutcliffe, *Topological Solitons*. Cambridge University Press, Cambridge, 2004.

[5] G. H. Derrick, *Comments on nonlinear wave equations as models for elementary particles*, *J. Math. Phys.* **5** (1964) 1252–4.

[6] J. Perring and T. Skyrme, *A model unified field equation*, *Nucl. Phys.* **31** (1962) 550 – 555.

[7] L. A. Ferreira, B. Piette, and W. J. Zakrzewski, *Wobbles and other kink-breather solutions of the sine-gordon model*, *Phys. Rev. E* **77** (2008) 036613.

[8] S. Cuenda, N. R. Quintero, and A. Sánchez, *Sine-Gordon wobbles through Bäcklund transformations* , *Discrete and Continuous Dynamical Systems - Series S* **4** (2011) 1047–1056.

[9] T. Skyrme, *A Nonlinear field theory*, *Proc. Roy. Soc. Lond.* **A260** (1961) 127–138.

[10] T. Skyrme, *A unified field theory of mesons and baryons*, *Nucl. Phys.* **31** (1962) 556 – 569.

[11] E. Witten, *Global Aspects of Current Algebra*, *Nucl. Phys.* **B223** (1983) 422–432.

[12] E. Witten, *Current algebra, baryon and quark confinement*, *Nucl. Phys.* **B223** (1983) 433–444.

[13] R. A. Battye and P. M. Sutcliffe, *Solitonic fullerene structures in light atomic nuclei*, *Phys. Rev. Lett.* **86** (2001) 3989–3992.

[14] R. A. Battye and P. M. Sutcliffe, *Skyrmions, fullerenes and rational maps*, *Rev. Math. Phys.* **14** (2002) 29–86, [hep-th/0103026].

[15] G. Brown, *The Multifaceted Skyrmion*. World Scientific Publishing Company Pte Limited, 2014.

[16] R. A. Battye and P. M. Sutcliffe, *Skyrmions with massive pions*, *Phys. Rev. C* **73** (2006) 055205.

[17] C. Adam, J. Snchez-Guilln, and A. Wereszczyski, *A Skyrme-type proposal for baryonic matter* , *Phys. Lett. B* **691** (2010) 105 – 110.

[18] M. Gillard, D. Harland, and M. Speight, *Skyrmions with low binding energies*, arXiv:1501.0545.

[19] P. Sutcliffe, *Skyrmions in a truncated BPS theory*, *JHEP* **2011** (2011).

[20] D. Harland, *Topological energy bounds for the Skyrme and Faddeev models with massive pions* , *Phys. Lett. B* **728** (2014) 518 – 523.

[21] S. Sondhi, A. Karlhede, S. Kivelson, and E. Rezayi, *Skyrmions and the crossover from the integer to fractional quantum Hall effect at small Zeeman energies*, *Phys. Rev.* **B47** (1993) 16419–16426.

[22] X. Z. Yu, Y. Onose, N. Kanazawa, J. Park, Y. Matsui, N. Nagaosa, and Y. Tokura, *Real-space observation of a two-dimensional skyrmion crystal*, *Nature* **465** (2010) 901–904.

[23] B. Piette, B. Schroers, and W. Zakrzewski, *Multisolitons in a two-dimensional Skyrme model*, *Z. Phys. C* **65** (1995) 165–174.

[24] B. M. A. G. Piette, B. J. Schroers, and W. J. Zakrzewski, *Dynamics of Baby Skyrmions*, *Nucl. Phys.* **B439** (1995) 205–238, [hep-ph/9410256].

[25] T. Weidig, *The baby Skyrme models and their multi-skyrmions*, *Nonlinearity* **12** (1999) 1489.

[26] P. Eslami, M. Sarbishaei, and W. Zakrzewski, *Baby Skyrme models for a class of potentials*, *Nonlinearity* **13** (2000) 1867.

[27] D. Foster, *Baby Skyrmion chains*, *Nonlinearity* **23** (2010) 465, [arXiv:0904.3846].

[28] L. Faddeev, *Quantization of solitons*, *Preprint IAS Print-75-QS70 (Inst. Advanced Study, Princeton, NJ, 1975).*

[29] L. Faddeev and A. J. Niemi, *Stable knot-like structures in classical field theory*, *Nature* **387** (1997) 58–61.

[30] L. Faddeev and A. J. Niemi, *Partially dual variables in SU(2) Yang-Mills theory*, *Phys. Rev. Lett.* **82** (1999) 1624–1627, [hep-th/9807069].

[31] Y. Kawaguchi, M. Nitta, and M. Ueda, *Knots in a Spinor Bose-Einstein Condensate*, *Phys. Rev. Lett.* **100** (2008) 180403.

[32] J. Speight, *Supercurrent coupling in the Faddeev-Skyrme model*, *J.Geom.Phys.* **60** (2010) 599–610, [arXiv:0812.1493].

[33] R. Bott and L. W. Tu, *Differential Forms in Algebraic Topology.* Springer, New York, 1995.

[34] P. Sutcliffe, *Knots in the Skyrme-Faddeev model*, *Proc. R. Soc. A* **463** (2007) 3001–3020.

[35] A. F. Vakulenko and L. V. Kapitanskii, *Stability of solitons in S^2 in the nonlinear σ-model*, *Sov. Phys. Dokl.* **24** (1979) 433.

[36] A. Kundu and Y. P. Rybakov, *Closed-vortex-type solitons with Hopf index*, *J. Phys. A* **15** (1982) 269.

[37] R. S. Ward, *Hopf solitons on S^3 and $\mathbb{R}^3$*, *Nonlinearity* **12** (1999) 241.

[38] F. Lin and Y. Yang, *Energy Splitting, Substantial Inequality, and Minimization for the Faddeev and Skyrme Models*, *Commun. Math. Phys.* **269** (2007) 137–152.

[39] J. Jaykka and M. Speight, *Easy plane baby skyrmions*, *Phys. Rev.* **D82** (2010) 125030, [arXiv:1010.2217].

[40] R. S. Ward, *Planar skyrmions at high and low density*, *Nonlinearity* **17** (2004) 1033.

[41] J. Jaykka, M. Speight, and P. Sutcliffe, *Broken Baby Skyrmions*, *Proc. Roy. Soc. Lond.* **A468** (2012) 1085–1104, [arXiv:1106.1125].

[42] J. E. Jones, *On the Determination of Molecular Fields. II. From the Equation of State of a Gas*, *Proc. Roy. Soc. Lond. A* **106** (1924) 463–477.

[43] M. Nitta, *Josephson vortices and the Atiyah-Manton construction*, *Phys. Rev. D* **86** (2012) 125004.

[44] M. Nitta, *Matryoshka Skyrmions* , *Nucl. Phys. B* **872** (2013) 62 – 71.

[45] M. Nitta, *Correspondence between Skyrmions in 2+1 and 3+1 dimensions*, *Phys. Rev. D* **87** (2013) 025013.

[46] M. Kobayashi and M. Nitta, *Sine-Gordon kinks on a domain wall ring*, *Phys. Rev. D* **87** (2013) 085003.

[47] G. W. Gibbons and P. K. Townsend, *Bogomol'nyi Equation for Intersecting Domain Walls*, *Phys. Rev. Lett.* **83** (1999) 1727–1730.

[48] S. M. Carroll, S. Hellerman, and M. Trodden, *Domain wall junctions are 1/4 BPS states*, *Phys. Rev. D* **61** (2000) 065001.

[49] C. Adams, *The Knot Book*. American Mathematical Society, Providence, R.I., 2004.

[50] D. Rolfsen, *Knots and Links*. AMS/Chelsea Publication Series. AMS Chelsea Pub., 1976.

[51] P. J. Callahan, J. C. Dean, and J. R. Weeks, *The simplest hyperbolic knots*, *J. Knot Theory Ramifications* **08** (1999) 279–297.

[52] A. Champanerkar, I. Kofman, and E. Patterson, *The next simplest hyperbolic knots*, *J. Knot Theory Ramifications* **13** (2004) 965–987.

[53] A. Champanerkar, I. Kofman, and T. Mullen, *The 500 simplest hyperbolic knots*, *J. Knot Theory Ramifications* **23** (2014) 1450055.

[54] R. A. Battye and P. M. Sutcliffe, *Knots as Stable Soliton Solutions in a Three-Dimensional Classical Field Theory*, *Phys. Rev. Lett.* **81** (1998) 4798–4801.

[55] R. A. Battye and P. M. Sutcliffe, *Solitons, links and knots*, *Proc. R. Soc. Lond. A* **455** (1999) 4305–4331.

[56] E. Brieskorn and H. Knörrer, *Plane Algebraic Curves*. Birkhuser Basel, Basel; Boston, 1986.

[57] D. Eisenbud and W. D. Neumann, *Three-dimensional Link Theory and Invariants of Plane Curve Singularities*. PUP, Princeton, 1985.

[58] E. Kahler, *Über die Verzweigung einer algebraischen Funktion zweier Veränderlichen in der Umgebung einen singulären Stelle*, *Math. Zeits.* **30** (1929) 188–206.

[59] C. T. C. Wall, *Singular Points of Plane Curves*. CUP, Cambridge, 2004.

[60] M. Culler, N. M. Dunfield, and J. R. Weeks, "SnapPy, a computer program for studying the topology of 3-manifolds." Available at http://snappy.computop.org.

[61] D. Nicole, *Solitons With Nonvanishing Hopf Index*, *J. Phys.* **G4** (1978) 1363.

[62] M. Gillard and P. Sutcliffe, *Hopf solitons in the Nicole model*, *J. Math. Phys.* **51** (2010).

[63] H. Aratyn, L. Ferreira, and A. Zimerman, *Toroidal solitons in 3+ 1 dimensional integrable theories*, *Phys. Lett. B* **456** (1999) 162–170.

[64] M. Gillard, *Hopf solitons in the AFZ model*, *Nonlinearity* **24** (2011) 2729.

[65] J. Gladikowski and M. Hellmund, *Static solitons with nonzero Hopf number*, *Phys. Rev. D* **56** (1997) 5194–5199.

[66] M. R. Dennis, R. P. King, B. Jack, K. OHolleran, and M. J. Padgett, *Isolated optical vortex knots*, *Nat Phys* **6** (2010) 118–121.

[67] D. Harland, M. Speight, and P. Sutcliffe, *Hopf solitons and elastic rods*, *Phys. Rev. D* **83** (2011) 065008.

[68] A. Goriely, *Twisted Elastic Rings and the Rediscoveries of Michell's Instability*, *J. Elasticity* **84** (2006) 281–299.

[69] M. Bergou, M. Wardetzky, S. Robinson, B. Audoly, and E. Grinspun, *Discrete elastic rods*, *ACM Trans. Graph.* **27** (2008) 63:1–63:12.

[70] R. Litherland, J. Simon, O. Durumeric, and E. Rawdon, *Thickness of knots*, *Topology and its Applications* **91** (1999) 233 – 244.

[71] E. J. Rawdon, *Can computers discover ideal knots?*, *Exper. Math.* **12** (2003) 287–302.

[72] E. J. Rawdon, *Approximating the thickness of a knot*, *Ideal knots* (1998) 143–150.

[73] E. J. Rawdon, *Approximating smooth thickness*, *J. Knot Theory Ramifications* **9** (2000) 113–145.

Appendix A

Knotted fields and Hopf charge

As we have mentioned in Chapter 4, the charge of initial conditions has not been found analytically for all choices of γ. Instead we solve numerically the equation $(p(Z_1, Z_0), q(Z_1, Z_0)) = (\epsilon, 0)$ for a particular value for ϵ. We then count the number these solutions which are within the unit four-ball $(Z_1, Z_0) \in \mathbb{B}^4 \subset \mathbb{C}^2$. In this appendix we give the rational maps used and tabulate the charges of these for each of the initial fields used to generate solutions presented. In the calculations below we set $\eta = 1/2$.

A.1 (2,3) cable on the (3,2)-torus knot

We recall that the initial field for $\mathcal{C}^{2,3}_{3,2}$ is generated by the field given by

$$W = \frac{Z_1^\alpha Z_0^\beta (Z_1 - Z_0)^\gamma}{Z_0^4 - 2Z_1^3 Z_0^2 - 4\eta^2 Z_1^3 Z_0 + Z_1^6 - \eta^4 Z_1^3} \tag{A.1.1}$$

for α a non-negative integer, β a positive integer and $\gamma \in \{0, 1\}$. We see that the fields of this form generate the charges given in Tables A.1 and A.2. We note that for charges with $\gamma = 0$, the charge is $4\alpha + 6\beta$, which we see is indeed the case when checking these solutions numerically. For $\gamma = 1$ we find a similar situation, we see that if we count the number of solutions there are $4\alpha + 6\beta + 5$. This is the case for all the α and β considered in this study.

We can understand this value by recalling that for η small enough the charge would be $4(\alpha + 1) + 6\beta$. However, in the case $\eta = 1/2$ we find one a root moving

$\gamma = 0$		β									
		0	1	2	3	4	5	6	7	8	9
	1	4	10	16	22	28	34	40	46	52	58
	2	8	14	20	26	32	38	44	50	56	62
	3	12	18	24	30	36	42	48	54	60	66
	4	16	22	28	34	40	46	52	58	64	70
α	5	20	26	32	38	44	50	56	62	68	74
	6	24	30	36	42	48	54	60	66	72	78
	7	28	34	40	46	52	58	64	70	76	82
	8	32	38	44	50	56	62	68	74	80	86
	9	36	42	48	54	60	66	72	78	84	90

Table A.1: The topological charge of fields generated by the initial field for $\mathcal{C}^{2,3}_{3,2}$ with $\gamma = 0$.

from the interior to the exterior of the four-ball. Thus our rational map has an additional unit of Hopf charge, giving the value found numerically of $4\alpha + 6\beta + 5$.

A.2 (2,5) cable on the (3,2)-torus knot

We did not give the exact form of this cable knot in Chapter 4. It follows similarly for the case above that the initial field for $\mathcal{C}^{2,5}_{3,2}$ is generated by the field given by

$$W = \frac{Z_1^\alpha Z_0^\beta (Z_1 - Z_0)^\gamma}{Z_0^4 - 2Z_1^3 Z_0^2 - 4\eta^2 Z_1^4 Z_0 + Z_1^6 - \eta^4 Z_1^5} \tag{A.2.2}$$

for α a non-negative integer, β a positive integer and $\gamma \in \{0, 1\}$. We see that the fields of this form generate the charges given in Tables A.3 and A.4. We see that for $\gamma = 0$ a similar argument to that for $\mathcal{C}^{2,3}_{3,2}$ gives us that the Hopf charge of the map is again $4\alpha + 6\beta$. Indeed this is what we find by numerically calculating the number of preimages within the four-ball. For $\gamma = 1$ we again find numerically that the number of preimages is given by $4\alpha + 6\beta + 5$.

A similar argument for $\gamma = 1$ as that for $\mathcal{C}^{2,3}_{3,2}$ shows that provided roots with $Z_1 = Z_0$ and $Z_1^2 - (2 + 4s\eta^2 + s\eta^4)Z_1 + 1 = 0$ lie within/outside the four-ball for $s \in [0, 1]$ then the charge of the map is $4(\alpha + 1) + 6\beta$. However, as seen in Figure A.1 we see that this is not the case for $\eta = 1/2$ and indeed one root moves outside

$\gamma=1$		β									
		0	1	2	3	4	5	6	7	8	9
	1	9	15	21	27	33	39	45	51	57	63
	2	13	19	25	31	37	43	49	55	61	67
	3	17	23	29	35	41	47	53	59	65	71
	4	21	27	33	39	45	51	57	63	69	75
α	5	25	31	37	43	49	55	61	67	73	79
	6	29	35	41	47	53	59	65	71	77	83
	7	33	39	45	51	57	63	69	75	81	87
	8	37	43	49	55	61	67	73	79	85	91
	9	41	47	53	59	65	71	77	83	89	95

Table A.2: The topological charge of fields generated by the initial field for $\mathcal{C}^{2,3}_{3,2}$ with $\gamma = 1$.

the four-ball in such a limit. Thus we can understand that the charge is $4\alpha+6\beta+5$. We also see that for a different choice of η the roots do not cross the boundary of the four-ball and we would have a charge $4(\alpha+1)+6\beta$ rational map.

A.3 (2,7) cable on the (3,2)-torus knot

We recall that the initial field for $\mathcal{C}^{2,7}_{3,2}$ is generated by the field given by

$$W = \frac{Z_1^\alpha Z_0^\beta (Z_1 - Z_0)^\gamma}{Z_0^4 - 2Z_1^3 Z_0^2 - 4\eta^2 Z_1^5 Z_0 + Z_1^6 - \eta^4 Z_1^7} \tag{A.3.3}$$

for α a non-negative integer, β a positive integer and $\gamma \in \{0, 1\}$. We see that the fields of this form generate the charges given in Tables A.5 and A.6. For $\gamma = 0$ we can again show analytically that $4\alpha + 6\beta$, which is indeed what is found by numerically counting the preimages. For $\gamma = 1$ we again see that we have charge $4\alpha + 6\beta + 5$. Again we can argue that for the choice of η small enough such that roots at $Z_1 = Z_0$ and $-s\eta^4 Z_1^3 + (1 - 4s\eta^2)Z_1^2 - 2Z_1 + 1 = 0$ remain inside/outside the four-ball for all $s \in [0, 1]$ the rational map has charge $4(\alpha + 1) + 6\beta$. We find that for our choice of $\eta = 1/2$ we find one of these roots moves outside the four-ball and so we should have Hopf charge $4\alpha + 6\beta + 5$. This is shown in Figure A.2. Note that one of the roots lies far outside the four-ball and so is off the scale of the plot.

$\gamma = 0$		β									
		0	1	2	3	4	5	6	7	8	9
	1	4	10	16	22	28	34	40	46	52	58
	2	8	14	20	26	32	38	44	50	56	62
	3	12	18	24	30	36	42	48	54	60	66
	4	16	22	28	34	40	46	52	58	64	70
α	5	20	26	32	38	44	50	56	62	68	74
	6	24	30	36	42	48	54	60	66	72	78
	7	28	34	40	46	52	58	64	70	76	82
	8	32	38	44	50	56	62	68	74	80	86
	9	36	42	48	54	60	66	72	78	84	90

Table A.3: The topological charge of fields generated by the initial field for $\mathcal{C}^{2,5}_{3,2}$ with $\gamma = 0$.

$\gamma = 1$		β									
		0	1	2	3	4	5	6	7	8	9
	1	9	15	21	27	33	39	45	51	57	63
	2	13	19	25	31	37	43	49	55	61	67
	3	17	23	29	35	41	47	53	59	65	71
	4	21	27	33	39	45	51	57	63	69	75
α	5	25	31	37	43	49	55	61	67	73	79
	6	29	35	41	47	53	59	65	71	77	83
	7	33	39	45	51	57	63	69	75	81	87
	8	37	43	49	55	61	67	73	79	85	91
	9	41	47	53	59	65	71	77	83	89	95

Table A.4: The topological charge of fields generated by the initial field for $\mathcal{C}^{2,5}_{3,2}$ with $\gamma = 1$.

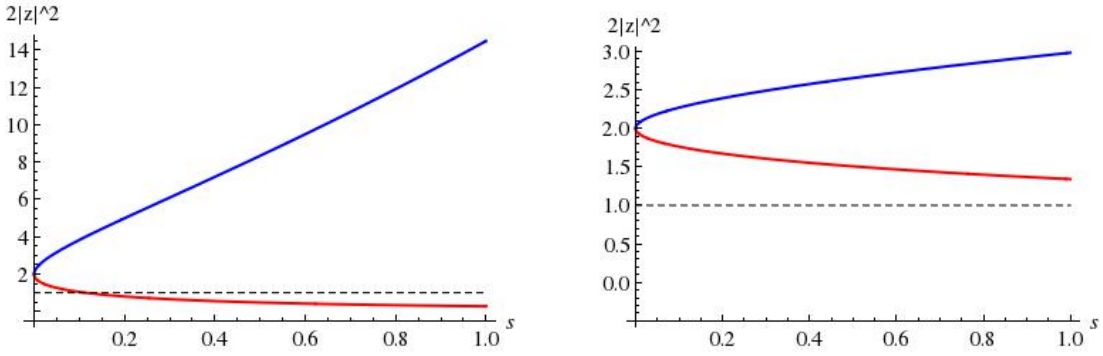

(a) $\eta = 0.5$ (b) $\eta = 0.1$

Figure A.1: Plots of $2|z|^2$ for the roots to $z^2 - (2 + 4s\eta^2 + s\eta^4)z + 1$ for $s \in [0, 1]$ for different values of η. Also marked is the value at which the root lies on the three-sphere.

$\gamma = 0$		β									
		0	1	2	3	4	5	6	7	8	9
	1	4	10	16	22	28	34	40	46	52	58
	2	8	14	20	26	32	38	44	50	56	62
	3	12	18	24	30	36	42	48	54	60	66
	4	16	22	28	34	40	46	52	58	64	70
α	5	20	26	32	38	44	50	56	62	68	74
	6	24	30	36	42	48	54	60	66	72	78
	7	28	34	40	46	52	58	64	70	76	82
	8	32	38	44	50	56	62	68	74	80	86
	9	36	42	48	54	60	66	72	78	84	90

Table A.5: The topological charge of fields generated by the initial field for $\mathcal{C}^{2,7}_{3,2}$ with $\gamma = 0$.

$\gamma = 1$		β									
		0	1	2	3	4	5	6	7	8	9
	1	9	15	21	27	33	39	45	51	57	63
	2	13	19	25	31	37	43	49	55	61	67
	3	17	23	29	35	41	47	53	59	65	71
	4	21	27	33	39	45	51	57	63	69	75
α	5	25	31	37	43	49	55	61	67	73	79
	6	29	35	41	47	53	59	65	71	77	83
	7	33	39	45	51	57	63	69	75	81	87
	8	37	43	49	55	61	67	73	79	85	91
	9	41	47	53	59	65	71	77	83	89	95

Table A.6: The topological charge of fields generated by the initial field for $\mathcal{C}^{2,7}_{3,2}$ with $\gamma = 1$.

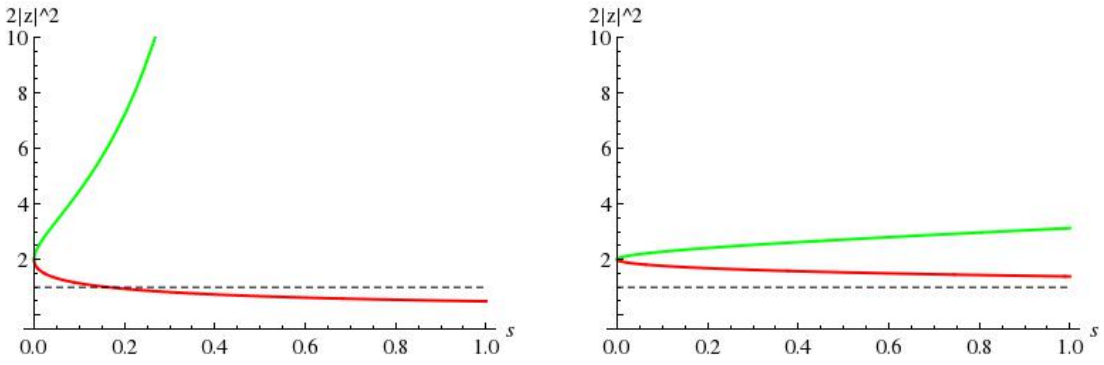

(a) $\eta = 0.5$ (b) $\eta = 0.1$

Figure A.2: Plots of $2|z|^2$ for the roots to $-s\eta^4 z^3 + (1 - 4s\eta^2)z^2 - 2z + 1$ for $s \in [0, 1]$ for different values of η. Note that one root lies off the scale of our plot for this range. Also marked is the value at which the root lies on the three-sphere.

A.4 Cable links

Cable links occur when we have a similar rational map as we had for the cable knots, however with (m_2, n_2) no longer being coprime. This gives us cable links, but without making it clear how the charge is shared between the components. Instead, for a field of the form $\mathcal{L}^{5,5}_{Q_1(3,2),Q_2(3,2)}$ we consider a rational map of the form

$$W = \frac{Z_1^{\alpha_1} Z_0^{\beta_1} (Z_1 - Z_0)^{\gamma_1}}{Z_0^2 - 2\eta_1 Z_1 Z_0 - Z_1^3 + \eta_1^2 Z_1^2} + \frac{Z_1^{\alpha_2} Z_0^{\beta_2} (Z_1 - Z_0)^{\gamma_2}}{Z_0^2 - 2\eta_2 Z_1 Z_0 - Z_1^3 + \eta_2^2 Z_1^2} \tag{A.4.4}$$

for α_1, α_2 non-negative integers; β_1, β_2 positive integers; $\gamma_1, \gamma_2 \in \{0, 1\}$ and non-zero $\eta_1, \eta_2 \in \mathbb{C}$ with $\eta_1 \neq \eta_2$. In this study we took $\eta_1 = -i\eta_2 = 1/2$. From the form of the rational map we can see the two terms each relate to distinct components of the link, with each term contributing charge Q_1 and Q_2 respectively. Again we can do a parameter search for these parameters. We found that it was sufficient to consider only the case where both $\gamma_1 = \gamma_2 = 0$ or where $\gamma_1 = 0$, $\gamma_2 = 1$. This second case was needed to introduce fields with odd topological charge. We again resorted to numerically checking that the roots found lay inside the unit four-ball.

Similarly, for the field of the form $\mathcal{L}^{6,6}_{Q_1(3,2),Q_2(3,2)}$ we considered rational maps of the form

$$W = \frac{Z_1^{\alpha_1} Z_0^{\beta_1} (Z_1 - Z_0)^{\gamma_1}}{Z_0^2 - 2\eta_1 Z_1^3 Z_0 - Z_1^3 + \eta_1^2 Z_1^3} + \frac{Z_1^{\alpha_2} Z_0^{\beta_2} (Z_1 - Z_0)^{\gamma_2}}{Z_0^2 - 2\eta_2 Z_1^3 Z_0 - Z_1^3 + \eta_2^2 Z_1^3} \tag{A.4.5}$$

for α_1, α_2 non-negative integers; β_1, β_2 positive integers; $\gamma_1, \gamma_2 \in \{0, 1\}$ and non-zero $\eta_1, \eta_2 \in \mathbb{C}$ with $\eta_1 \neq \eta_2$. In this study for this cable link we again took $\eta_1 = -i\eta_2 = 1/2$, and it was sufficient to consider the two cases $\gamma_1 = \gamma_2 = 0$ or where $\gamma_1 = 0$, $\gamma_2 = 1$.